UNIVERSITY OF OKLAHOMA

GRADUATE COLLEGE

REGIONAL STRATIGRAPHY AND PROXIMAL TO DISTAL VARIATION OF LITHOLOGY AND POROSITY WITHIN A MIXED CARBONATE-SILICICLASTIC SYSTEM, MERAMEC AND OSAGE SERIES (MISSISSIPPIAN), CENTRAL OKLAHOMA

A THESIS

SUBMITTED TO THE GRADUATE FACULTY

in partial fulfillment of the requirements for the

Degree of

MASTER OF SCIENCE

By

KATHERINE DRUMMOND
Norman, Oklahoma
2018

REGIONAL STRATIGRAPHY AND PROXIMAL TO DISTAL VARIATION OF LITHOLOGY AND POROSITY WITHIN A MIXED CARBONATE-SILICICLASTIC SYSTEM, MERAMEC AND OSAGE SERIES (MISSISSIPPIAN), CENTRAL OKLAHOMA

A THESIS APPROVED FOR THE
CONOCOPHILLIPS SCHOOL OF GEOLOGY AND GEOPHYSICS

BY

Dr. Matthew J. Pranter, Chair

Dr. John D. Pigott

Dr. Michael G. Grammer

ACKNOWLEDGEMENTS

I want to recognize and thank Dr. Matthew Pranter for all his guidance, support, communication, and knowledge throughout the entirety of this project. This research used software provided to the University of Oklahoma by IHS for Petra, Schlumberger for Petrel and Techlog, and The EasyCopy Company for EasyCore. I would like to thank Warwick Energy and Sandridge Energy for donating well data to this project. Core data was supplied from the Oklahoma Petroleum Information Center (OPIC). I would also like to thank Dr. Piggott and Dr. Michael Grammer for their advice and input. Thank you to Suriamin for his guidance through describing core and his time. Thank you to all of the RCML for their help and contribution, especially Niles Wethington.

TABLE OF CONTENTS

LIST OF TABLES

LIST OF FIGURES

ABSTRACT

Mississippian reservoirs of northern and central Oklahoma were deposited within a regionally extensive mixed carbonate-siliciclastic system. The stratigraphy, lithology, and porosity characteristics of the Mississippian "Meramec" and "Osage" series vary significantly as older proximal ramp carbonates transition into more distal calcareous, quartz, and feldspar-rich siltstones. Lithofacies within the northern "proximal" area commonly include altered chert, skeletal grainstones, peloidal packstones-grainstones, bioturbated wackestones-packstones, bioturbated mudstones-wackestones, glauconitic sandstones and siliceous shale. Distal lithofacies include structureless to bioturbated calcareous sandstones, calcareous siltstones, and laminated calcareous mudstones. Core-based lithologies are related to well-log properties and predicted in non-cored wells through electrofacies classification methods including Artificial-Neural Network (ANN) and k-means clustering. The ANN yielded the highest overall accuracy (~85%) for classifying lithologies in non-cored wells.

Core data, conventional well logs, lithology logs, and log-attribute curves were integrated to interpret depositional cycles and establish the regional stratigraphic framework of the Mississippian. The Mississippian interval consists of sixteen progradational stratigraphic zones. The proximal to distal and stratigraphic variability of lithology and porosity are evaluated through depositional-dip and oblique-oriented cross sections and reservoir models. From proximal to distal, a carbonate-dominated succession that is capped by diagenetically altered limestone and chert-rich deposits transitions into a more siliciclastic-dominated interval, with increasing clay content stratigraphically

upward and basinward. Distally, higher total porosity is associated with greater clay content and less calcite cement. Whereas, proximally, diagenetically altered cherts and cherty limestones exhibit higher total porosity near the crests of clinoforms.

INTRODUCTION

The Mississippian interval of the Anadarko Basin has been of high interest since the early 1900's owing to the large volumes of associated hydrocarbons. The Mississippian Meramec and Osage series of the Anadarko Basin includes formations that form a regionally extensive mixed siliciclastic and carbonate interval that is stratigraphically above the Woodford Shale and below the Pennsylvanian Cherokee Group. The Mississippian interval (informally referred to as the "Mississippi Lime") in northern Oklahoma and southern Kansas is primarily a carbonate and altered chert-rich system. Whereas, down-dip in the Sooner Trend of the Anadarko Basin of Canadian and Kingfisher counties (STACK) and south-central Oklahoma oil province (SCOOP), the Mississippian primarily represents a siliciclastic system of quartz and feldspathic very-fine sandstones, calcareous siltstones, and mixed carbonate and siliciclastic mudstones. The Mississippian carbonates and siltstones were deposited across a broad, gently sloping ramp and basin floor of the Anadarko Basin (Guschick and Sandberg, 1983; Chaplin, 2010) (Figure 1) and form shoaling-upward lithofacies successions and prolific reservoirs. Lithofacies and associated reservoir quality vary significantly throughout the study area, where porosity ranges from less than 1% to 20%.

Traditionally, subsurface lithology is determined from cores and well-log signatures. However, most wells are not cored, creating a need to classify and predict lithology from non-cored wells. Lithologic classification from well logs has become more accurate as technology has developed and studies have used combinations of well-log signatures to estimate lithology (Rider and Laurier, 1979; Sullivan et al., 2003; Qi et al.,

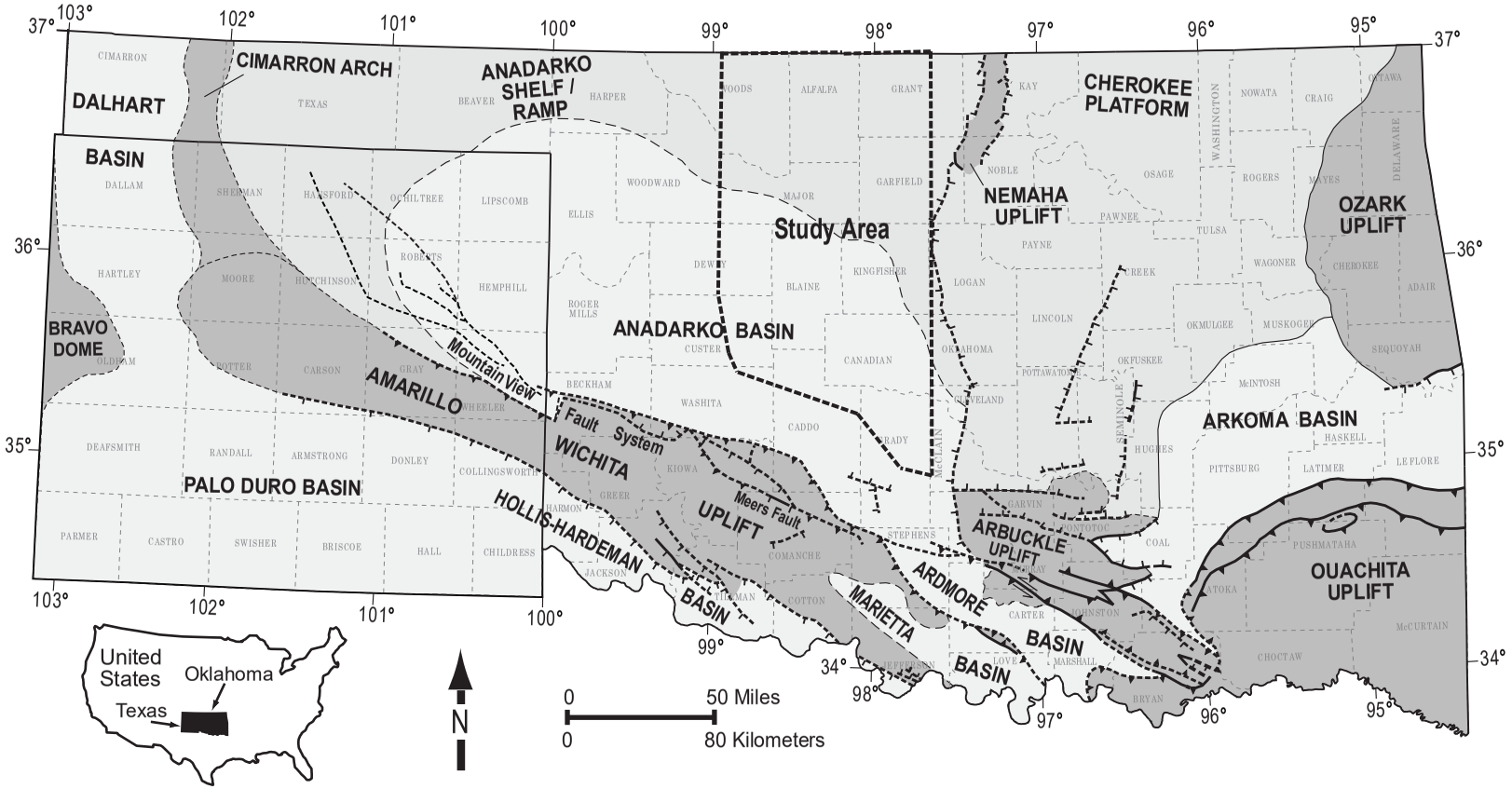

Figure 1: Regional map of major tectonic provinces of Oklahoma and part of Texas. Modified from Dutton, 1985; Campbell et al., 1988; McConnell et al., 1989; Northcutt and Campbell, 1995; Johnson and Luza, 2008; LoCricchio, 2012.

.

2007; Costello et al., 2014; Allen and Pranter, 2016, Wethington and Pranter, 2018). Doveton (1986) determined that porosity logs of carbonate intervals can discriminate lithofacies which have been affected by diagenesis. Statistical approaches have been explored since the 1990's to automate the task of facies prediction from well logs. The term "electrofacies" was introduced by Serra and Abbot (1980) and is defined as "the set of wireline log responses which characterizes a bed and permits it to be distinguished from others". Wolff and Pelissier-Combescure (1982) were early practitioners of the multivariate statistical approach to automate facies classification which utilized principle components and cluster analysis to estimate the occurrence of lithofacies. The non-multivariate analysis approach of the artificial neural network (ANN) has been a common approach used to successfully predict electrofacies in non-cored wells (Kapur et al., 1998; Grotsch and Mercadier, 1999; Saggaf and Nebrija, 2000, Russell et al., 2002; Caers and Zhang, 2004; Dubois et al., 2007; Allen and Pranter, 2016). In more recent studies by Qi et al. (2007), Costello et al. (2014), Lindzey (2015), and Wethington and Pranter (2018), statistical estimation methods were utilized to identify lithofacies and lithologies within the Mississippian interval. ANNs and clustering electrofacies classification techniques were used to predict the lithologies based on well-log signatures in non-cored wells. These techniques were used to create lithology logs as a constraint to generate 3-D lithology models of the Mississippian limestone to understand the lithologic variability.

Diagenetic processes have highly altered the Mississippian interval, creating a complex arrangement of cherts and carbonates. Rogers (2001) called the prolific porous chert-rich intervals "chat" and studied the depositional and diagenetic origin. Well-log

and core samples from northern Oklahoma suggested that much of the replacement of calcite by silica was likely due to supersaturated meteoric waters from periods of subaerial exposure from sea-level drop, and tectonic uplift (Rogers, 2001) (Appendix A-5). Hydrothermal alteration also was observed to play a part in digenesis from fluid inclusions (Coveney, 1992; Young, 2010; Ramaker et al., 2014; Shelley et al., 2017; Suriamin and Pranter, 2018). Mazzullo et al. (2008) divided diagenesis into three stages of chert formation. Farzaneh (2012), Haynes (2013), Birch (2015), and Lindzey (2015) observed a variety of alteration types resulting from silicification, brecciation, and dolomitization, all of which can impact reservoir quality. In the northern part of the study area, silicification is perhaps the most pervasive diagenetic process and is responsible for enhanced porosity associated with productive tripolitic and altered chert intervals.

Subsidence, uplift, relative sea-level changes and subaerial exposure, changes in ocean conditions, and different depositional environments along the widespread carbonate ramp resulted in significant heterogeneity in the lithologies, reservoir properties, and stratigraphy (Rogers, 2001; Watney et al., 2001; Mazzullo et al., 2009; Grammer et al., 2013; LeBlanc, 2014; Lindzey, 2015; Flinton, 2016; Jaeckel, 2016; Pranter et al., 2016; Mazzullo et al., 2016; Price et al., 2017; Price and Grammer, 2018; Childress and Grammer, 2018; Shelley et al. 2018; Miller, 2018; Wethington and Pranter, 2018). The primary nomenclature of the Mississippian limestone was developed and modified from outcrop data in the Ozark Uplift region for Kansas (Mazzullo, 2011). However, a formal subsurface nomenclature has not been accepted relating the

stratigraphy up-dip on the carbonate shelf to the stratigraphy down-dip in the distal basinal settings (Figure 2).

The proximal to distal stratigraphic and depositional variability of the interpreted "Meramec" and "Osage" series from northern to south-central Oklahoma is complex. The purpose of this study is to further delineate the regional stratigraphy, dominant lithologies, and depositional environments and to evaluate the utility of two electrofacies classification techniques to accurately estimate lithologies of the Mississippian interval. Expanding upon the relevant previous research, this project defines stratigraphic correlations of the Mississippian from the Anadarko distally steepened ramp margin into the basin. This study also investigates the complex-spatial distribution of lithologies/lithofacies and porosity within the Mississippian (Meramec and Osage series).

The study area extends from the Kansas-Oklahoma border, including the southern extent of the Mississippi Lime play, to south-central Oklahoma, and encompasses both the STACK play and a portion of the SCOOP play (Figure 3). The dataset includes data for 1255 wells (664 wells with digital logs and an additional 591 wells with raster logs), and eight published and three new core descriptions for eleven wells (three in Grant, one in Garfield, one in Woods, two in Kingfisher, three in Blaine, and one in Canadian counties, Oklahoma; Figure 3). The data were utilized to create proximal to distal dip- and oblique-oriented transects to interpret and illustrate the lithology and porosity variability of the Mississippian strata. The data presented are used to better understand the study area in terms of the complex-spatial distribution of lithologies, porosity, and how reservoir quality relates to the Mississippian sequence-stratigraphic framework.

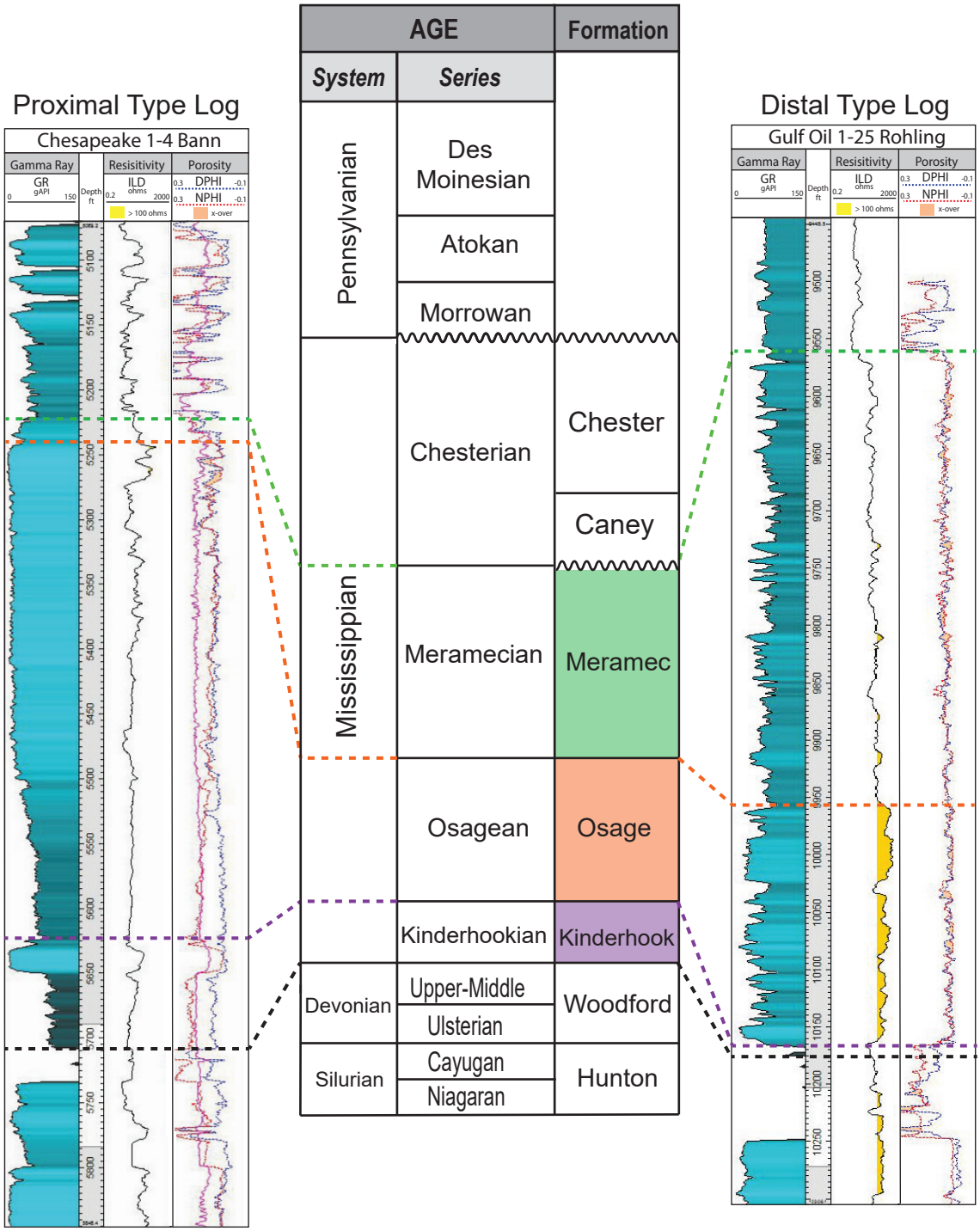

Figure 2: Generalized stratigraphic column and proximal and distal type logs for the study area (modified from Boyd, 2008). The left is a proximal type log from the northern part of the study area and the right is a distal type log from the southern part of the study area.

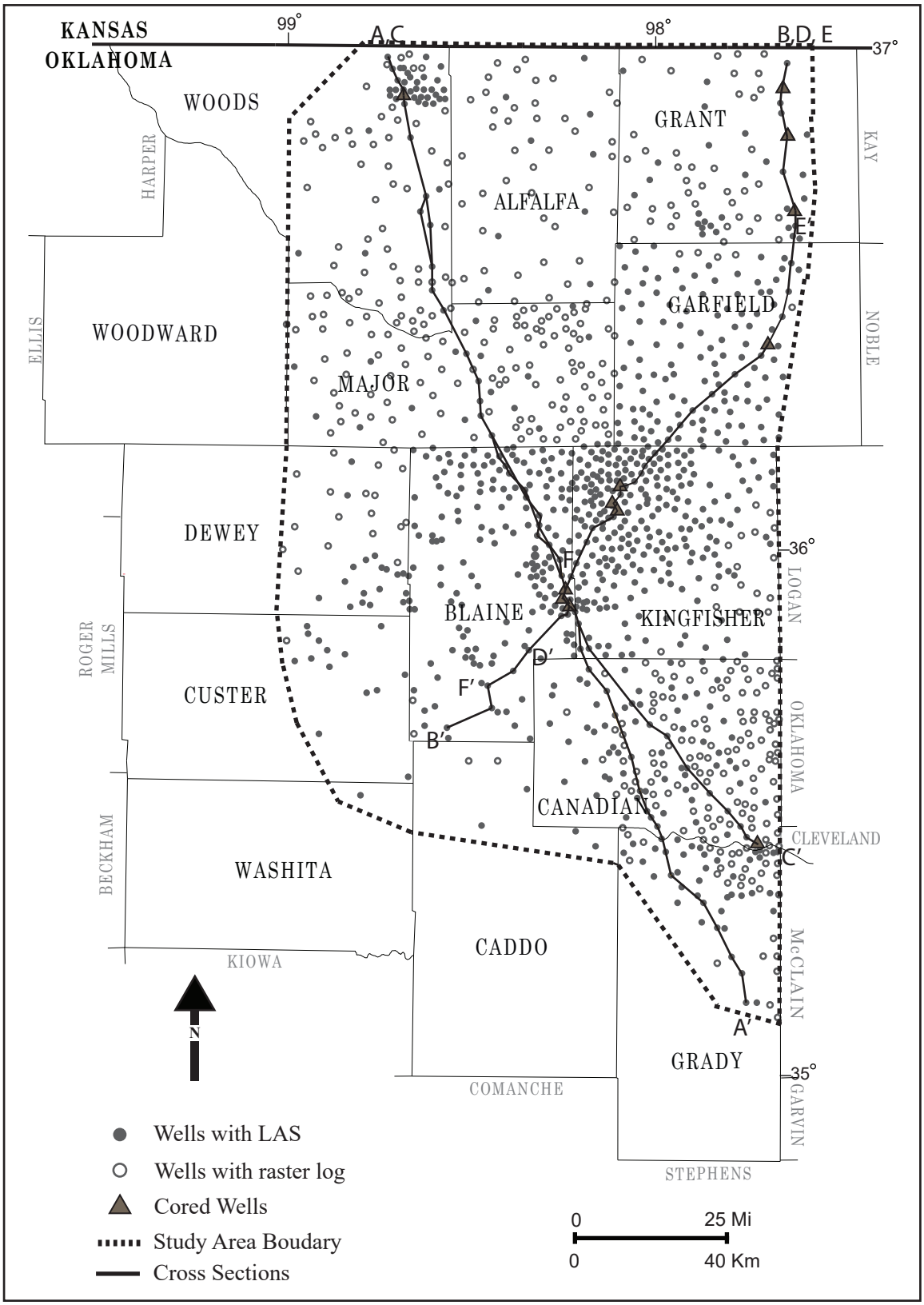
KANSAS
OKLAHOMA
99°
98°
37°
A,C
B,D,E
WOODS
HARPER
ALFALFA
GRANT
KAY
E
ELLIS
WOODWARD
GARFIELD
NOBLE
MAJOR
DEWEY
36°
F
LOGAN
BLAINE
KINGFISHER
ROGER MILLS
D′
F′
CUSTER
B′
OKLAHOMA
CANADIAN
CLEVELAND
C′
BECKHAM
WASHITA
CADDO
McCLAIN
KIOWA
A′
GRADY
35°
COMANCHE
GARVIN
STEPHENS
N
Wells with LAS
Wells with raster log
Cored Wells
Study Area Boudary
Cross Sections
0
25 Mi
0
40 Km

Figure 3: Basemap of study area showing the well, core, and cross-section locations. The dataset includes 1255 wells (664 digital logs and 591 raster logs) and 11 cored wells.

GEOLOGIC SETTING

The Anadarko Basin is one of the most prolific and deepest sedimentary basins in the continental United States (40,000 ft [12,200 m]) and compasses an area of 50,000 mi^2 (130,000 km^2) (Ham and Wilson, 1967). The basin is classified as an asymmetrical basin and exhibits numerous faults and is deeper to the south and gentle dips toward the north. The major structural features bounding the basin include the Amarillo-Wichita Uplift toward the south, Ardmore Basin and Arbuckle Mountains to the southeast, and the Nemaha uplift toward the east. Northward and northwestward, the basin thins into a broad shelf (Evans, 1979; Ball et at., 1991) (Figure 1).

The structural formation of the Anadarko Basin began in the Early to Middle Cambrian with the initiation of a rifting event near the modern southern boundary of Oklahoma, referred to as the Southern Oklahoma aulacogen (Ball et al., 1991). Following this failed rifting was an extended period of thermal subsidence as igneous extrusive deposits cooled through the Early Mississippian, forming the southern Oklahoma trough (Perry, 1989). During the Early and Middle Mississippian, the mid-continent was relatively inactive in terms of tectonic activity. However, by the Late Mississippian early compressional tectonism associated with the Ouachita Orogeny formed the current basin morphology and major geological features in the study area that directly influenced the distribution, deposition, and preservation of the Mississippian carbonates (Gutschick and Sandberg, 1983).

Mississippian carbonates were deposited across hundreds of miles of the expansive, shallow Burlington shelf along regions of the modern American mid-continent

(Gutschick and Sandberg, 1983). Deposition occurred on a distally steepened carbonate ramp and was influenced by both pre and syn-depositional structural features, including the Nemaha uplift and Ouachita-related faulting (Rogers, 2001). Sedimentation occurred in four main phases: the Kinderhookian, Osagean, Meramecian, and the Chesterian respectively (Northcutt et al., 2001). Regionally, deposits of Chesterian and Meramecian are absent in a proximal direction as a result of post-Mississippian erosion.

The study area was positioned between 20-30° south latitude relative to the paleoequator during the Mississippian Period which resulted in a subtropical setting with dominant wind and Coriolis-driven surface currents coming from the present day northeast direction (Gutschick and Sandberg, 1983; Witzke, 1990; Mazzulo et al., 2009) (Appendix A-1). A shallow, warm and oxygenated sea covered the wide carbonate platform of the North American craton during Early-to-Mid Mississippian (Curtis and Champlin, 1959). During this time, the shallow-marine waters were warm and covered the east-west trending ramp margin of the Burlington shelf (Gutschick and Sandberg, 1983; Northcutt et al., 2001; Elebiju et al., 2011). Newer studies suggest that the Mississippian interval was deposited on a distally steepened ramp (Jaeckel, 2016; Childress and Grammer, 2018; Price and Grammer, 2018). Ahr (1973) defines a ramp as a gently sloping (less than 1°) surface that extends basinward with no break in slope (Ahr, 1973). The environment flourished with sponges, crinoids, bryozoans, and brachiopods during the Osagean interval. Lime mud dominated the shallow-marine outer ramp and reefs were fringed along the distally steepened ramp margin. Algal reef deposits were eroded by the wave action and turbulent shallow water (Rogers, 2001),

likely leaving behind altered deposits. The lack of a definite break in slope along the distally steepened ramp allowed for shallow water deposits to transition and mix into deeper water deposits more readily (Read, 1985). Distally, the deposition of Meramecian-aged siliciclastic silt-sized material within the system is still highly debated. Price et al. (2017) hypothesized Meramecian deposition occurred from a subaqueous delta complex, whereas Leavitt (2018) alternatively suggests the deposition occurred from storm or turbidite flows transporting eolian-sourced silt and detrital carbonates. In both scenarios, depositional systems were dependent on sea level changes where drops in sea level correspond to siliciclastic sedimentation. Read (1985) suggested distally steepened ramps could be identified based on the presence of downslope gravity flows and mass transport deposits carrying shallower sediments basinward. The Mississippian represents a transitional period between the greenhouse conditions of the Devonian and the icehouse conditions that existed during the Pennsylvanian, in which the seas were regressing and global temperatures cooled (Read 1995; Buggisch et al., 2008) (Appendix A-2). An overall trend of falling sea level throughout most of the Mississippian led to the progradational wedges of carbonate/siliciclastic sediment toward the southeast comprised of higher frequency sea level driven deposits (Watney et al., 2001; Childress and Grammer, 2015; Jaekel, 2016; Price et al. 2017; Childress and Grammer, 2018). The sea-level changes were influenced by climate, tectonic activity, sedimentation rates, and variability of ice volumes in Earth's orbit (Read, 1995). As a whole, the Mississippian interval is considered to be a 2nd-order-regressive (5-50 Ma) sequence (Appendix A-3) (Sloss, 1963). The sequence is capped by the Pennsylvanian unconformity, which

represents the upper part of the Kaskaskia sequence of Sloss (1963). Higher-order cyclicity (third-, fourth- and fifth-order) has been interpreted in the Mississippian interval (e.g., LeBlanc, 2014; Price, 2014; Childress and Grammer, 2015; Flinton, 2016; Jaeckel, 2016; Price and Grammer, 2018). Milankovich-driven eustasy is the attributed driving force to these shorter, higher-order cycles; however, other controlling factors may also include: rates of sedimentation, short term (seasonal) climate variations tectonics (e.g., Read, 1995; Rogers, 2001; Watney et al, 2001; LeBlanc, 2014; Price, 2014; Flinton, 2016).

METHODS

Data Preparation, Acquisition, Normalization

Cores and wells were chosen based on stratigraphic and geographic distribution, quality, and accessibility. Wells were preferentially selected to ensure consistent spacing and contain a *triple-combo* (GR, RESD, DPHI, and NPHI). Additional wells with raster images of well logs were digitized using IHS *Petra* along dip and oblique-oriented transects. Electrofacies classification techniques are sensitive to the input well-log data; therefore, several quality-control tasks were conducted on the well logs to ensure reliable results. Well logs were resampled to a common 0.25 ft (0.08 m), and core-to-log depth shifts were applied to the cored wells. The well logs were also examined visually to remove obvious spikes or data associated with washouts. Gamma-ray logs were normalized using the base-line-shift method (Appendix D-1). Normalization was conducted in order to minimize variations in log acquisition caused by tool failures or

miscalibrations. Normalization was not completed on every well but only as needed, to not diminish the geologically significant trends within the interval.

Lithologies and Lithofacies

The dominant Mississippian lithologies and lithofacies (both proximal and distal) were determined by detailed core descriptions and integrating previously described cores within the study area. Three cores at Oklahoma Petroleum Information Center (OPIC), Gulf Oil 1-14 Musselman, Gulf Oil 1-23 Shaffer, and Gulf Oil 1-25 Rohling, were described in detail to determine the lithologies, lithofacies, sedimentary structures, grain size, fossils, color, texture, and bioturbation index (Appendix B). Cores descriptions from previous studies (Haynes, 2013; Birch, 2015; Lindzey, 2015; Flinton, 2016; Suriamin and Pranter, 2018) were adapted for this study. The cored wells include: Chesapeake 1-4 Bann, Devon Energy 1-8 Kirby, Devon Energy 1-7 Downing, Devon Energy 1-7 Frieouf, 1 Albert F. Severin, Pan American 1 Moore D Unit, Pan American 1 Effie B York, and Petrolia 1 Payne. Additionally, eight thin sections from the Gulf Oil 1-23 Shaffer, along with photomicrographs of the thin sections from other cores were also used to aid in the classification of the key lithologies. Porosity, permeability, and mineralogy using X-ray diffraction (XRD) data from core plugs helped to further classify the lithologies. Depositional environments were interpreted based on the lithologies and lithofacies characteristics observed in the cores.

Electrofacies Classification

Electrofacies classification techniques are used to integrate data from core with conventional well-log data to estimate lithologies. Fundamentally, the main goal of

electrofacies classification is to categorize depth intervals into similar groups based on their well-log signatures, so that specific log characteristics can be linked to lithologies to ultimately predict those lithologies in non-cored wells. Two electrofacies classification techniques were evaluated on their ability to accurately predict lithology using seven different permutations of GR, DPHI, NPHI, RESD, and porosity separation logs as inputs. These two methods include supervised (artificial neural network) and unsupervised (k-means clustering) methods.

Artificial Neural Network

Artificial neural network (ANN) is a supervised method that uses interpreted core data to train an algorithm to perform pattern recognition and interpretation. In this supervised method, ANNs iteratively minimize the difference between the user defined output and a predicted output by weighting and combining the input variables to create a lithology log that represents the core (Kumar and Kishore, 2006). The training set acts as a desired output, which is used to tune the predictive capability of the inputs selected (Anggraini and Puspa, 2008). Core descriptions from each well were used to train the ANN. The network learns the combination of input well logs for each lithology and uses 50% of the input data to train the estimation model. The remaining 50% of the input data were used to validate the accuracy of the resulting estimations. This process is then repeated and the weights are adjusted until a satisfactory match is achieved.

In this study, core descriptions from six wells were used to train the ANNs. The dip-oriented model (Appendix D-29) was divided into two regions: a proximal, up-dip area using ANNs based on the Chesapeake 1-4 Bann core, and a distal, down-dip area

using ANNs based on the Gulf Oil 1-23 Shaffer, Gulf Oil 1-25 Rohling, Gulf Oil 1-14 Musselman, and Petrolia 1 Payne cores. Similarly, the oblique-oriented model (Appendix D-30) was divided into two parts. The first was a proximal area using ANNs based on the Devon Energy 1-7 Downing, Devon Energy 1-8 Kirby, and Devon Energy 1-7 Frieouf cores. The second was a distal region using ANNs based on the Gulf Oil 1-23 Shaffer, Gulf Oil 1-25 Rohling, and Gulf Oil 1-14 Musselman cores. Overall accuracies for each input well-log assemblage in both dip-oriented and oblique-oriented models were evaluated, and the best performing ANN was applied to the non-cored wells in both regions and merged to illustrate the lithologies present across the transects.

To appropriately validate the predictive capability of an ANN, it is important to run "blind" tests, which test the results of an estimated output against the known values associated with hard data not used in the training process. Seven blind tests were conducted on both proximal and distal regions to determine the prediction accuracy of different log assemblages on an unused, or "blind" cored well. For the proximal region, only the oblique-oriented model had adequate core data to conduct a blind test. Seven different ANNs each based on distinct log input combinations trained from core data from the Devon Energy 1-7 Downing core (training set) were used to predict the lithology of the Devon Energy 1-8 Kirby core (testing well) (Appendix D-11 A). For the distal regions of both dip- and oblique-oriented models, the Gulf Oil 1-25 Rohling core was used as the training well, and the resulting ANNs were tested blindly on the Gulf Oil 1-23 Shaffer (Appendix D-11 B). The highest achieved blind test overall accuracies (77% and 84%, respectively) support the feasibility of using ANNs as a predictive tool to

estimate lithology. Combined ANNs using multiple core to train the estimation model were utilized instead to ensure all available data were utilized.

K-means Clustering

K-means clustering is a type of unsupervised learning, which is not conditioned to the core. The purpose of k-means is to classify the data set into groups or clusters. The number of clusters assigned is known as the K value. The algorithm works iteratively to assign each data point to one of the clusters that are based on the similarity or dissimilarity between the data points (Kanungo et al., 2002). It works by minimizing the sum of squared distances from each point to the centroid within each cluster. A cluster is defined by only one centroid and is initially randomly positioned among the data. Then, each centroid location is recomputed by taking the mean of all the data points assigned to that centroid's cluster and is repeated until each point is the closest it can be to the representative centroid of each cluster (Hartigan, 1975). The inputs used within the algorithm are well logs and the user-defined K value. Typically, the optimum K value should reflect the lithologies observed in core. However, if the cores do not represent all the lithologies present, the K value can be obtained experimentally by plotting the summed distance of data points to centroids for successively increasingly number of clusters, referred to as sum of squares between and the sum of squares within plot (SSB vs. SSW). The K value is determined at the elbow point, which is the inflection point where the slope of both lines decreases. This approach can also be used to validate the number of lithologies present. The plot in Appendix D-10 validates that the 6 core-based lithologies are also observed in the well logs.

Similar to the ANN process used within this study, the dip-oriented model (Appendix D-29) was divided into two regions using k-means: a proximal, up-dip, area based on the Chesapeake 1-4 Bann core, and a distal, down-dip area based on the Gulf Oil 1-23 Shaffer, Gulf Oil 1-25 Rohling, Gulf Oil 1-14 Musselman, and Petrolia 1 Payne cores. The oblique-oriented model (Appendix D-30) was also divided into two parts. The first was a proximal area using k-means based on the Devon Energy 1-7 Downing, Devon Energy 1-8 Kirby, and Devon Energy 1-7 Frieouf cores. The second was a distal region using k-means based on the Gulf Oil 1-23 Shaffer, Gulf Oil 1-25 Rohling, and Gulf Oil 1-14 Musselman cores. Overall k-means accuracies for each of the seven input combinations were then compared and evaluated using a confusion matrix.

Regional Cross Sections and Stratigraphy

To define the stratigraphic relationships within the Mississippian interval, the Kinderhook, Mississippi Limestone, Osage, and Meramec were correlated using one or more of the well logs (raster or digital) for 1255 wells: gamma-ray (GR), deep resistivity (RESD), neutron porosity (NPHI), density porosity (DPHI), bulk density (RHOB), photoelectric (PE), and classified lithology logs. Isopach and structure-contour maps were constructed to determine the lateral extent and thickness variation of the Kinderhookian, Osagean, and the Meramecian intervals. Existing formation tops from Mazzullo et al. (2009), Wilhite and Mazzullo (2013), Mazzullo et al. (2016), Price et al. (2017), Miller (2018), and Wethington and Pranter (2018) were used as appropriate for certain wells. The tops were correlated and adjusted by creating an approximate depositional-dip and oblique-oriented cross-sections across the study area. Due to the

elusiveness and disagreement on the location of the Osage top across the Anadarko Basin, the Osage top from Price et al. (2017) was used as a guide for correlation.

Finer scale correlations were also developed within the Meramec and Osage series. The finer scale correlations often correspond to stratigraphic cycles and were interpreted using a log-attribute analysis, called Derivative Trend Analysis (DTA). The objective of DTA is to identify the log responses that are geologically significant, by identifying and quantifying upward increasing or decreasing log patterns (Wethington and Pranter, 2018). DTA was applied to GR logs to identify intervals of the log that exhibit decreasing upward patterns that represent coarsening-upward intervals and intervals that exhibit an increasing upward pattern that represents a fining-upward interval. To apply DTA to the GR logs, the first step is to determine the suitable smoothing window in order to highlight geologically significant features. This could mean suppressing higher frequency log responses by applying a larger smoothing window or using smaller window to investigate finer scale trends. Once the smoothing window length is established, the Gaussian-smoothing function can be applied to the GR logs (Sharpiro and Stockman, 2000). The last step is to differentiate the smoothed GR curve using the central-difference method (Appendix E-1), which results in a curve that shows how the smoothed GR curve changes. For example, when the curve is positive, this means that the original GR curve is decreasing upward and when the curve is negative, the original GR curve is increasing upward. DTA was successively used to correlate these cycles within the study area (Figure 4). Different smoothing windows were used in different portions of the study area depending on the range in log values

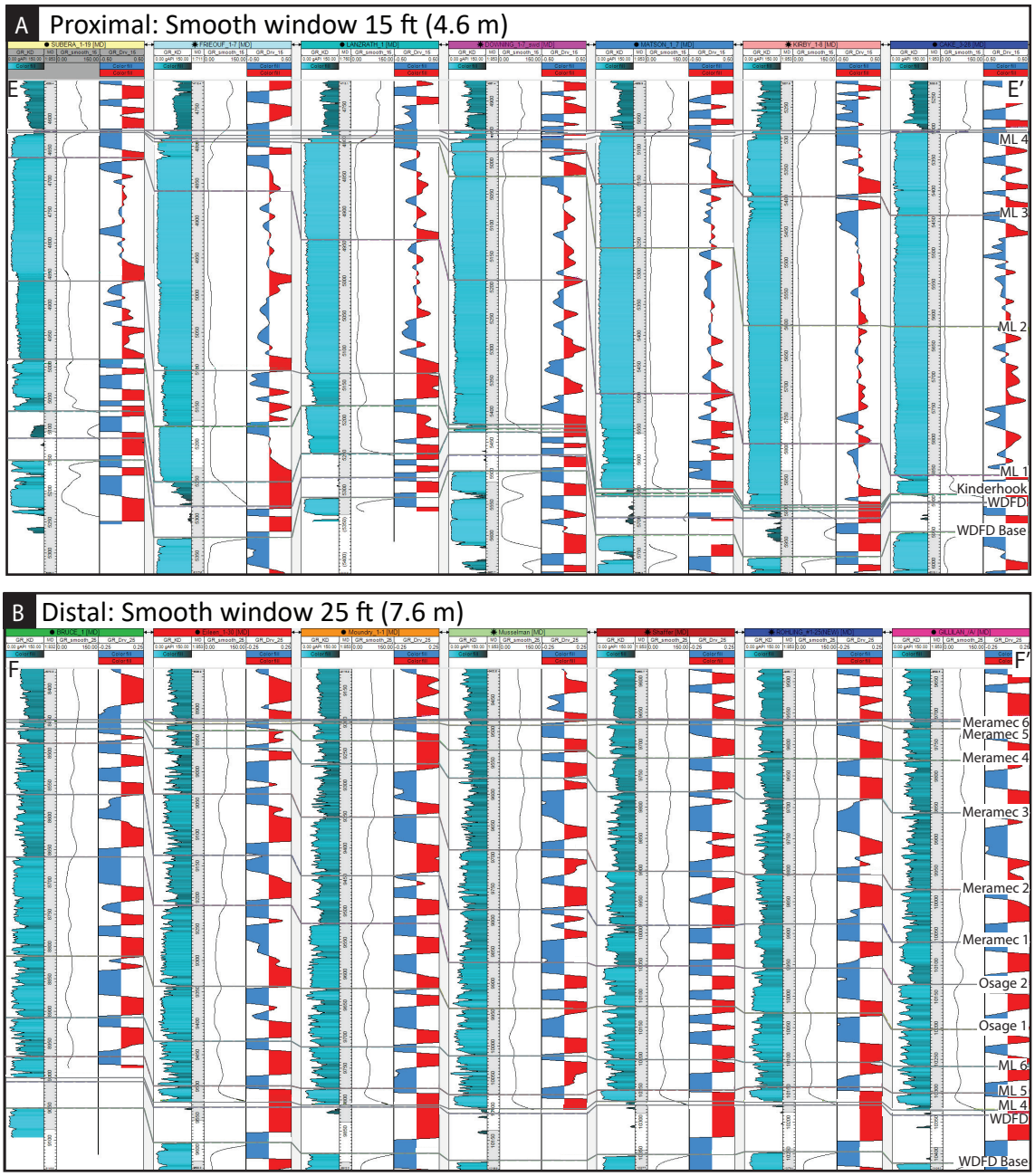

Figure 4: Example well-log correlations guided by GR-derivative curves using different smoothing windows. The left track is the original GR log, and the second track is the Gaussian-smoothed GR log (smoothing windows vary based on location within the study area). The third track is the GR derivative of the smoothed GR curve. Red represents positive values (GR is decreasing or cleaning upward) and blue represents negative values (GR is increasing of fining upward). (A) Proximal cross-section (E-E') (see Figure 3 for location) shows a shorter smoothing window of 15 ft (4.6 m). A smaller smoothing window is applied to investigate finer-scale stratigraphic trends. (B) Distal cross-section (F-F') (see Figure 3 for location) with a larger smoothing window of 25 ft (7.6 m). A larger smoothing window is applied to suppress high-frequency noise.

manifested in the lithologies present. DTA was also used in conjunction with other well logs such as RESD and DPHI to correlate the distinguishable log signatures across the study area.

Other curves including total porosity (PHIT), gamma ray (GR), deep resistivity (RESD), and porosity separation (PHISEP) were mapped to also aid correlation and to evaluate their spatial distribution throughout the study area. PHIT and PHISEP logs were calculated using the following equations:

$$PHIT = \sqrt{(NPHI^2 + DPHI^2)}$$

$$PHISEP = NPHI - DPHI$$

Using *Petra's* interpretative color-fill cross-section function, GR, RESD, and calculated PHIT and PHISEP curves were interpolated on each dip and oblique-oriented transects (Appendix E-4, 5, and 6). Wells included in the cross section were chosen to maintain approximately constant spacing to capture the changes in petrophysical properties and how they relate to lithologies. PHISEP was modeled to emphasize dolomitized as well as clay-rich intervals. PHIT and PHISEP curves were normalized as needed by the base-line shift method to the neighboring wells.

Lithology Modeling

By integrating core descriptions, stratigraphic correlations, carbonate depositional sequences and electrofacies classification results, dip- and oblique-oriented lithology models were created using *Petrel*. The models were created along projection lines oriented approximately perpendicular to the structure contours of the Woodford Shale upon which wells were projected (Figure 5). This was done to minimize structural

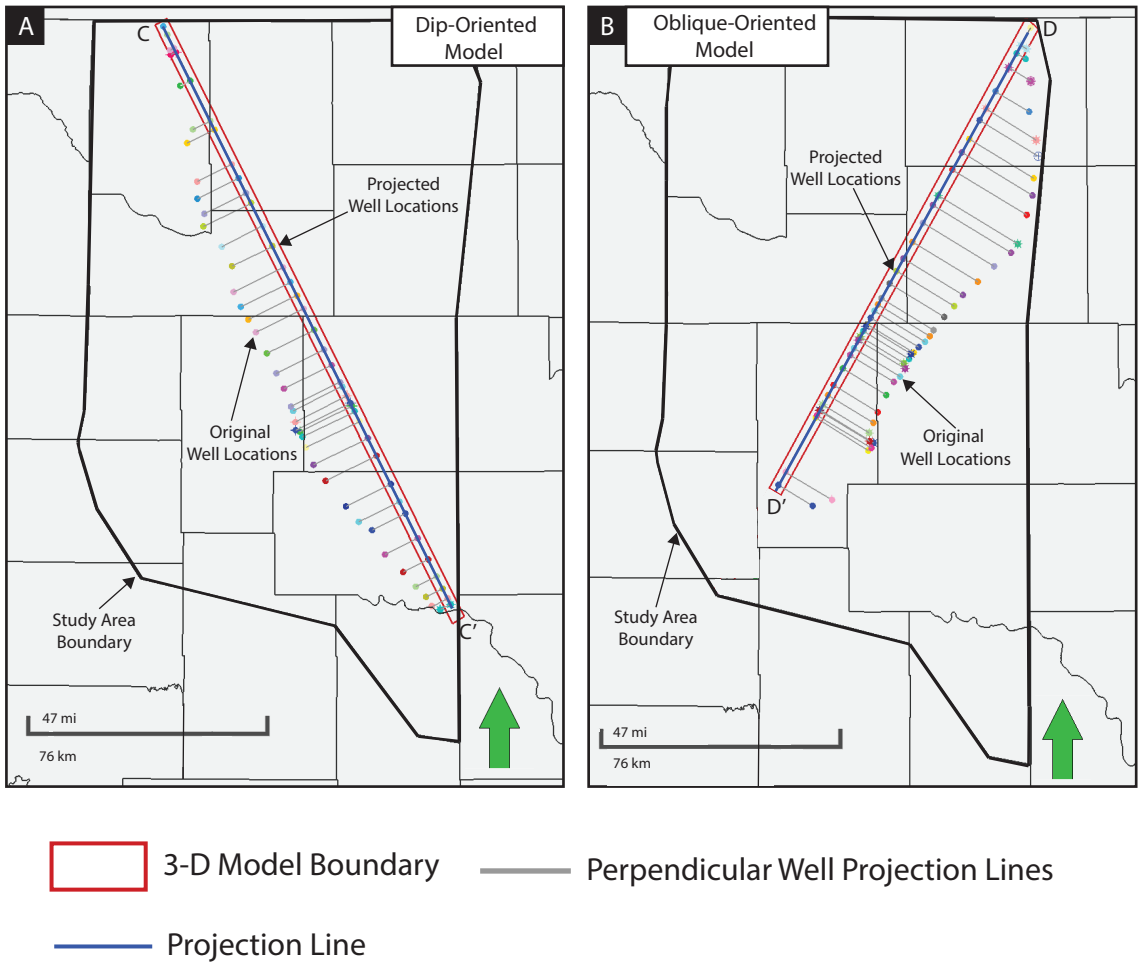

Figure 5: 3-D model locations. Wells were projected into the line of section, approximately perpendicular to the structure contours of the Woodford Shale, to minimize structural distortion. Models focused on cross-sectional variability and geometries rather than 3-D variability, hence the slender models, (A) Location of dip-oriented model. (B) Location of oblique-oriented model.

distortion in the model. Models were focused on the cross-sectional variability and geometries rather than the 3-D spatial variability, therefore slender models were created along each transect. The 3-D grid was created using the formation tops of each zone and flattened on the top of the Woodford Shale. The dip-oriented model covers 124 mi (200 km) and the oblique-oriented model covers 100 mi (160 km), each with an aerial cell size of 500 ft x 500 ft (152.4 m x 152.4 m), 16 stratigraphic zones, and 460 proportional layers. The average layer thickness of the dip-oriented grid is 1.5 ft (0.46 m), resulting in 52,497,500 cells. Similarly, the oblique-oriented grid has an average layer thickness of 1.7 ft (0.52 m) with 17,275,300 cells. Once the 3-D grid was created, the resulting lithology logs from the highest lithology estimation model were upscaled and populated to the model grid (flattened on top of the Woodford Shale). The modeled lithologies include chert, cherty limestone, calcareous siltstone, calcareous very-fine sandstone, and calcareous mudstone. If more than one lithology intersected a cell along the well path, the most abundant lithology was assigned to the cell. Sequential-indicator simulation (SIS) was used to model the spatial distribution of lithology. The models were constrained to upscaled ANN-derived lithology logs, lithology percentage histograms by zone, and horizontal and vertical variograms ranges by zone and lithology. Horizontal ranges were used to ensure geologically appropriate distances of correlation (Lindzey, 2015). Vertical ranges were estimated through variography with well logs. The experimental variograms ranges for each lithology and zone are summarized in Appendix D-27 and 28.

Porosity Modeling and Classification

Total porosity (PHIT) and porosity separation (PHISEP) were modeled to A) evaluate their spatial distribution, B) explore how they relate to lithology, and C) define potential controls on porosity distribution. Porosity models were created using sequential-Gaussian simulation (SGS). Each porosity model was constrained using the previously described 3-D lithology models, upscaled total porosity logs biased to lithology logs, histograms of total porosity by zone and for each lithology, and variogram parameters by zone and lithology. Variogram ranges were less for total porosity given the porosity heterogeneity within each lithology. The values are summarized in Appendix E-7 and 8.

Thin sections and photomicrographs were analyzed to determine the types of porosity present. Porosity classification was based on Choquette and Pray (1970) (Appendix B-4). In addition, petrophysical and grain composition information from core plugs, including porosity and permeability (ambient and at reservoir conditions) and XRD mineral percentages were used to further evaluate porosity relationships**.**

RESULTS

Proximal Lithologies, Lithofacies, and Pore Types

The proximal lithofacies of the Mississippian consist of eight dominant lithofacies including: 1) skeletal grainstone, 2) peloidal packstone to grainstone, 3) bioturbated wackestone to packstone, 4) bioturbated mudstone to wackestone, 5) dolomitized wackestone, 6) altered chert, 7) glauconitic sandstone, and 8) siliceous shale (Figure 6 and Figure 7) (Birch, 2015; Lindzey, 2015; Flinton, 2016; Suriamin and Pranter, 2018). Table 1 summarizes each lithofacies, including interpreted depositional environment,

Limestone/Cherty Limestone

A Skeletal Grainstone

B Pelodial Packstone to Grainstone

C Bioturbated Wackestone to Packstone

D Bioturbated Mudstone to Wackestone

E Dolomitized Wackestone

Chert

F Altered Chert

Sandstone

G Glauconitic Sandstone

Shale

H Siliceous Shale

Figure 6: Proximal Mississippian core-defined lithologies. (A) Skeletal grainstone (Devon Energy 1-8 Kirby 5352 ft [1631 m] MD), (B) peloidal packstone to grainstone (Devon Energy 1-8 Kirby 5557 ft [1694 m] MD), (C) bioturbated wackestone to packstone (Devon Energy 1-8 Kirby 5537 ft [1688 m] MD), (D) bioturbated mudstone to wackestone (Devin Energy 1-8 Kirby 5880 ft [1792 m] MD), (E) dolomitized wackestone (Chesapeake 1-4 Bann 5279 ft [1609 m] MD), (F) altered chert (Devon Energy 1-8 Kirby 5309 ft [1618 m] MD), (G) glauconitic sandstone (Devon Energy 1-7 Frieouf 5238 ft [1597 m] MD), (H) siliceous shale (Devon Energy 1-7 Frieouf 5279 ft [1609 m] MD).

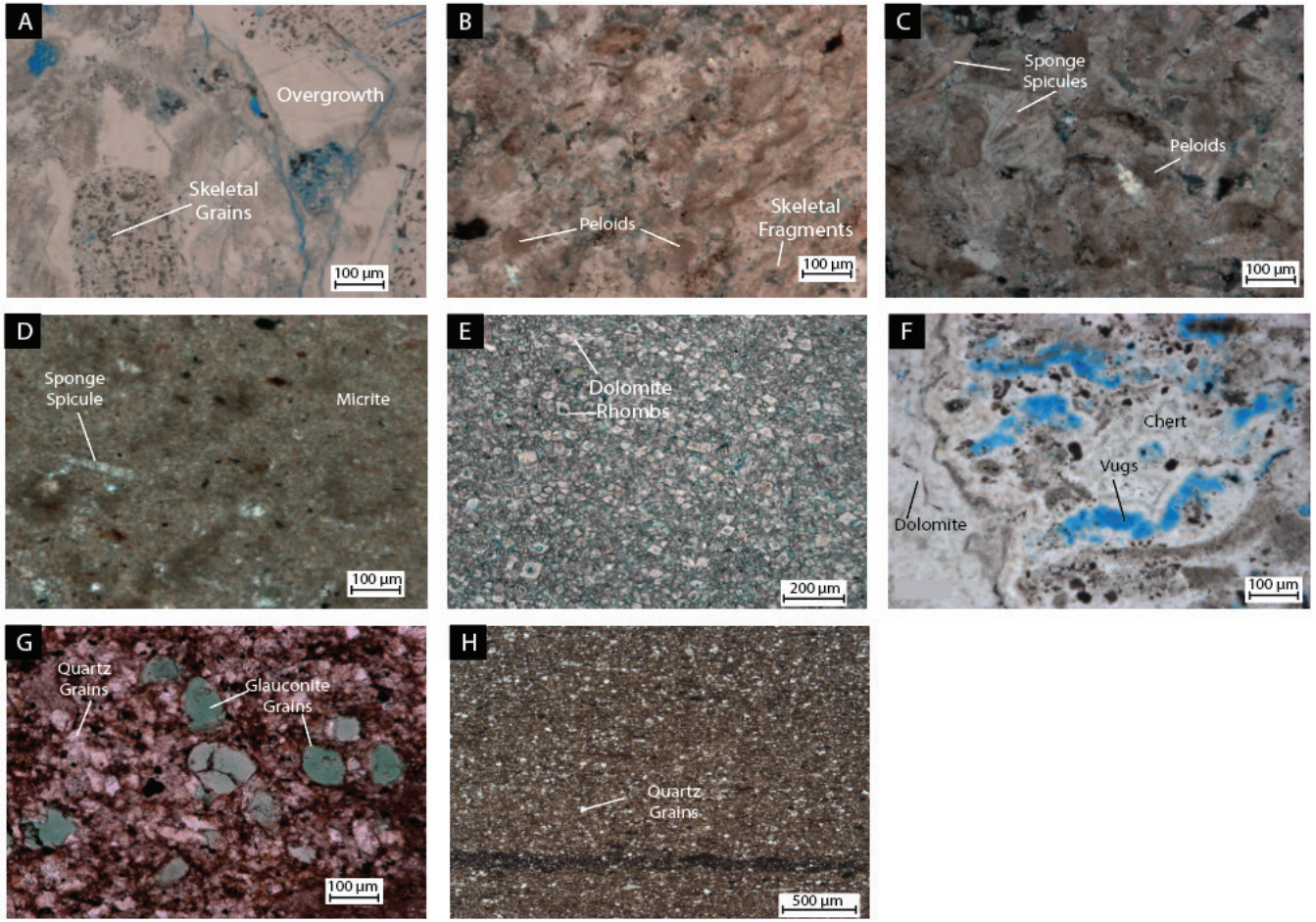

Figure 7: 3-Representative thin-section photomicrographs of the proximal Mississippian lithofacies. (A) Skeletal grainstone (Devon Energy 1-8 Kirby 5349.1 ft [1630.4 m] MD). (B) Peloidal packstone to grainstone (Devon Energy 1-8 Kirby 5557.7 ft [1694 m] MD). (C) Bioturbated wackestone to packstone (Devon Energy 1-8 Kirby 5807.8 ft [1770.2 m] MD). (D) Bioturbated mudstone to wackestone (Devon Energy 1-7 Downing 5887.35 ft [1794.5 m] MD). (E) Dolomitized wackestone (Chesapeake 1-4 Bann 5279.4 ft [1609.2 m] MD). (F) Altered chert (Devon Energy 1-8 Kirby 5309.3 ft [1618.3 m] MD). (G) Glauconitic sandstone (Devon Energy 1-8 Kirby 5877 ft [1791.3 m] (H) Siliceous shale (Devon Energy 1-7 Frieouf 5298.2 ft [1614.9 m] MD).

Lithologies	Lithofacies	Description	Depositional Setting
Limestone	Skeletal Grainstone	Light gray grain-supported, characterized by abundant fossils and fragments. Cherty zones are observed. No micrite	Skeletal Shoals near FWWB
	Peloidal Packstone to Grainstone	Medium gray, grain dominated, characterized by abundant peloids and skeletal grains. Some micrite present. Bioturbation frequent. Often silica replaced/cherty	Mid-ramp proximal to skeletal shoals near FWWB
	Bioturbated Wackestone to Packstone	Micrite is abundant. Chert sections throughout. Highly bioturbated. Peloids, spicules and shell fragments common	Distal Mid-ramp
	Dolomitized Wackestone	Medium to dark gray calcareous mudstone. Principle constituent is micrite. Abundant euhedral dolomite rhombs throughout and sometimes coupled with chert	Nearshore to Supratidal
	Bioturbated Mudstone to Wackestone	Calcareous mudstone. Principle constituent is micrite. Extensive bioturbation. Often cherty. Spicules present	Mid to outer ramp
Chert	Altered Chert	Angular grain supported chert. Silica replaced limestone. Often the original fabric has been completely destroyed from diagenesis related to subaerial exposure and fluid invasion	Subaerially exposed area near karsted terrain to nearshore settings
Sandstone	Glauconitic Sandstone	Fine-grained rounded glauconite grains encompassed in finer quartz grains matrix	Low oxygen and energy submarine environments
Shale	Siliceous Shale	Dark gray shale with occasional faint laminations. Mainly clay minerals with some silt-sized quartz grains	Outer ramp in deep water below SWB

Table 1: Summary of dominant proximal Mississippian lithofacies.

categorical lithologies, and identifying characteristics such as grain- or matrix-dominated and primary constituents. Interpreted depositional environments range from karst-prone region and subaerially exposed regions of the inner ramp to distal ramp environments (Figure 8). Appendix C-1 offers detailed proximal lithofacies descriptions and interpretations.

Common Pore Types – Proximal (Mississippian limestone)

Common pore types include: 1) interparticle, 2) intraparticle, 3) intercrystalline, 4) moldic, 5) vuggy, and 6) fracture (Figure 9) (Mazzullo, 2004; Lindzey, 2015; Birch, 2015; Vanden Berg and Grammer, 2016; Vanden Berg et al., 2017; Wethington and Pranter, 2018; Suriamin and Pranter, 2018). In the proximal area, the dominant pore types are vuggy, moldic, and fracture with minimal intercrystalline porosity. Vuggy porosity is most common owing to dissolution by fluids migration and is most prevalent in altered (tripolitic) chert (Figure 9A) (Suriamin and Pranter, 2018). Pore space is commonly occluded by silica cement (Figure 9H). Skeletal grainstones, peloidal packstones to grainstones, and bioturbated packstones often exhibit moldic to partially moldic porosity (Figure 9B). Proximally, fractures are the least common pore type (Figure 9C). Minor intercrystalline porosity is associated with dolomitized wackestones and cherty limestones (Figure 9D) (Mazzullo, 2004; Gao and Wang, 2017; Wang et al., 2017). Proximally, dissolution-related porosity is dominant and the magnitude of porosity and permeability is greater in Mississippian limestone than the down-dip Mississippian Osage and Meramec (Figure 10A).

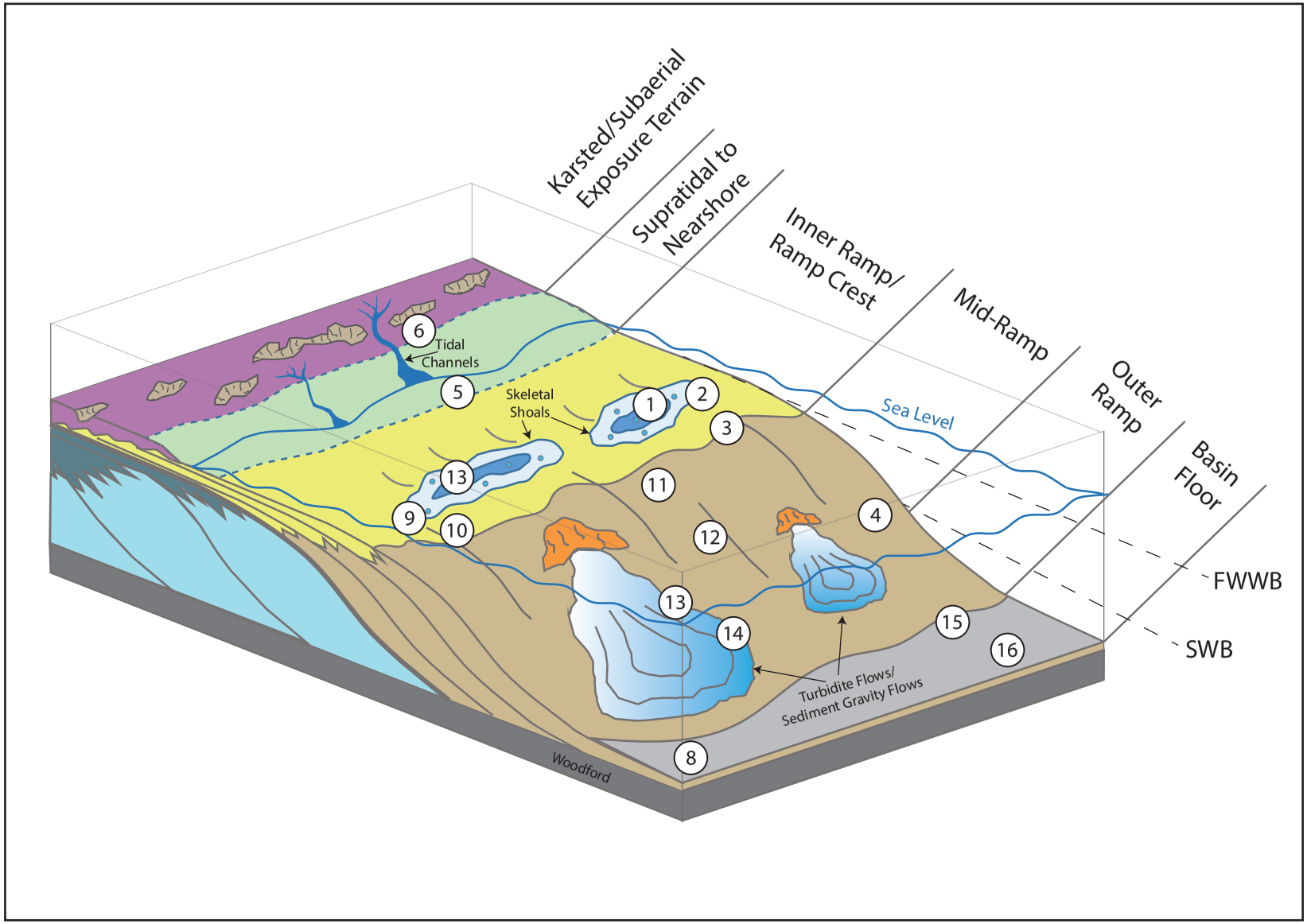
Karsted/Subaerial
Exposure Terrain
Supratidal to
Nearshore
Inner Ramp/
Ramp Crest
Mid-Ramp
Outer
Ramp
Basin
Floor
Sea Level
FWWB
SWB
Tidal
Channels
Skeletal
Shoals
Turbidite Flows/
Sediment Gravity Flows
Woodford
1
2
3
4
5
6
8
9
10
11
12
13
13
14
15
16

Figure 8: Schematic depositional model of the carbonate ramp and basin settings within the Mississippian strata across the study area and approximate interpreted depositional settings of each lithofacies, including: (1) Skeletal grainstone, (2) peloidal packstone to grainstone, (3) bioturbated wackestone to packstone, (4) bioturbated mudstone to wackestone, (5) dolomitized wackestone, (6) altered chert, (7) glauconitic sandstone, not shown due to the variation in depositional environments, (8) siliceous shale, (9) fossiliferous calcareous very-fine sandstone, (10) structureless calcareous very-fine sandstone, (11) bioturbated calcareous very-fine sandstone, (12) cross-bedded calcareous siltstone, (13) laminated calcareous siltstones, (14) bioturbated calcareous siltstone, (15) laminated calcareous mudstone, and (16) bioturbated calcareous mudstone.

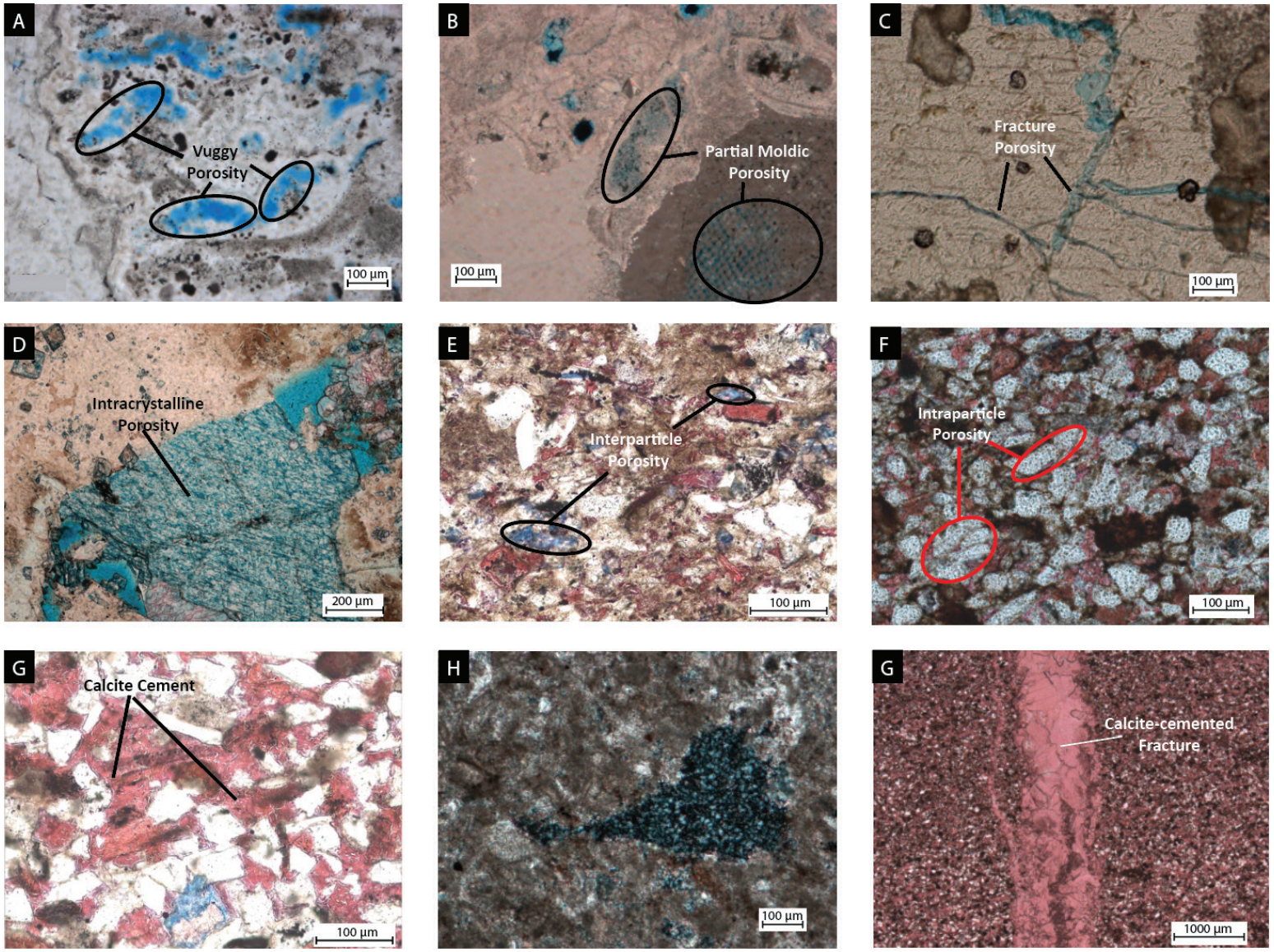
A
Vuggy
Porosity
100 µm
B
Partial Moldic
Porosity
100 µm
C
Fracture
Porosity
100 µm
D
Intracrystalline
Porosity
200 µm
E
Interparticle
Porosity
100 µm
F
Intraparticle
Porosity
100 µm
G
Calcite Cement
100 µm
H
100 µm
G
Calcite-cemented
Fracture
1000 µm

Figure 9: Dominant pore types for proximal and distal settings. (A) Vuggy porosity (Devon Energy 1-8 Kirby 5309.3 ft [1618.3 m] MD). (B) Partially moldic porosity within skeletal grains (Devon Energy 1-8 Kirby 5349.1 ft [1630.4 m] MD). (C) Fracture porosity (Devon Energy 1-7 Downing 5077.05 ft [1547.5 m] MD). (D) Intracrystalline porosity (Chesapeake 1-4 Bann 5273.56 ft [1607.4 m] MD). (E) Interparticle porosity (Gulf Oil 1-23 Shaffer 9681 ft [2950.8 m] MD). Contains 37 wt. % of carbonates and 20 wt. % clay with a porosity value of 3.8%. (F) Intraparticle porosity (Gulf Oil 1-23 Shaffer 9769.9 ft [2977.9 m] MD). (G) Interparticle porosity with calcite cement. Contains 58 wt. % of carbonates and 5 wt. % clay with a porosity value of 0.99%. (Gulf Oil 1-23 Shaffer 9781.2 ft [2981.2 m] MD). (H) Silicification of pore (Devon Energy 1-7 Downing 1-7 5037.45 ft [1535.4 m] MD). (I) Fracture calcite cement (Gulf Oil 1-23 Shaffer 9669.45 ft [2947.2 m] MD).

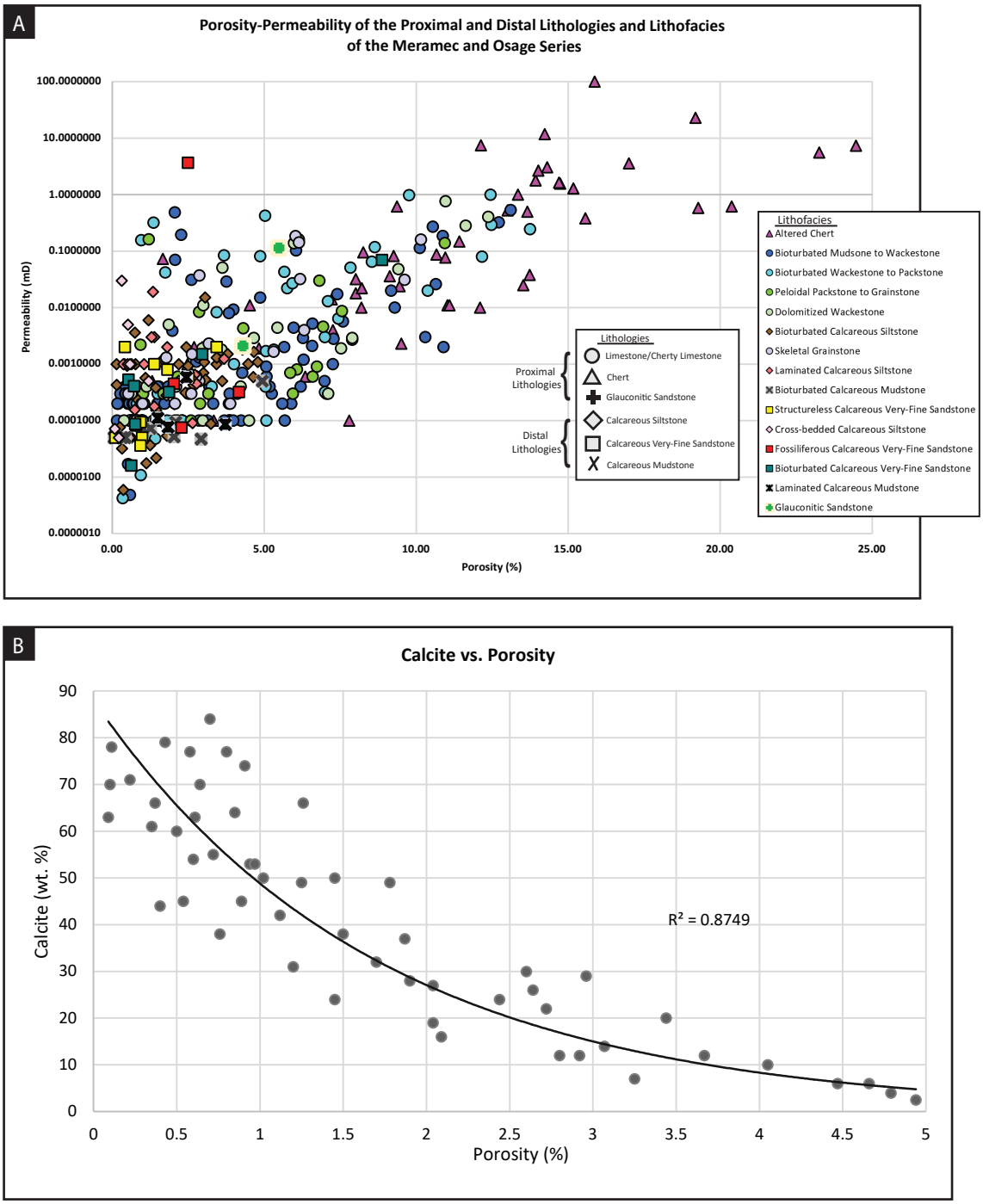

Figure 10: (A) Porosity-permeability cross plot measured from core plugs from 10 cores throughout the study area. Colors represent core-defined lithofacies. The cross-plot illustrates a reasonably good relationship between the lithofacies and reservoir properties. In general, the proximal lithofacies have relatively higher porosity values. Whereas the distal lithofacies have lower reservoir quality. (B) Cross plot of porosity vs. calcite content illustrates the negative relationship (values from 3 distal cores).

Distal Lithologies, Lithofacies, and Pore Types

The dominant distal lithologies of the Mississippian consist of eight lithofacies including: 1) fossiliferous calcareous very-fine sandstone, 2) structureless calcareous very-fine sandstone, 3) bioturbated calcareous very-fine sandstone, 4) laminated calcareous siltstone, 5) calcareous cross-bedded siltstone, 6) bioturbated calcareous siltstone, 7) laminated calcareous mudstone, and 8) bioturbated calcareous mudstone (Figures 11 and 12). Table 2 provides a summary of each lithofacies, including categorical lithologies, interpreted depositional environments, and defining characteristics such as primary grains and sizes, dominant fossils, bioturbation index, and sedimentary structures. Distal interpreted depositional environments range from inner ramp settings to the basin floor (Figure 8). Detailed descriptions and interpretations of the distal lithofacies are in Appendix C-2.

Common Pore Types – Distal (Mississippian Osage and Meramec)

Distally, the dominant pore types are interparticle, intraparticle, and fracture. Unlike in the proximal area, fractures are solely calcite-cemented (Figure 9I). Intraparticle porosity is primarily within quartz grains, where portions of each grain have been partially dissolved (Figure 9F). The most common porosity type is interparticle (Figure 9E and G). Interparticle porosity is negatively affected by cementation and compaction. Calcite cement is common (Figure 9G); however, where some clay is present, there tends to be preservation of porosity (Figure 9E).

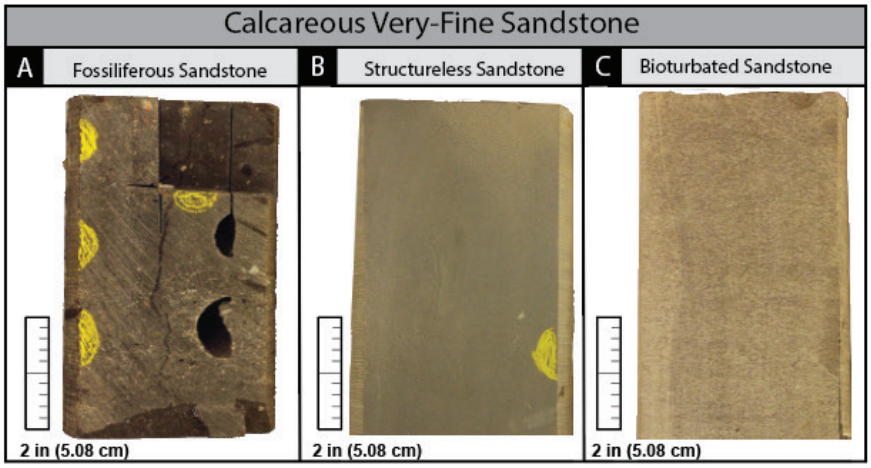
Calcareous Very-Fine Sandstone
A
Fossiliferous Sandstone
B
Structureless Sandstone
C
Bioturbated Sandstone
2 in (5.08 cm)
2 in (5.08 cm)
2 in (5.08 cm)

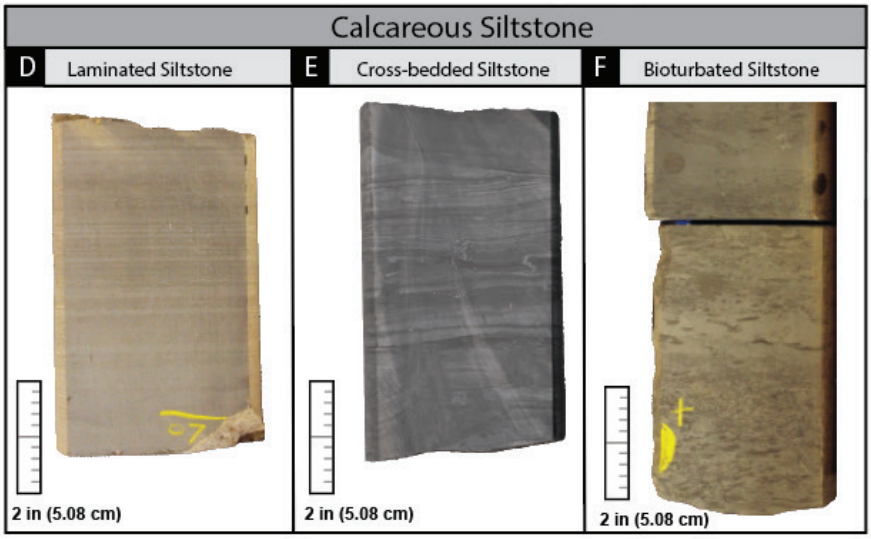
Calcareous Siltstone
D
Laminated Siltstone
E
Cross-bedded Siltstone
F
Bioturbated Siltstone
2 in (5.08 cm)
2 in (5.08 cm)
2 in (5.08 cm)

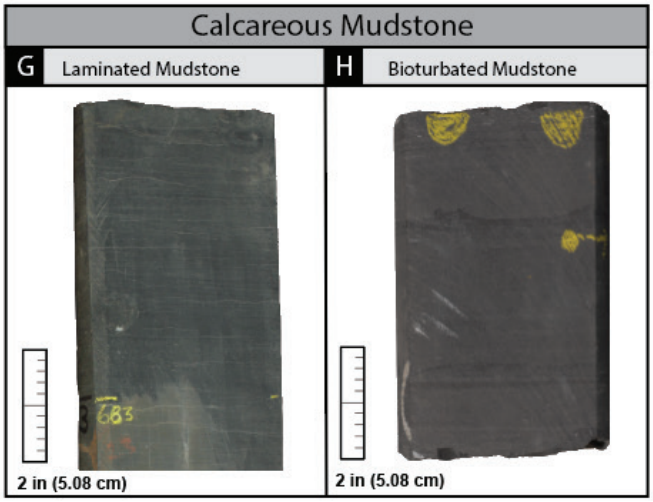
Calcareous Mudstone
G
Laminated Mudstone
H
Bioturbated Mudstone
2 in (5.08 cm)
2 in (5.08 cm)

Figure 11: Distal Mississippian core-defined lithologies. (A) Fossiliferous calcareous very-fine sandstone (Gulf Oil 1-23 Shaffer 9696 ft [2955 m] MD), (B) structureless calcareous very-fine sandstone (Gulf Oil 1-25 Rohling 9721.5 ft [2963 m] MD), (C) bioturbated very-fine calcareous sandstone (Gulf Oil 1-23 Shaffer 9660 ft [2944 m] MD), (D) laminated calcareous siltstone (Gulf Oil 1-25 Rohling 9906.5 ft [3020 m] MD), (E) cross-bedded calcareous siltstone (Gulf Oil 1-23 Shaffer 9675.5 ft [2949 m] MD), (F) bioturbated calcareous siltstone (Gulf Oil 1-25 Rohling 9841 ft [3000 m] MD), (G) laminated calcareous mudstone (Gulf Oil 1-23 Shaffer 9663 ft [2945 m] MD), and (H) bioturbated calcareous mudstone (Gulf Oil 1-23 Shaffer 9704 ft [2958m] MD).

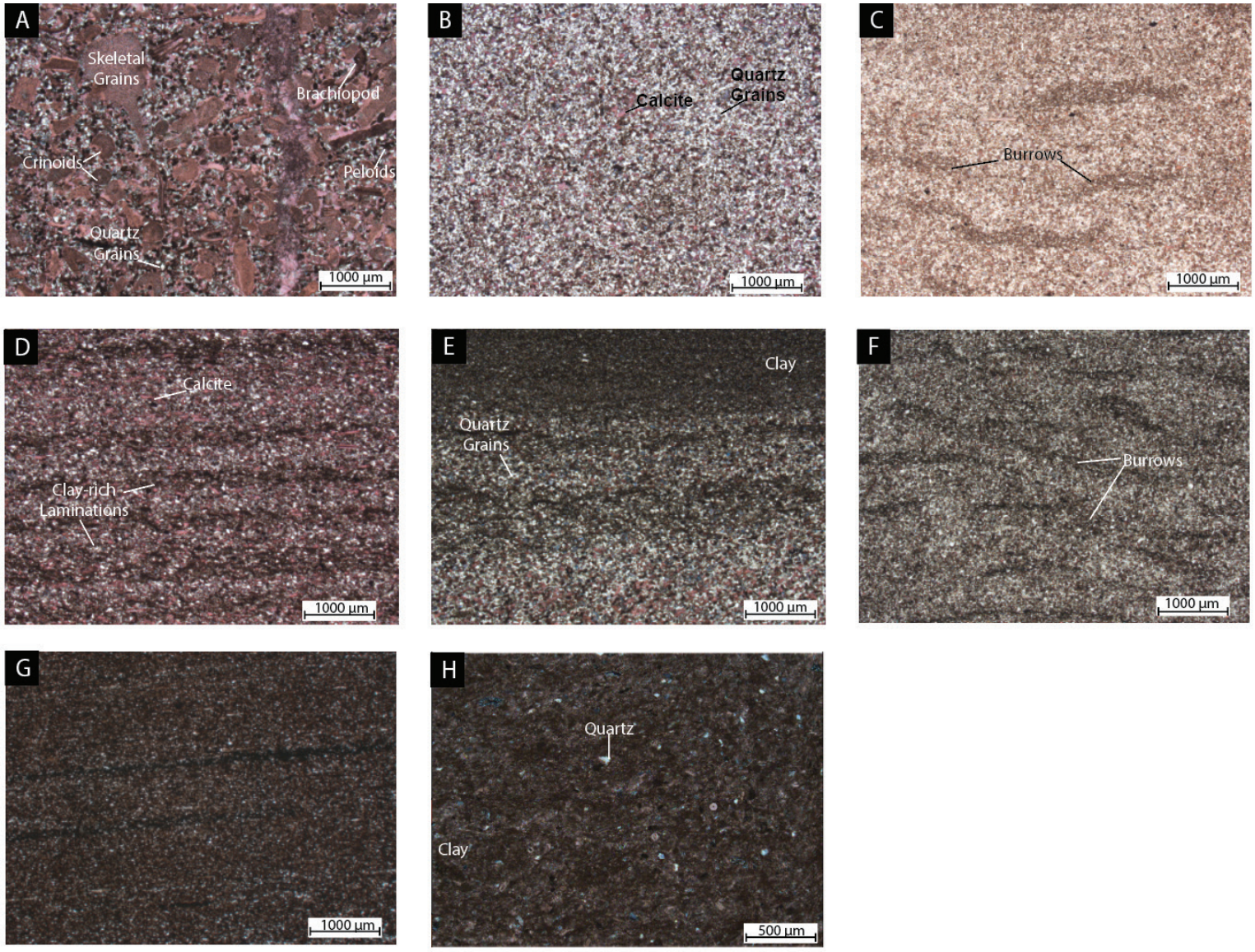
A
Skeletal Grains
Brachiopod
Crinoids
Peloids
Quartz Grains
1000 µm
B
Calcite
Quartz Grains
1000 µm
C
Burrows
1000 µm
D
Calcite
Clay-rich Laminations
1000 µm
E
Clay
Quartz Grains
1000 µm
F
Burrows
1000 µm
G
1000 µm
H
Quartz
Clay
500 µm

Figure 12: Representative thin section photomicrographs of the distal Mississippian lithofacies. (A) Fossiliferous very-fine calcareous sandstone (Gulf Oil 1-23 Shaffer 9665 ft [2945.9 m] MD). (B) Structureless very-fine calcareous sandstone (Gulf Oil 1-23 Shaffer 9725 ft [2664.2 m] MD). (C) Bioturbated very-fine calcareous sandstone (Gulf Oil 1-25 Rohling 9920.15 ft [3023.7 m] MD). (D) Laminated calcareous siltstone (Gulf Oil 1-23 Shaffer 9677.85 ft [2949.8 m] MD). (E) Cross-bedded calcareous siltstone (Gulf Oil 1-23 Shaffer 9670.6 ft [2947.6 m] MD). (F) Bioturbated calcareous siltstone (Gulf Oil 1-23 Shaffer 9807.85 ft [2989.4 m] MD). (G) Laminated calcareous mudstone (Gulf Oil 1-23 Shaffer 9675 ft [2948.94 m] MD). (H) Bioturbated calcareous mudstone (Gulf Oil 1-14 Musselman 9968.6 ft [3038.4 m] MD).

Lithologies	Lithofacies	Description	Depositional Setting
Very Fine Calcareous Sandstone	Fossiliferous Sandstone	Medium gray, very-fine sized quartz grains. Abundant fossils and fragments. Calcite cemented.	Inner to mid-ramp within FWWB
	Structureless Sandstone	Light gray, very-fine sized quartz grains. Abundant calcite cement. Predominantly structureless with occasional calcite cemented fractures	Mid-ramp within FWWB
	Bioturbated Sandstone	Medium to light gray, very-fine sized quartz grains, calcite cemented. Moderately bioturbated. Some fossil fragments.	Mid-ramp within FWWB
Calcareous Siltstone	Laminated Siltstone	Characterized by planar laminations. Mainly silt-sized quartz grains with some clay. Some fossil fragments. Calcite cementation observed.	Transition from mid to outer-ramp within FWWB/ turbiditie flows
	Cross-bedded Siltstone	Characterized by hummocky cross-stratification. Mainly silt-sized quartz grains. Some fossil fragments. Calcite cementation observed.	Transition from inner to mid-ramp within FWWB
	Bioturbated Siltstone	Medium to dark gray. Silt-sized quartz grains and clays. Calcite cemented. Some fossil fragments. Extensively bioturbated. Some argillaceous-rich zones observed.	Transition from mid to outer-ramp within FWWB/ turbiditie flows
Calcareous Mudstone	Laminated Mudstone	Composed of clay minerals and calcite with some silt-sized quartz grains. Characterized by faint planar laminations.	Deep waters of the basin floor – within SWB
	Bioturbated Mudstone	Composed clay minerals and calcite with some silt-sized quartz grains. Characterized by some bioturbation.	Deep waters of the basin floor – below SWB

Table 2: Summary of dominant distal Mississippian lithofacies.

Electrofacies Classification

Lithofacies are characterized by fine-scale properties such as sedimentary structures, bioturbation, and bedding types which do not exhibit unique well-log signatures. Therefore, lithofacies were grouped into their categorical lithologies to improve the prediction accuracy of lithology in non-cored wells. Classification models were created based on 1) shale, 2) limestone, 3) cherty limestone, 4) cherty, 5) calcareous very fine sandstone, 6) calcareous siltstone, and 7) calcareous mudstone.

Prior to applying the classification model to non-cored wells, the electrofacies classification techniques were evaluated on their ability to accurately predict the lithologies present. The accuracy of ANN and k-means was achieved by comparing the estimated lithologies to the core lithologies in a confusion matrix (Ting 2011). The confusion matrix compares the actual lithology from core to the predicted classes and depicts the number of successful and unsuccessful lithology classifications (Appendix D-12 to Appendix D-25). Dividing the number of successfully classified lithologies by the total number of predicted lithologies produces the overall accuracy of the classification. Individual accuracies of each class, known as user's accuracies, are obtained by dividing the number of correctly predicted instances for a particular class by the actual number of instances for that class (Janssen and van der Wel, 1994). ANN (supervised) and k-means (unsupervised) electrofacies classification techniques were compared to determine the highest user's accuracy and overall accuracy of lithologies to apply to the non-cored data set to model. Appendix D-2 to Appendix D-9 contains the visual comparison of the

cored-wells used the estimation models. Figure 13 summarizes the overall cumulative accuracies of the seven different well-log input permutations.

Using artificial neural networks (ANN), the highest overall accuracy of 85% was achieved using GR, DPHI, and NPHI inputs for the dip-oriented section (Figure 13 A). User's accuracies for this case were 72% for calcareous mudstone, 80% for limestone, 97% for cherty limestone, 82% for chert, 90% for calcareous siltstone, and 75% for calcareous sandstone (Figure 14 A). Figure 14-A2 shows the confusion matrix of the five cores combined ANN using GR, NPHI, and DPHI depicting lower accuracies and confusion in differentiating calcareous mudstone and calcareous sandstone. Due to the similarities in these lithologies, generally only differing in the amount of quartz grains within the matrix and the size of the grains present, the classification model tended to confuse them. Small-scale sedimentary features, minute differences in grain size, in addition to the thin-bedded nature (commonly 1 in [2.5 cm]) of the rocks observed are difficult to detect given the resolution of the logging tools (highest resolution down to 6 in [15 cm] for density tool and up to 4 ft [1.2 m] for resistivity tools depending on vintages). For the oblique-oriented section, the highest overall accuracy of 83% was achieved using GR, DPHI, and NPHI curves (Figure 13 B). User's accuracies for this case were 72% for calcareous mudstone, 78% for limestone, 86% for cherty limestone, 85% for chert, 91% for calcareous siltstone, and 77% for calcareous sandstone (Figure 14 B). Figure 14-B2 shows the confusion matrix of the six-core combined ANN using GR, NPHI, and DPHI, depicting lower accuracies and confusion in differentiating limestone and cherty limestone. The matrix indicated that the cherty limestone and the limestone

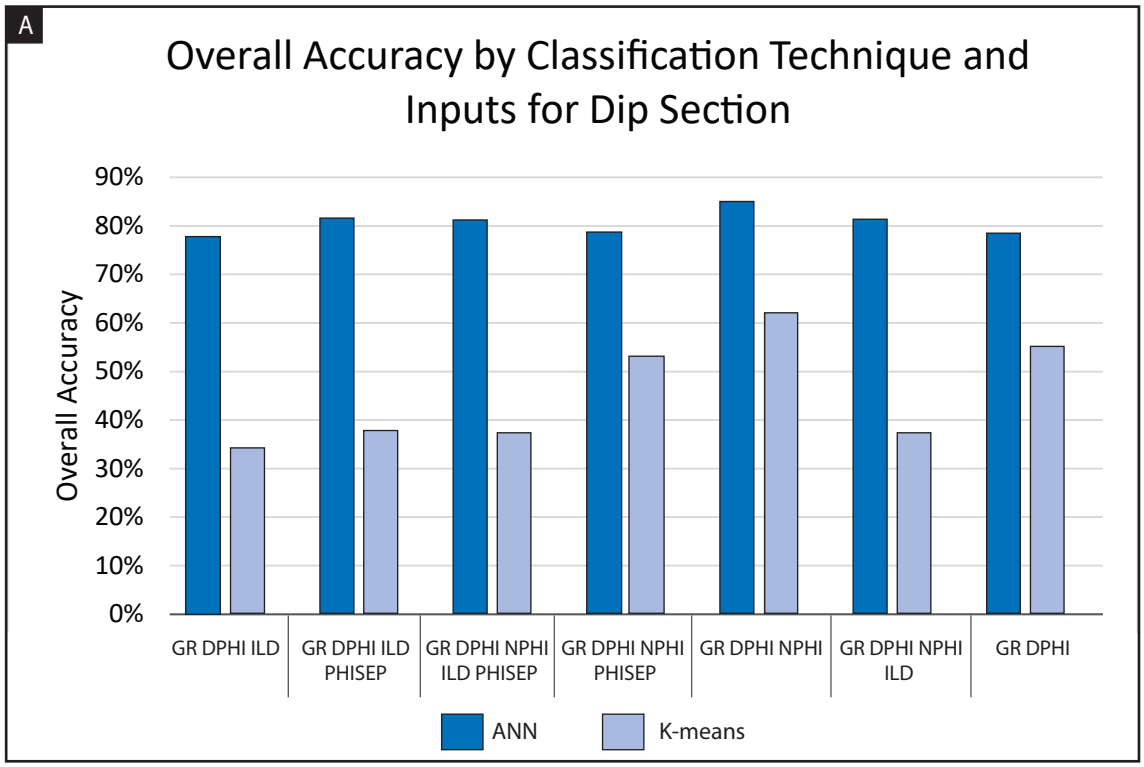
A
Overall Accuracy by Classification Technique and Inputs for Dip Section
Overall Accuracy
90%
80%
70%
60%
50%
40%
30%
20%
10%
0%
GR DPHI ILD
GR DPHI ILD PHISEP
GR DPHI NPHI ILD PHISEP
GR DPHI NPHI PHISEP
GR DPHI NPHI
GR DPHI NPHI ILD
GR DPHI
ANN
K-means

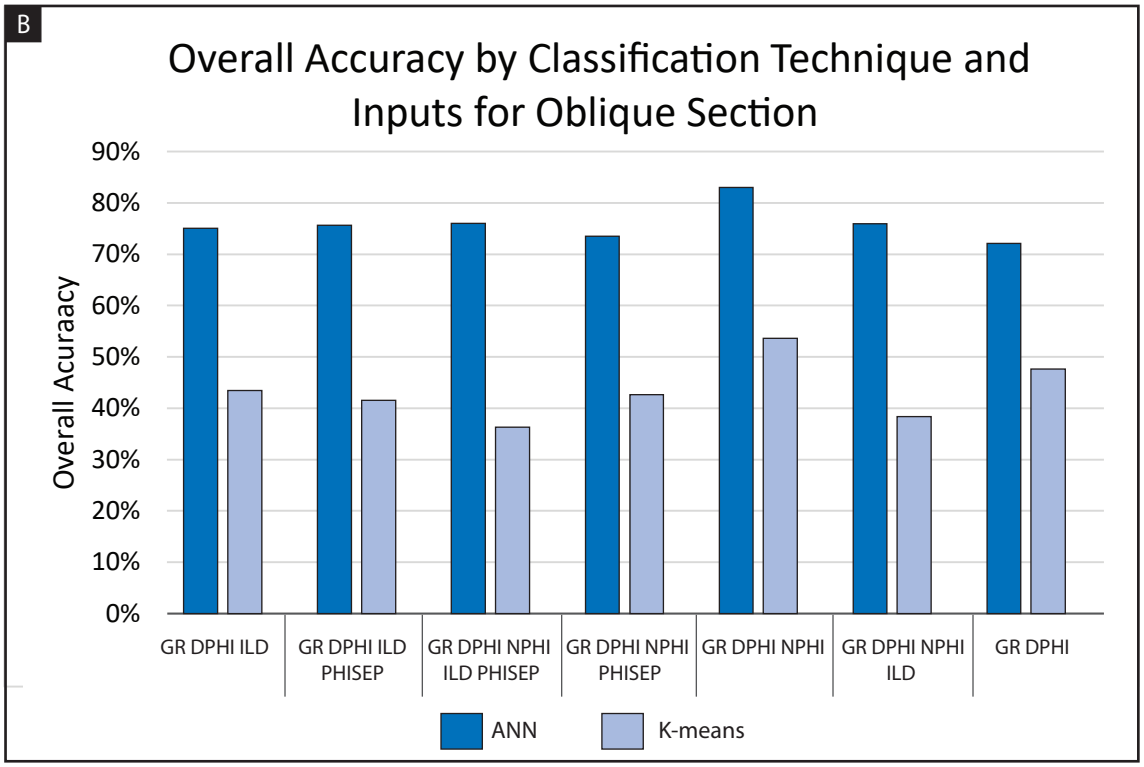
B
Overall Accuracy by Classification Technique and Inputs for Oblique Section
Overall Acuraacy
90%
80%
70%
60%
50%
40%
30%
20%
10%
0%
GR DPHI ILD
GR DPHI ILD PHISEP
GR DPHI NPHI ILD PHISEP
GR DPHI NPHI PHISEP
GR DPHI NPHI
GR DPHI NPHI ILD
GR DPHI
ANN
K-means

Figure 13: Comparison of overall accuracies of lithology classification methods between ANNs and k-means for each set of well-log input combinations (GR: Gamma Ray, RESD: Deep Resistivity, DPHI: Density Porosity, NPHI: Neutron Porosity, PHISEP: Porosity [NPIH-DPHI] Separation). The chart is used to compare how well each set of well-logs for each method predicts lithologies. (A) Overall accuracy from the dip-oriented (C-C') line of section using 33 wells. (B) Overall accuracy from the oblique - oriented (D-D') line of section using 37 wells.

A

A1

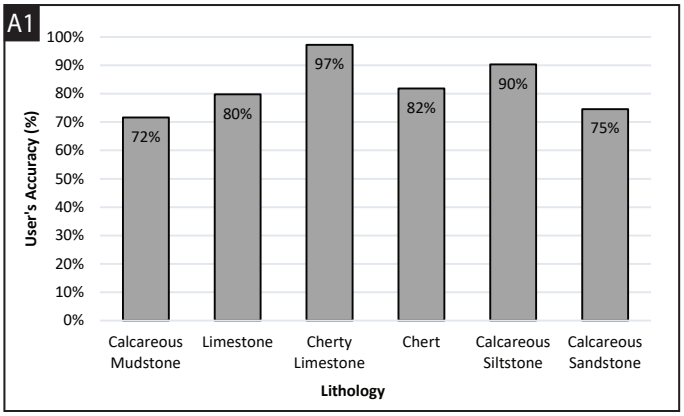

A2

Predicted Lithologies	Actual Lithology					
	Calcareous Mudstone	Limestone	Cherty Limestone	Chert	Calcareous Siltstone	Calcareous Sandstone
Calcareous Mudstone	262	0	0	0	39	1
Limestone	1	75	5	3	0	0
Cherty Limestone	0	19	245	22	0	0
Chert	0	0	2	113	0	0
Calcareous Siltstone	102	0	0	0	1165	187
Calcareous Sandstone	1	0	0	0	86	552
Accuracy	**72%**	**80%**	**97%**	**82%**	**90%**	**75%**

B

B1

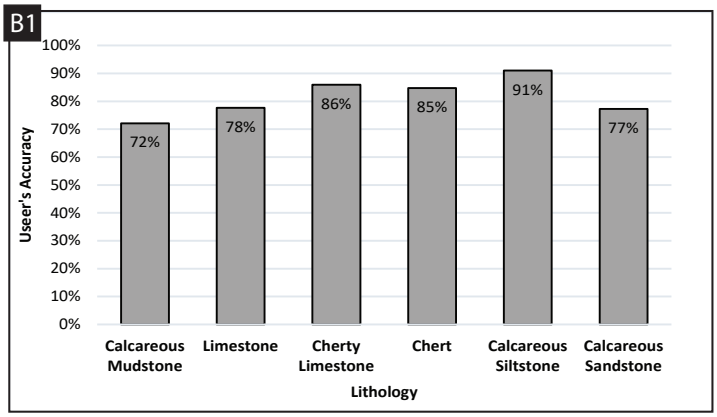

B2

Predicted Lithologies	Actual Lithology					
	Calcareous Mudstone	Limestone	Cherty Limestone	Chert	Calcareous Siltstone	Calcareous Sandstone
Calcareous Mudstone	411	6	24	22	23	0
Limestone	4	1579	307	3	0	0
Cherty Limestone	24	446	2437	94	0	0
Chert	5	3	67	660	0	0
Calcareous Siltstone	125	0	0	0	1046	153
Calcareous Sandstone	1	0	0	0	80	520
Accuracy	**72%**	**78%**	**86%**	**85%**	**91%**	**77%**

Figure 14: Accuracy of ANN for (A) dip-oriented and (B) oblique-oriented data sets. (A1) User's accuracy histogram illustrating how well each lithology was predicted using ANN in the dip-oriented (C-C') section using GR, DPHI and NPHI for 5 cores. Cherty limestone and calcareous siltstones were predicted very well with accuracies over 90%, while chert and calcareous mudstone were not as easily identified. (A2) Confusion matrix with user's accuracies as well as common misclassification errors. Dark grey colored cells represent correctly classified classes, while all other cells indicate incorrect classifications. Calcareous mudstone is often misclassified as calcareous siltstone, while calcareous siltstones were confused with both calcareous mudstones and calcareous very-fine sandstone lithologies. (B1) User's accuracy histogram illustrating how well each lithology was predicted using ANN in the oblique-oriented (D-D') section using GR, DPHI and NPHI for 6 cores. Cherty limestone and calcareous siltstone are predicted very well with accuracies from higher than 85%, while calcareous mudstone was not as easily classified. (B2) Confusion matrix with user's accuracies as well as common misclassification errors. Dark grey colored cells represent correctly classified classes, while all other cells indicate incorrect classifications. Calcareous mudstone is often misclassified as calcareous siltstone, while cherty limestone is confused with both chert and limestone. Similar plots for ANN and k-means techniques are in Appendices D-12 to D-25.

were getting confused, likely due to the similar and often interbedded nature of these lithologies. The primary difference between these lithologies is the content of silica present, while the logs used as inputs (GR, DPHI, NPHI) struggled to identify this difference, it is plausible that additional logging tools may differentiate this compositional variation (photoelectric). The ANNs yielded fairly consistent results, but some tended to be more negatively affected by the RESD log which could indicate a presence of different fluid types within the zones subsequently affecting the accuracies. Consequently, the lowest overall accuracy of the ANN classification method across both transects was 73%, which included a RESD curve.

Similarly, k-means clustering had the highest overall accuracy using the same inputs (GR, DPHI, NPHI) as the ANN method but was much lower (62%) in the dip-oriented model. The associated user's accuracies were 73% for calcareous mudstone, 41% for limestone, 83% for cherty limestone, 66% for chert, 55% for calcareous siltstone, and 63% for calcareous sandstone (Appendix D-13). For the oblique-oriented model, the overall accuracy using k-means was 54% using GR, DPHI, and NPHI logs. The associated user's accuracies were 85% for calcareous mudstone, 69% for limestone, 33% for cherty limestone, 4% for chert, 52% for calcareous siltstone, and 62% for calcareous sandstone (Appendix D-23). The other log input combinations had much lower accuracies as compared to the ANNs at predicting lithologies. K-means produced low, unreliable results with the lowest overall accuracy of the k-means classification method across both transects being 34%.

The use of a constrained and incomplete data set can lead to inherent limitations with these models but generally its predictability power can stimulate meaningful results. Some limitations of electrofacies classifications techniques are discussed in Appendix D-26. Overall, in this study, the supervised electrofacies classification method of ANNs provides higher accuracies when compared to the unsupervised k-means method. The ANN model with the highest overall accuracy using the well-log assemblage of GR, DPHI, and NPHI was used to derive lithology logs in the non-cored wells for both the dip- and oblique-oriented sections.

Regional Stratigraphic Framework

The regional stratigraphic framework of the lower Mississippian is interpreted through well-log correlations guided by core data, classified lithology logs and DTA curves. Three Mississippian units are evaluated: Kinderhook, Osage, and Meramec (Appendix E-2). The thickness of the Mississippian intervals ranges from 35 ft (10.7 m) to 1235 ft (376.4 m) and generally thickens to the southwest and west and thins to the east and southeast near the Nemaha Uplift and Ardmore Basin, respectively (Appendix E-3).The interval is subdivided into sixteen stratigraphic zones that were correlated across the study area. Figure 15 shows the regional stratigraphic correlations in the approximate dip (Figure 15A-C) and oblique (Figure 15D-F) orientations. Cross-sections reveal the progradational architecture based on distinct GR, RESD, and porosity signatures.

The Kinderhook overlies the Woodford Shale and is primarily a siliceous shale-rich interval that is characterized by relatively high GR values (>135 API). The boundary

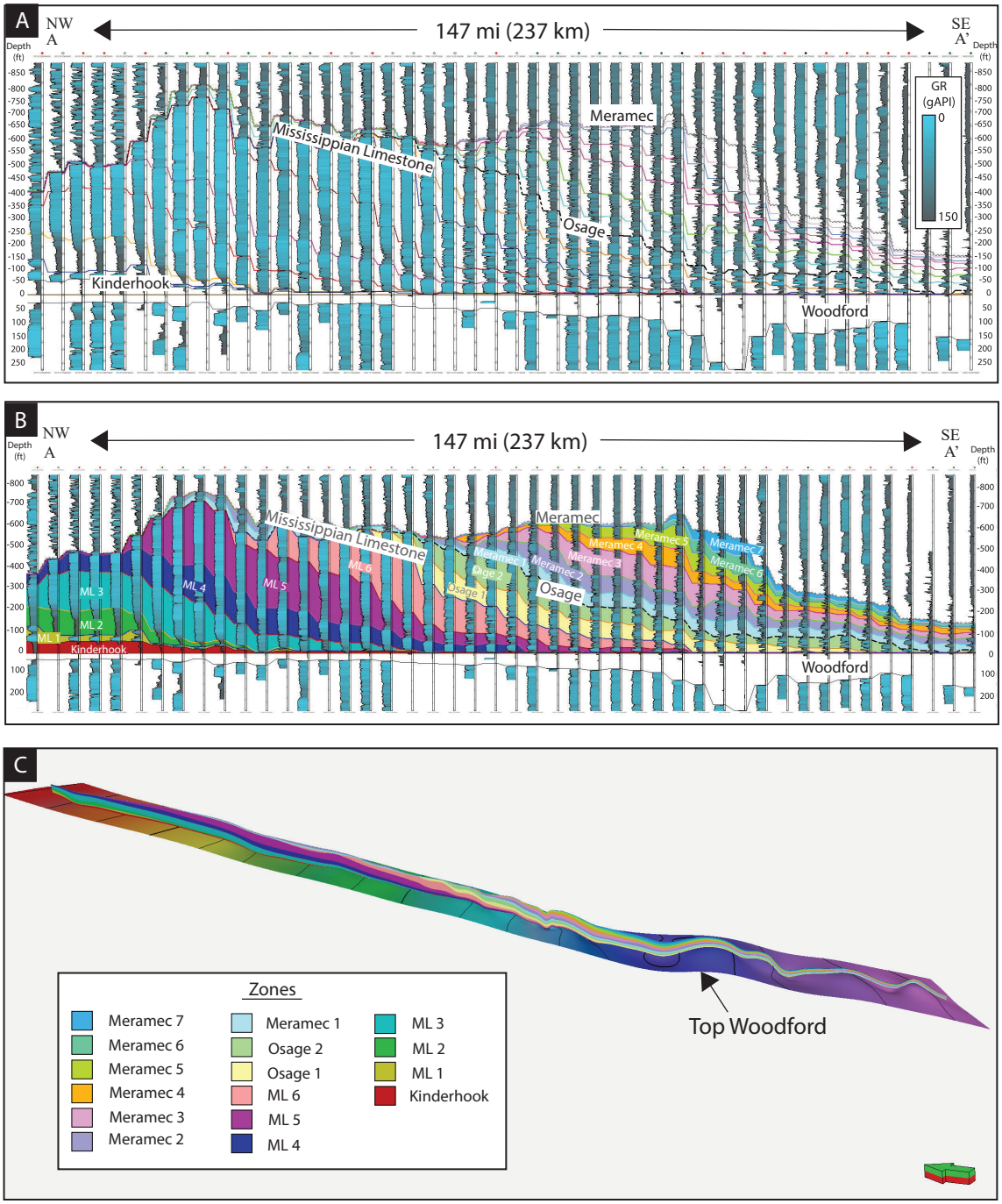

Figure 15: (A) Dip-oriented cross-section A-A' flattened on top of Woodford Shale. Stratigraphic interpretation illustrates changes in GR log character associated with lithologic and depositional environment variations. Cross-section illustrates proximal to distal (basinward) thinning of zones. (B) Same line of section as A illustrating the geometries of the internal stratigraphy. Note the progradational nature of the zones. (C) 3-D model of stratigraphic zones of equivalent section in A and B showing structural variation across the study area.

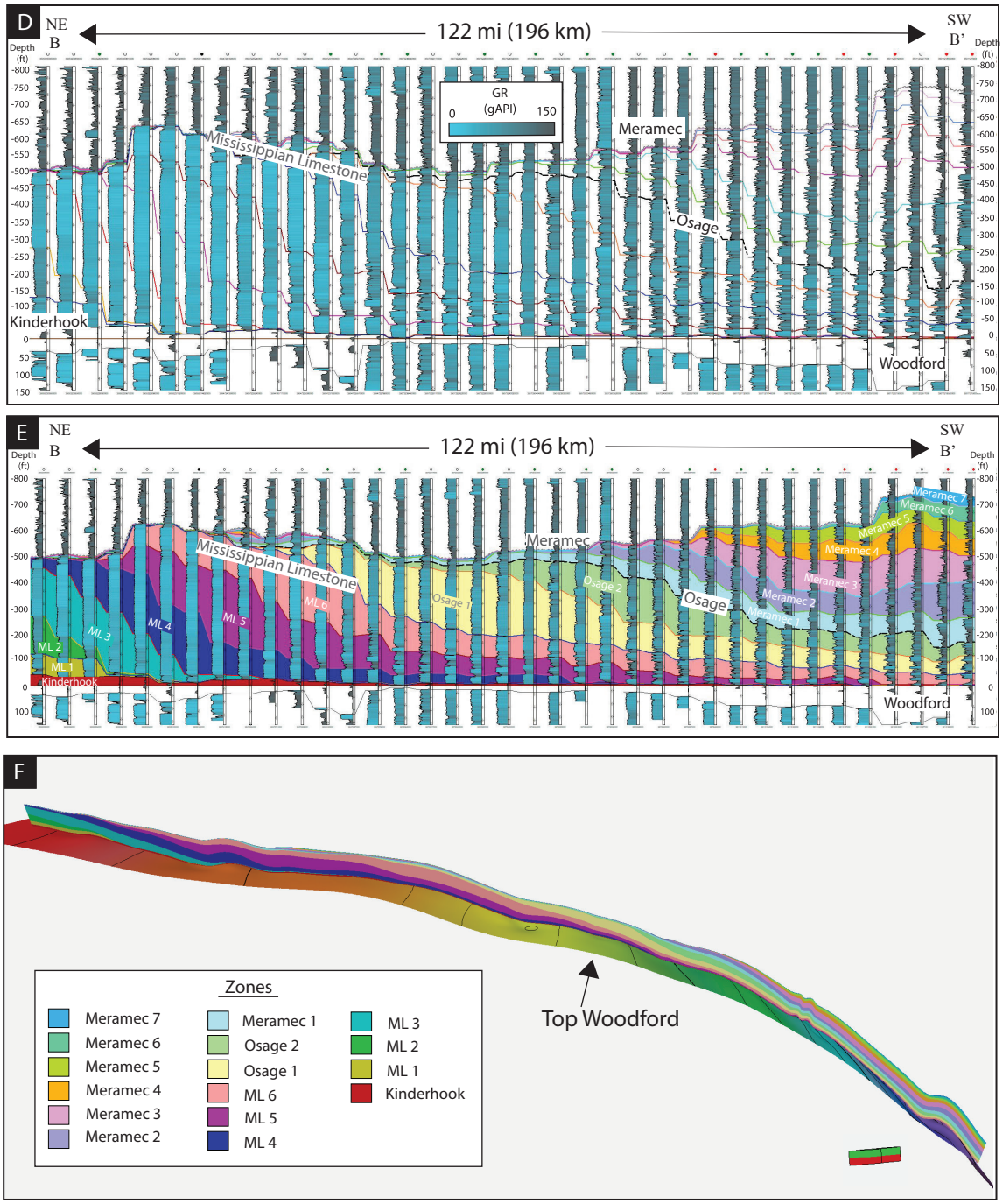

Figure 15 cont'd.: (D) Oblique-oriented cross-section B-B' flattened on the top of Woodford. Stratigraphic interpretation illustrates changes in GR log character associated with lithologic and depositional environment variations. Cross-section is in the approximate direction of paleo-oblique and shows increased thickness to the southwest. (E) Same line of section as D, illustrating the geometries of the internal stratigraphy. (F) 3-D model of stratigraphic zones of equivalent section in D and E showing structural variation in the oblique transect.

between the Kinderhook and the Woodford Shale corresponds to a significant increase in GR values, from 130-145 gAPI to greater than 250 gAPI. The Kinderhook shale differs from the Woodford Shale in the quartz content observed from lower GR units and core observations compared to the Woodford Shale. The Kinderhook thickness ranges from 80 ft (24 m) to 0 ft (0 m), thinning to the south (Figure 16C).

The Osagean was divided into the Mississippian limestone and the Osage based on differences in log character and core samples. The term "Mississippi Lime" is an informal term that refers to the Mississippian-aged strata up-dip in southern Kansas and northern Oklahoma which is characterized by *in-situ* carbonates within the system. The Mississippian limestone interval represents carbonate-dominated cycles that prograde to the southeast and consist of limestones, cherty limestones, cherts, and mudstones (Figure 15 and Figure 17). The interval is divided into six zones based on correlative interruptions in high RESD values (Appendix E-4) and exhibit basinward-dipping clinoforms (Figure 17). The Osage interval represents a transitional zone from the Mississippian limestone into the clastic-dominated system down-dip, which is characterized by continued prograding sequences of siltstone-rich and detrital carbonate sediments shed from the *in-situ* carbonate ramp of the Mississippian limestone onto the up-dip carbonate wedge (Figure 15 and 17) (Leavitt, 2018). The Osage has not been biostratigraphically constrained; therefore, Price et al. (2017) provides a basis for picking the Osage top from low GR values (<35-45 gAPI) coupled with relatively high resistivity values (RESD values >100 ohms) (Appendix E-4) as compared the surrounding strata. The Osage is divided into two zones based on correlative distinct GR trends and breaks in

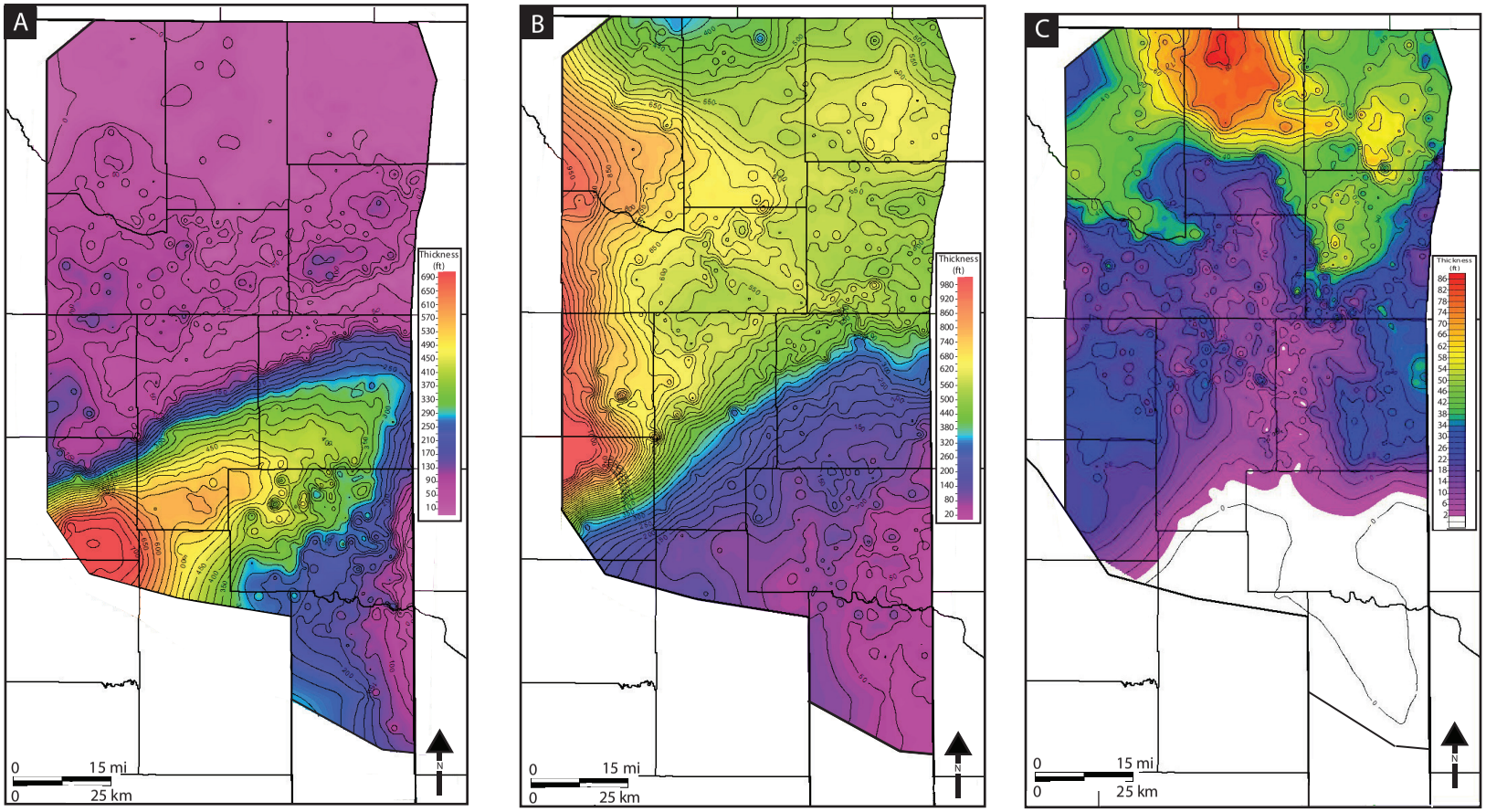

Figure 16: Isopach maps of Meramec, combined Mississippian limestone and Osage interval, and Kinderhook. (A) Meramec isopach. Contour interval is 25 ft (7.6 m). The Meramec is thin to the north and thickens to the south forming an elongate NE-SW trend. (B) Isopach map of combined Mississippian limestone and Osage interval. Contour interval is 25 ft (7.6 m). Mississippian limestone and Osage progrades to the southeast and thins to the south. (C) Kinderhook isopach. Contour interval is 10 ft (3 m). The Kinderhook thins to the south and eventually pinches out.

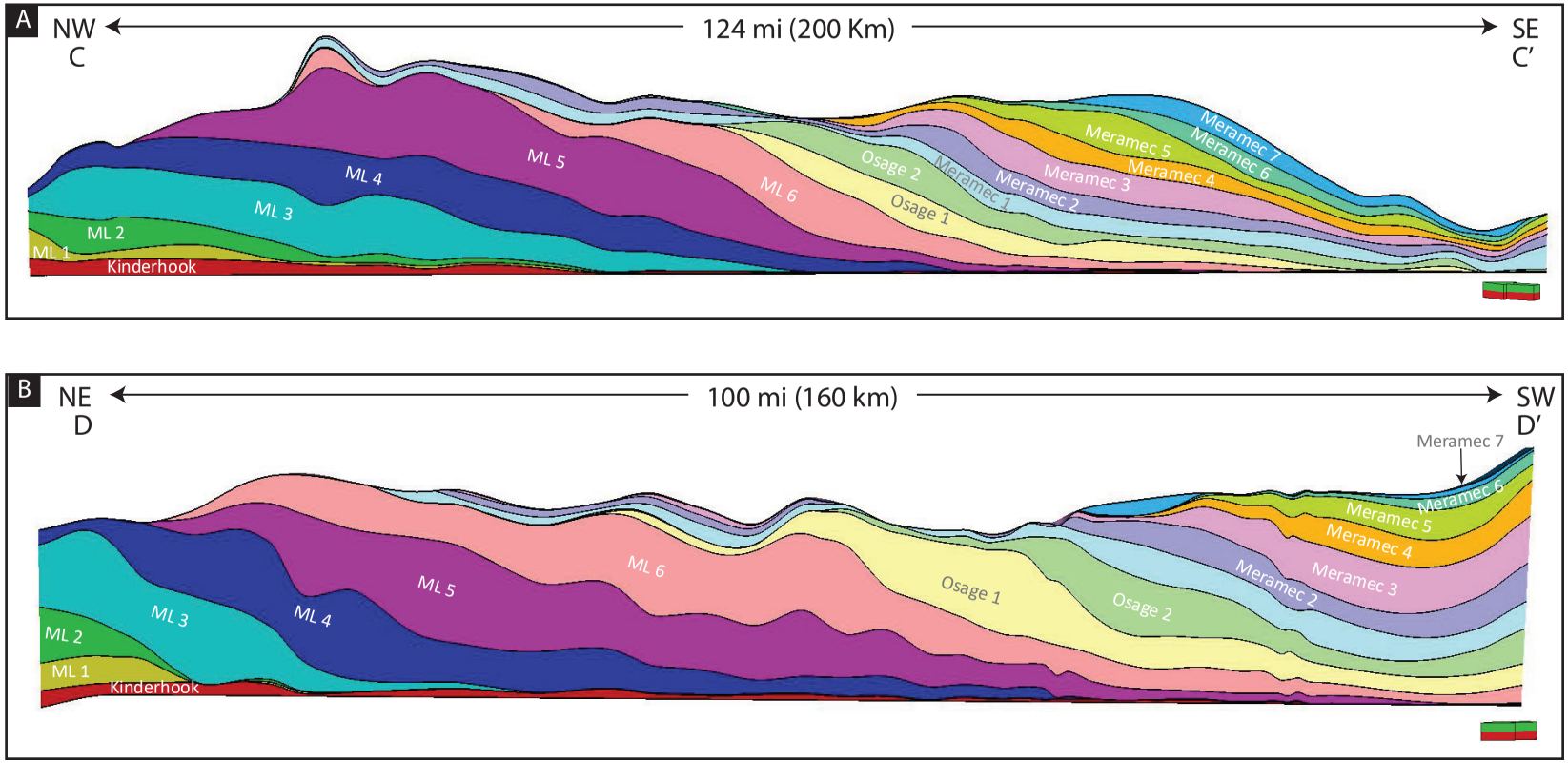

Figure 17: (A) Dip-oriented model (C-C') showing progradational Mississippian stratigraphic architecture (flattened on top of Woodford Shale). (B) Oblique-oriented model (D-D') showing Mississippian stratigraphic architecture (flattened on top of Woodford Shale). Stratal geometries of the Mississippian limestone and Osage reveals prograding clinoforms, while the Meramec represent both onlapping and prograding wedges.

high RESD and exhibits an on-lapping geometry. The thickness of the Mississippian limestone and the Osage ranges from 850 ft (260 m) in the west to less than 10 ft (3 m) in the southwest and gradually thins to the southeast and is absent in the southern portion of the study area in Grady County (Figure 16B).

The Meramec thickens to the south and is very thin to absent in the northern portion of the study area. The Meramec overlies the limestone and chert-rich Osage and the thickness ranges from 0–665 ft (0–203 m) (Figure 16A). The top of the Meramec corresponds to a regionally correlative increase in RESD and drop in DPHI and NPHI relative to the overlying Chester. The Meramec is divided into seven zones based on correlative flooding surfaces. The zones consist of calcareous siltstones, mudstones and very-fine grained sandstones. The Meramec intervals represent onlapping and prograding calcareous siltstones and mudstones (Figure 15 and 17). More specifically, the Meramec zones 1-3 represent onlap of the sequences onto the Osage carbonate ramp, with an overall fining-upward vertical succession. Whereas, the Meramec zones 4-7 represent prograding sequences with a coarsening upward vertical succession. The average GR map for the Meramec and Osage intervals shows the approximate location of the major change in GR values that corresponds to the transition from dominantly Osagean carbonates (low GR values) to Meramecian clay-rich siltstones (higher GR values) (Figure 18).

Several shallowing-upward depositional cycles are defined for the Meramec and Osage series (LeBlanc, 2014; Birch, 2015; Flinton 2016; Price et al., 2017; Miller, 2018; Price and Grammer, 2018). Cycles are interpreted based on the vertical stacking patterns

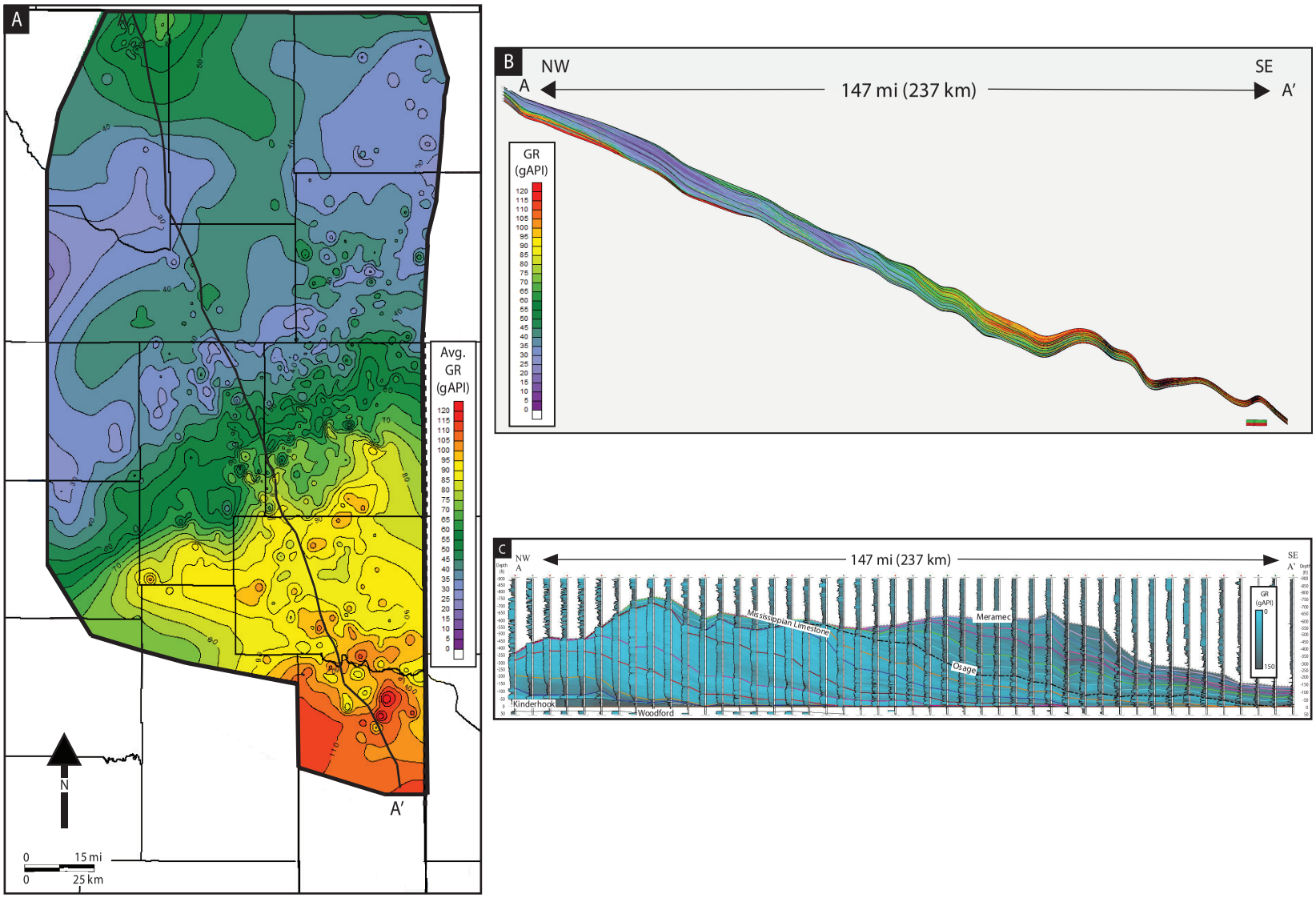
A
Avg. GR (gAPI)
120
115
110
105
100
95
90
85
80
75
70
65
60
55
50
45
40
35
30
25
20
15
10
5
0
A'
N
0 15 mi
0 25 km
B
NW
A
147 mi (237 km)
SE
A'
GR (gAPI)
C
NW
A
147 mi (237 km)
SE
A'
Mississippian Limestone
Meramec
Osage
Kinderhook
Woodford
GR (gAPI)
0
150

Figure 18: (A) Average gamma ray (GR) API for the interval from the top of Meramec to top of Woodford Shale. Contour interval is 10 ft (3 m). Major shift in GR values corresponds to the transition from dominant Osage carbonates (low GR values) up-dip on the shelf to silt-rich Meramec with higher clay content (higher GR values) down-dip into the basin. (B) Structural dip-oriented 3-D GR model from A to A' illustrating the variability in GR values down-dip. (C) Stratigraphic view of the (GR) interpretative dip-oriented A-A' cross-section flattened on the top of Woodford Shale with regional stratigraphic correlations that illustrate the changes the in GR log character associated with lithologic and depositional environment variations. Light blues reflect greater carbonate content and grays correspond to more clay content. The low GR values up-dip transition into higher GR values down-dip related to the system change from carbonate-rich to more clastic-dominated.

observed in core and gamma-ray derivative trends (Figure 19). The coarsening and upward-shallowing depositional cycles are observed in well logs as upward deceasing GR motif interrupted by a sharp increase in GR at the top of each cycle. By comparing GR, DTA curves and core descriptions, generally more detailed cycles are observed core than what is suggested from logs, especially in the proximal area (Figure 19). Proximally, the idealized facies succession (base to top) consists of siliceous shale, glauconitic sandstone, bioturbated mudstone to wackestone, bioturbated wackestone to packstone, peloidal packstone to grainstone, skeletal grainstone, and altered chert (Figure 19) (Birch, 2015; Flinton, 2016; Suriamin and Pranter, 2018). Distally, the idealized facies succession (base to top) consists of siliceous shale, bioturbated calcareous mudstone, laminated calcareous mudstone, bioturbated calcareous siltstone, laminated calcareous siltstone, cross-bedded calcareous siltstone, bioturbated calcareous very-fine sandstone, structureless calcareous very-fine sandstone, and fossiliferous calcareous very-fine sandstone (Figure 19). Such cycles are often frequently irregular or incomplete across the entire study area likely due to an incomplete rock record owing to erosion, diagenetic processes, and non-deposition. Due to the large aerial extent of the study area and observed lateral facies changes, individual cycles are expected to change in character (lithologic and log response), making them difficult to correlate across a large area. However where idealized successions occur, these stacked facies manifest as shoaling upward decreasing GR response with generally increasing porosity.

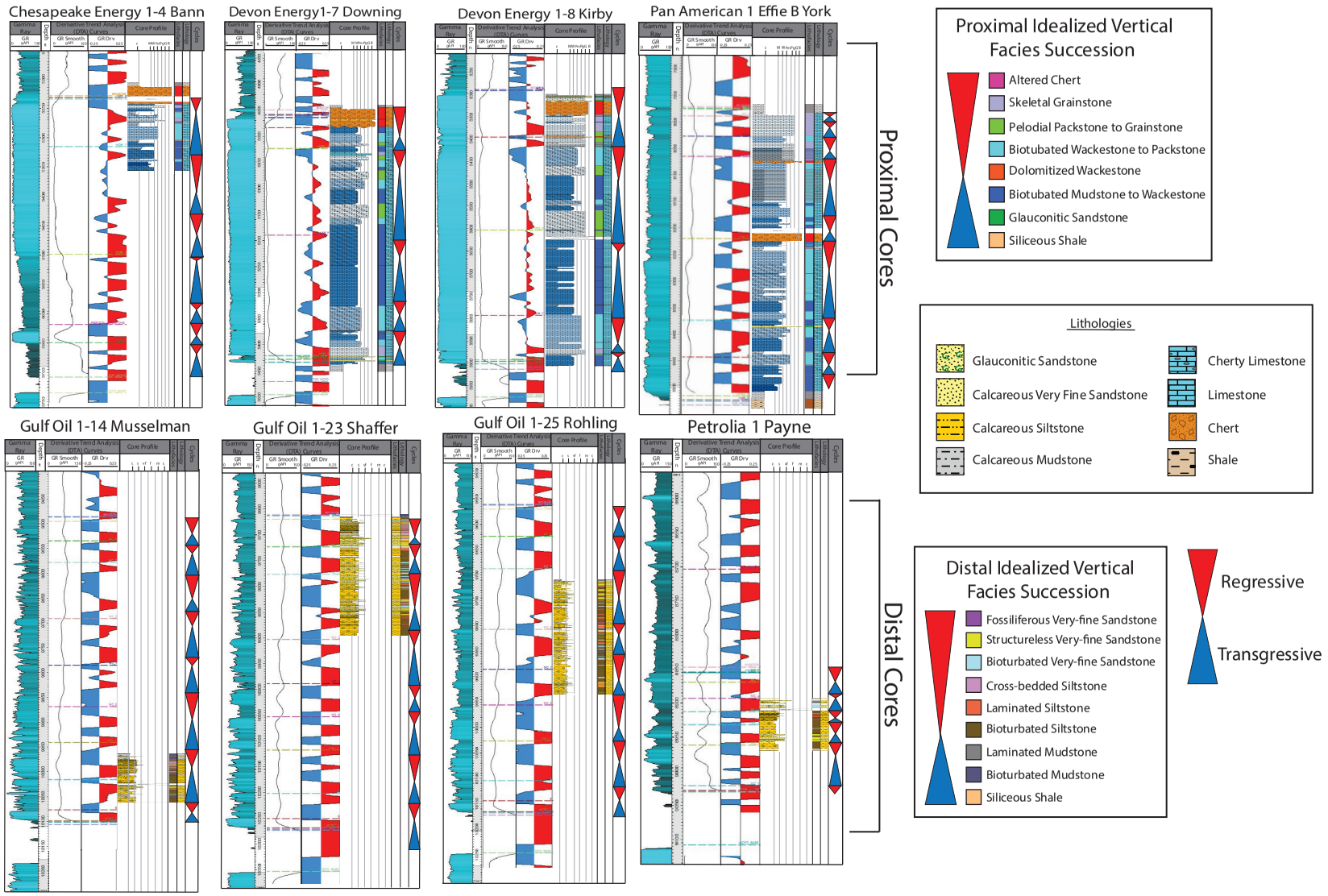
Chesapeake Energy 1-4 Bann
Devon Energy1-7 Downing
Devon Energy 1-8 Kirby
Pan American 1 Effie B York
Gulf Oil 1-14 Musselman
Gulf Oil 1-23 Shaffer
Gulf Oil 1-25 Rohling
Petrolia 1 Payne
Proximal Cores
Distal Cores
Proximal Idealized Vertical Facies Succession
Altered Chert
Skeletal Grainstone
Pelodial Packstone to Grainstone
Biotubated Wackestone to Packstone
Dolomitized Wackestone
Biotubated Mudstone to Wackestone
Glauconitic Sandstone
Siliceous Shale
Lithologies
Glauconitic Sandstone
Calcareous Very Fine Sandstone
Calcareous Siltstone
Calcareous Mudstone
Cherty Limestone
Limestone
Chert
Shale
Distal Idealized Vertical Facies Succession
Fossiliferous Very-fine Sandstone
Structureless Very-fine Sandstone
Bioturbated Very-fine Sandstone
Cross-bedded Siltstone
Laminated Siltstone
Bioturbated Siltstone
Laminated Mudstone
Bioturbated Mudstone
Siliceous Shale
Regressive
Transgressive

Figure 19: Proximal and distal cored wells that compare core description to gamma ray (GR) log responses, and the DTA curves which were used to interpret cycles. Four distal cored wells (Gulf Oil 1-14 Musselman, Gulf Oil 1-23 Shaffer, Gulf Oil 1-25 Rohling, and Petrolia 1 Payne) and 5 proximal cored wells (Chesapeake 1-4 Bann, Devon Energy 1-7 Frieouf, Devon Energy 1-7 Downing, Devon Energy 1-8 Kirby, and Pan American 1 Effie B York [Birch, 2015; Lindzey, 2015; Flinton, 2016; Suriamin and Pranter, 2018) are shown. The first track in each cored well is the GR log, the second is the Gaussian smoothed GR (smoothing windows vary based on location within the study area), and the third track is the GR derivative of the smoothed GR curve. For the DTA curve, red represents positive values (GR is decreasing or cleaning upward) and blue represents negative values (GR is increasing of fining upward). DTA allows for recognition of individual cycles and is useful in the absence of inadequate core coverage. The DTA curve approximates 3rd-order cyclicity in this case. The red triangles represent the regressive phases of cycles and the blue triangles represent the transgressive phases (Wethington and Pranter, 2018).

Lithology and Porosity Distribution

The stratigraphic framework was populated with electrofacies classification results and well-log data to create reservoir models The stratigraphic architecture and spatial distributions of lithology, total porosity (PHIT), and neutron-density porosity separation (PHISEP) are evaluated with dip-oriented (A-A') and oblique-oriented (B-B') reservoir models (Figure 20). Lithology and porosity vary significantly owing to variations in depositional environment and diagenetic processes.

Mississippian lithologies in the proximal area are stratigraphically characterized by an upward succession of deep water shales below storm weather wave base to shallow marine limestones within fair weather wave base. Specifically, a basal shale unit of the Kinderhookian is overlain by interbedded mudstones and dense limestones. This sequence is capped by prograding porous limestones, cherts, and cherty limestones associated with zones (ML 1-6 zones) (Figure 20 A and D). Down-dip, the Mississippian section in the STACK area is a siliciclastic-dominated system. Lithologies are characterized by a thinner basal Kinderhookian shale, overlain by calcareous very-fine sandstones, siltstones, and mudstone, fining and increasing in clay content upward (Osage 1-2 and Meramec 1-7). Spatial variations in lithology are also observed on a smaller scale within individual clinoformal packages, where generally thin (or locally absent) coarse grained proximal lithologies grade into thicker packages of sandstone and siltstones, which transition into thinner distal intervals of mudstones and shales. Similar proximal to distal trends are noted in the carbonate dominated up-dip "Mississippi-lime" area, where cyclic and aggradational inner ramp wackestones, packstones, and

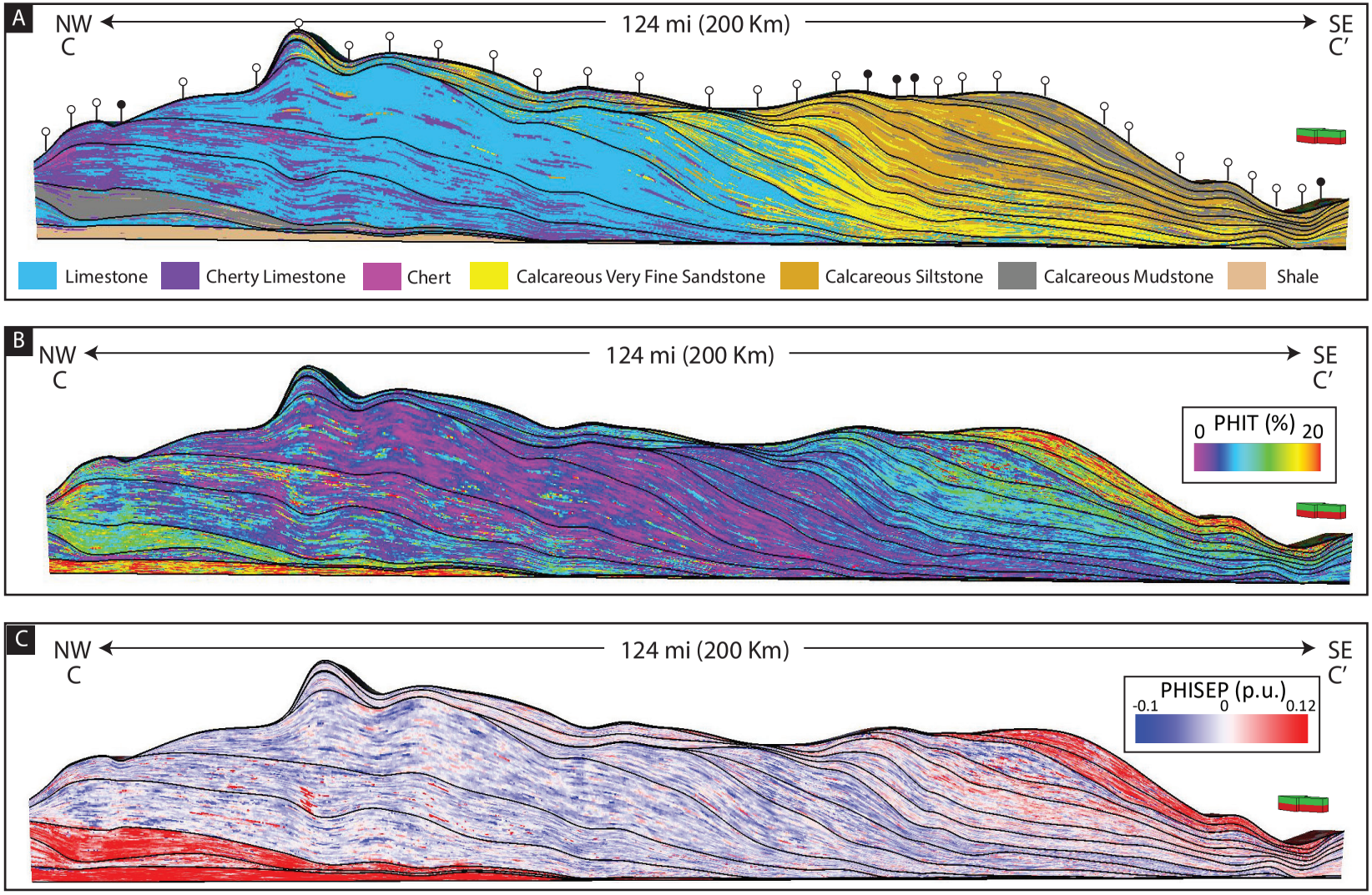
A
NW
C
124 mi (200 Km)
SE
C′
Limestone
Cherty Limestone
Chert
Calcareous Very Fine Sandstone
Calcareous Siltstone
Calcareous Mudstone
Shale
B
NW
C
124 mi (200 Km)
SE
C′
0 PHIT (%) 20
C
NW
C
124 mi (200 Km)
SE
C′
PHISEP (p.u.)
-0.1
0
0.12

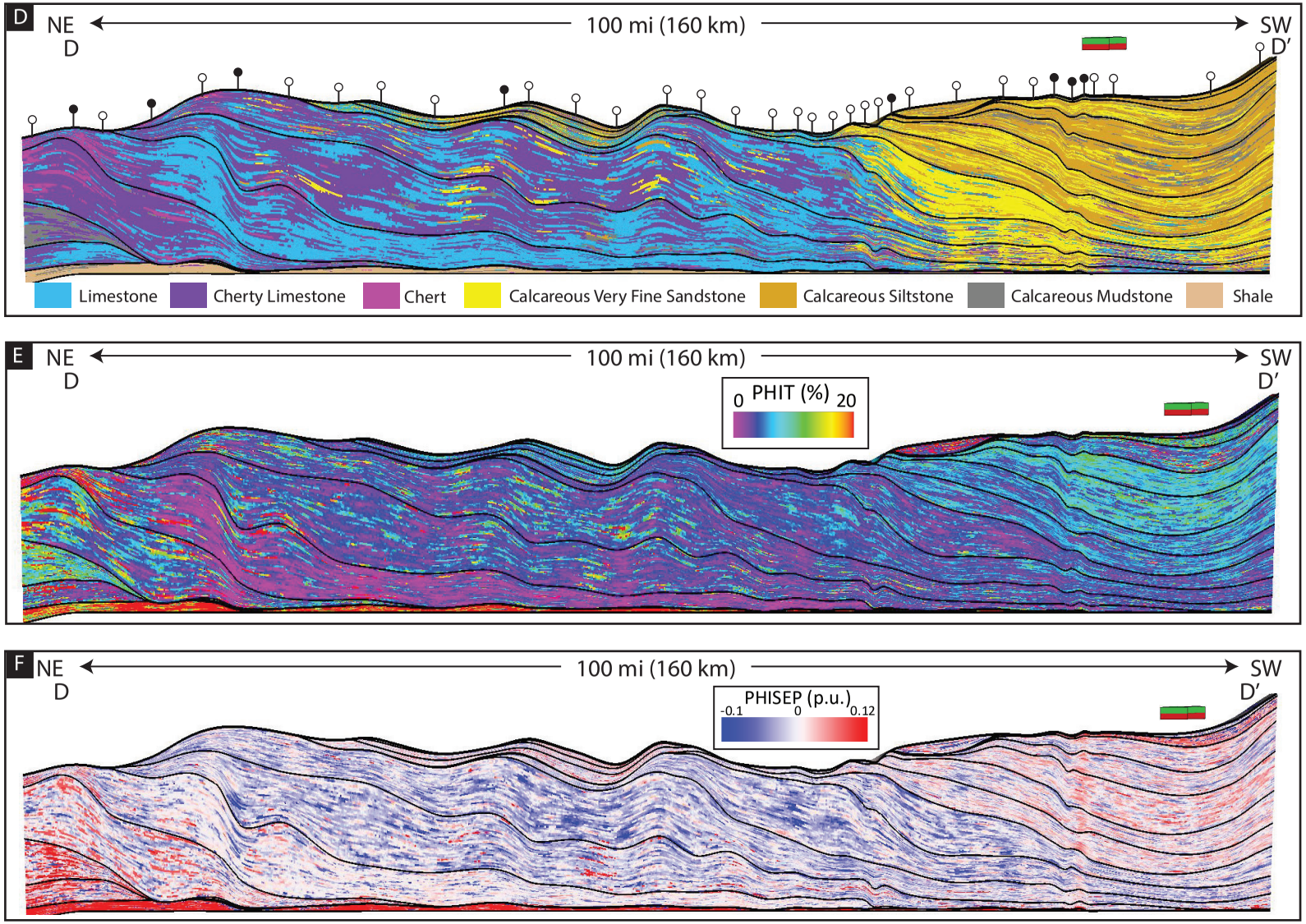
D
NE
D
100 mi (160 km)
SW
D′
Limestone
Cherty Limestone
Chert
Calcareous Very Fine Sandstone
Calcareous Siltstone
Calcareous Mudstone
Shale
E
NE
D
100 mi (160 km)
SW
D′
0 PHIT (%) 20
F
NE
D
100 mi (160 km)
SW
D′
PHISEP (p.u.)
-0.1
0
0.12

Figure 20: Dip-oriented (A, B, C) and oblique-oriented (D, E, F) lithology, total porosity, and porosity-separation models (flattened on top of Woodford Shale. (A) Lithology model showing the dip proximal to distal and stratigraphic variation in lithology. Cores used within the modeling for the dip model are represented by the black circles and non-cored wells are represented by the white circles. The Mississippian limestone zones are dominantly carbonate and silica-rich deposits. The Osage and Meramec lithologies represent some carbonate to siliciclastic deposits that are dominated by calcareous siltstones, mudstone and sandstones. (B) Total porosity (PHIT) model shows lower PHIT values are associated with carbonates. Higher PHIT values up-dip are associated with altered cherts and cherty limestone. Down-dip the higher PHIT values are related to the amount of clay in the system. C) Porosity separation (PHISEP) model emphasizes dolomitized and clay-rich intervals. High PHISEP values are associated with the higher PHIT intervals. High PHISEP values are concentrated in the Kinderhook zone and down-dip with the increased clay content. (D) Oblique-oriented lithology model showing stratigraphic variation in lithology. Cores used within the modeling for the oblique model are represented by the black circles and non-cored wells are represented by the white circles. (E) Oblique-oriented total porosity (PHIT) 3-D model. PHIT typically increases stratigraphy upward. In the oblique models, porosity trends are not as well observed as in the dip model. (F) Oblique-oriented porosity separation (PHISEP) 3-D model. The oblique-oriented models (D, E, and F) all show similar trends to the dip model. Models are vertically exaggerated 125 times the original size.

grainstones transition to outer ramp mudstones and wackestones. This distribution of lithologies aligns with the progradational nature observed within the interpreted stratigraphic framework (Figure 15; Figure 17). Overall, PHIT is higher up-dip and transitions into low PHIT values corresponding to the dense limestone in the center of the study area and then transitions into higher PHIT values associated with the shift in the system from carbonate-dominated to clastic-dominated.

Proximally, the highest total porosity (>20%) is associated with altered (tripolitic) chert (Figure 20). The high porosity zones are irregularly distributed but are typically concentrated in the northern portion of the study area at the top of the section (Figure 20B and E). The occurrence of chert at the top of the Mississippian likely coincident with the regional unconformity and exposure leading to diagenetically enhanced porosity (Rogers, 2001). The *in-situ* and weathered cherts are generally confined to proximal areas where regional dip provides a greater probability of impact from glacio-eustatic sea level changes. As Mississippian greenhouse conditions transitioned to Pennsylvanian icehouse conditions (Haq and Schutter, 2008), magnitude of sea level fluctuations decreased over time, likely resulting in a greater surface area subjected to subaerial exposure during the early Mississippian than the late Mississippian (Appendix A-3). This could support the increased abundance of diagenetically initiated porous chert in the early Mississippian Osagean strata than in the later-Mississippian-aged Meramec. In other words, there are more chert-rich sections in the proximal, older strata than in the distal, younger strata due to less drastic sea level change. Generally, lower porosity (1-2%) is observed with dense limestones associated with proximal prograding wedges (Figure 20). A trend of

decreasing porosity is observed from the top and crest of proximal sigmoidal clinoforms, where moderate porosity (~4-5%) along the clinoform slope transitions to the lowest porosity at the clinoform base (Figures 20B and E).

Distally, at the transition from Osage to Meramec strata, total porosity values generally increase owing to the transition from dominantly carbonate strata to more siliciclastic-rich interbedded sandstones, siltstones, and mudstones (Figure 20). With this transition comes an increase in detrital clay content, which inherently results in higher neutron-porosity values and subsequently greater neutron-density porosity separation values (Shale effect) and higher total porosity values increasing stratigraphically upward (Figure 20). X-ray diffraction analysis shows that the clay mineral assemblage of the distal siltstones and mudstones are dominated by illite and mica (2-18 wt. %) with trace amounts of kaolinite and chlorite. Greater porosity separation and higher clay content is commonly associated with less calcite cement (Figure 9E and G). The inverse relationship between clay content and calcite cement may be linked to obstruction of pore throats by fine-grained clay material inhibiting pervasive pore occluding cement (Figure 9E) (Price et al., 2017). However, there is a clay-content threshold beyond which reservoir quality is expected to decrease as fine-grained material fills pores and reduces rock brittleness (Brown, 1997; Jiang, 2012). Figure 10B illustrates the relationship of the volume of calcite to porosity, illustrating where there are higher amounts of calcite within the interval, the associated porosity is systematically decreased suggesting the calcite cement negatively affects the reservoir quality down-dip.

The transition from a carbonate-dominated system to a siliciclastic-dominated system is likely related to a number of factors. Throughout the Mississippian, there is a continual progressive sea level regression and with this sea level drop it is possible that during the middle Mississippian available accommodation for carbonate deposition effectively disappears favoring long-term regressive low stand clastic deposition, analogous to the well documented reciprocal sedimentation models that characterize higher-order sea level change (Van Siclen, 1958). Another potential contributing factor could be increased sedimentation rates driven by landward tectonic uplifts and ensuing sediment shedding, choking the carbonate system down-dip. Additionally, shifts in climate could play a contributing role. Shifts in wind direction could increase the potential for eolian sedimentation across the ramp, while increased precipitation can also be tied to higher runoff and sedimentation rates, suppressing carbonate development. Detrital carbonates and eolian silts have also been interpreted as transported by storms and turbidite flows downslope into the basin (Leavitt, 2018).

CONCLUSIONS

Mississippian carbonate and silica-rich reservoirs of northern and central Oklahoma formed on a regionally extensive carbonate ramp to basinal setting and vary significantly in terms of lithology and porosity from proximal to distal settings. Proximal lithofacies commonly include altered chert, skeletal grainstones, peloidal packstones-grainstones, bioturbated wackestones-packstones, bioturbated mudstones-wackestones, glauconitic sandstones, and siliceous shale. Dominant proximal pore types observed are vugs, molds, intercrystalline, and fracture. Periodic sea level fall and subsequent

subaerial exposure resulted in enhanced proximal porosities as meteoric fluids diagenetically replaced carbonate with silica creating chert-rich zones. Distal lithofacies include structureless to bioturbated calcareous sandstones, calcareous siltstones, and laminated calcareous mudstones. Dominant pore types observed in the distal lithologies are interparticle, intraparticle, and fracture. Calcite and clay volume, cementation, and compaction are the primary sources of variations in distal reservoir quality. The Mississippian limestone in the proximal setting represents a spectrum of carbonate ramp deposits; whereas, Osage and Meramec depositional cycles in the distal setting have been interpreted to represent subaqueous sedimentation, carbonate debris flows, clastic turbidite flows, and eolian silts. An Artificial-Neural Network (ANN) was used to accurately classify and predict core-defined lithologies with an overall accuracy of 85% for a depositional-dip transect and 83% for a oblique-oriented section.

Stratigraphic models were produced by correlating 16 stratigraphic zones within the Kinderhook, Mississippian limestone, Osage, and Meramec by means of a type of log attribute analysis called Derivative Trend Analysis (DTA) as well as distinctive correlative well-log signatures. The stratigraphic framework was populated with log data and electrofacies as predicted from a validated ANN to produce special lithology models. These stratigraphically constrained models reveal a succession of stratal geometries characterized by a basal shale-rich Kinderhookian interval overlain by prograding mudstones, limestones, and cherty limestones capped by cherts of the Mississippian limestone. These early Mississippian deposits are in turn overlain by younger siliciclastic

dominated clinoforms of the Osage and Meramec, comprised of calcareous siltstones, calcareous very-fine sandstones, and calcareous mudstones.

REFERENCES

Ahr, W., 1973, The Carbonate Ramp: An alternative to the shelf model: Gulf Coast Association of Geological Societies Transactions, v. 23, p. 221-225.

Allen, D. B., and M. J. Pranter, 2016, Geologically constrained electrofacies classification of fluvial deposits: an example from the Cretaceous Mesaverde group, Uinta and Piceance basins: AAPG Bulletin, v. 100, no. 12, p. 1775- 1801.

Anggraini, J., and M. A. Puspa, 2008, Supervised and unsupervised neural networks technique in facies classification and interpretation, *in* Indonesian Petroleum Association Thirty-Second Annual Convention and exhibition: p. 1-8.

Ball, M. M., M. E. Henry, and S. E. Frezon, 1991, Petroleum geology of the Anadarko Basin Region, Province (115), Kansas, Oklahoma, and Texas: Department of the Interior U.S. Geological Survey, 36 p.

Bentor, Y. K., and M. Kastner, 1965, Notes on the Mineralogy and Origin of Glauconite, Journal of Sedimentary Petrology, v. 35, no. 1, p. 155-166.

Birch, C. B., 2015, Reservoir-scale stratigraphy, sedimentology, and porosity characteristics of Mississippian reservoirs, northeastern Anadarko shelf, Oklahoma, master's thesis, University of Oklahoma, Norman, Oklahoma, 81 p.

Blakey, R., 2011, Paleogeography and geologic evolution of North America, http://cpgeosystems.com/paleomaps.html, (accessed December, 2015).

Boyd, D. T., 2008, Stratigraphic guide to Oklahoma oil and gas reservoirs: Oklahoma Geological Society, Special Publication 2008-1, 2 p.

Brown, A., 1997, Porosity variation in carbonates as a function of depth: Mississippian Madison Group, Williston Basin, Reservoir Quality Prediction in Sandstones and Carbonates, AAPG Memoir 69, p. 29-46.

Buggisch, W., M. M. Joachimski, G. Sevastopulo, and J. R. Morrow, 2008, Mississippian $\delta 13C_{carb}$ and Conodont Apatite $\delta 18O$ Records – Their Relation to the Late Palaeozoic Glaciation, Palaeogeography, Palaeoclimatology, Palaeoecology 268, p. 273-292.

Burst, J. F. 1958, "Glauconite" Pellets: Their Mineral Nature and Applications to Stratigraphic Interpretations, AAPG Bulletin, v. 42, no. 2, p. 310-327.

Caers, J., and T. Zhang, 2004, Multiple-point geostatistics: a quantitative vehicle for integrating geologic analogs into multiple reservoir models, AAPG Memoir 80, p. 383-394.

Campbell, J. A., C. J. Mankin, A. B. Schwarzkopf, and J. J. Raymer, 1988, Habitat of petroleum in Permian rocks of the midcontinent region; in, Permian Rocks of the Midcontinent, W. A. Morgan and J. A. Babcock, eds.: Midcontinent Society of Economic Paleontologists and Mineralogists, Special Publication, no. 1, p. 13-35.

Chaplin, J., 2010, Stratigraphic analysis of the Permian Chase Group in Northern Oklahoma -outcrop analogs of reservoir rocks in the Hugoton Embayment of Northwestern Oklahoma and Southwestern Kansas: Norman, OK, Oklahoma Geological Survey. 124 p.

Childress, M., and G. M. Grammer, 2015, High resolution sequence stratigraphic architecture of a mid-continent Mississippian outcrop in southwest Missouri: The Shale Shaker, v. 66, no. 4, p. 206-234.

Childress, M., and G. M. Grammer, 2018 , Characteristics of debris flows and outrunner blocks – evidence for Mississippian deposition on a distally steepened ramp, *in* G. M. Grammer, J. M. Gregg, J. O. Puckette, P. Jaiswal, S. J. Mazzullo, M. J. Pranter, and R. H. Goldstein, eds., Mississippian Reservoirs of the Midcontinent: AAPG Memoir 116, doi: 10.1306/13632145M1163786.

Choquette, P. W. and L. C. Pray, 1970, Geologic nomenclature and classification of porosity in sedimentary carbonates, AAPG Bulletin, v. 54, no. 2, p. 207-250.

Costello, D., M. Dubois, and R. Dayton, 2014, Core to Characterization and Modeling of the Mississippian, North Alva Area: 2014 Mid-continent Section AAPG Core Workshop, p. 165-174.

Coveney, R. M., 1992, Evidence for expulsion of hydrothermal fluids and hydrocarbons in the Midcontinent during the Pennsylvanian, *in* Johnson, K. S., and Cardott, B. J., Source rocks in the southern Midcontinent, 1990, Symposium, Oklahoma Geological Survey, Circular, v. 93, p. 133-143.

Curtis, D. M., and S. C. Champlin, 1959, Depositional Environments of Mississippian Limestones of Oklahoma, Tulsa Geological Society Digest, v. 27, no. 1, p. 90-103.

Deffeyes, K. S., 1965, Carbonate equilibria: a graphic and algebraic approach, Limnology and Oceanography, v. 10, p. 412–426.

Doveton, J. H., 1986, Log analysis of subsurface geology- concepts and computer methods: Wiley Interscience, New York, 273 p.

Dubois, M. K., G. C. Bohling, and S. Chakrabarti, 2007, Comparison of four approaches to a rock facies classification problem, Computers and Geoscience, v. 33, p. 599-617.

Dutton, S. P., 1985, Fan-delta Granite Wash of the Texas Panhandle: Oklahoma City Geological Society Short Course, p. 1-144.

Elebiju, O. O., S. Matson, G. R. Keller, and K. J. Marfurt, 2011, Integrated geophysical studies of the basement structures, the Mississippian chert, and the Arbuckle Group of Osage County region, Oklahoma: AAPG Bulletin, v. 95, p. 371- 393.

Evans, J. L., 1979, Major structural features of the Anadarko Basin: Tulsa Geological Society, Special Publication no. 1, p. 97-114.

Farzaneh, S., 2012, Integrated paleomagnetic and diagenetic study of the Mississippian limestones in northern Oklahoma, master's thesis, The University of Oklahoma, Norman, Oklahoma, 98 p.

Flinton, K. C., 2016, The effects of high-frequency cyclicity on reservoir characteristics of the "Mississippian Limestone", Anadarko Basin, Kingfisher County, Oklahoma, master's thesis, Oklahoma State University, Stillwater, Oklahoma, 414 p.

Gao, Z., and Y. Wang, 2017, Sequence stratigraphic architecture and reservoir characteristics of the unconventional "Mississippian Limestone", North-Central Oklahoma, USA: Unconventional Resources Technology Conference (URTEC), Article #2670748.

Grammer, G. M., D. Boardman, J. Puckette, J. Gregg, J. Priyank, M. Childress, B. J. Price, B. Vanden Berg, and S. LeBlanc, 2013, Integrated reservoir characterization of Mississippian-age mid-continent carbonates: AAPG Search and Discovery Article #30297, 31 p.

Grotsch, J., and C. Mercadier, 1999, Integrated 3-D reservoir modeling based on 3-D seismic: the Tertiary Malampaya and Camago buildups, offshore Palawan, Philippines: AAPG Bulletin, v. 83, p. 1703–1728.

Guo, H., 2011, A Simple algorithm for fitting a Gaussian function (DSP Tips and Tricks): Signal Processing Magazine, IEEE, v. 28, no. 5, p. 134-137.

Gutschick, R., and C. A. Sandberg, 1983, Mississippian continental margins of the conterminous United States: SEPM Special Publication, no. 33, p. 79-96.

Ham, W. E., and J. L. Wilson, 1967, Paleozoic epeirogeny and orogeny in the central United States: American Journal of Science, v. 265, p. 332-407.

Haq, B. U., and S. R. Schutter, 2008, A chronology of Paleozoic sea-level changes: Science, v. 322, p. 64-68.

Hartigan, J. A., 1975, Clustering algorithms: New York, John Wiley & Sons, p. 84- 107.

Haynes, J., 2013, Diagenesis within the Mississippian limestone–north central Oklahoma, master's thesis, The University of Oklahoma, Norman, Oklahoma, 80 p.

Jaeckel, L., 2016, High-resolution sequence stratigraphy and reservoir characterization of mid-continent Mississippian carbonates in north-central Oklahoma and south-central Kansas, master's thesis, Oklahoma State University, Stillwater, Oklahoma, 356 p.

Janssen, L. F., and F. M. van der Wel, 1994, Accuracy assessment of satellite derived land- cover data: a review: Photogrammetric Engineering and Remote Sensing, v. 60, p. 419 – 426.

Jiang, S., 2012, Clay minerals from the perspective of oil and gas exploration, Clay Minerals in Nature, p. 21-38.

Johnson, K. S., and K. V. Luza, 2008, Earth sciences and mineral resources of Oklahoma: Oklahoma Geological Survey, Educational Publication 9, 22 p.

Kanungo, T., D. Mount, N. Netanyahu, C. Piatko, R. Silverman, and A. Wu, 2002, An efficient K-means clustering algorithm, Analysis and implementation, Pattern Analysis and Machine Intelligence: IEEE Transactions on Pattern Analysis and Machine Intelligence, v. 24, no. 7, p. 881-892.

Kapur, L., L. Lake, D. Sepehrnoori, D. Herrick, and C. Kalkomey, 1998, Facies prediction from core and log data using artificial neural network technology. In: Transactions of the 39th Society of Professional Well Log Analysts Annual Logging Symposium, Keystone, CO, paper PP, p. 11.

Knauth, L. P., 1979, A model for the origin of chert in limestone, Geology, v. *7*, p. 274-277.

Kumar, B., and M. Kishore, 2006, Electrofacies classification – a critical approach: 6th International conference and exposition on petroleum geophysics, Kolkata, India, p. 822-825.

Leavitt, A., 2018, Depositional systems of the STACK and SCOOP Mississippian units; regional understanding from logs and core, STACK Play Workshop Technical Program and Core Viewing, Norman, Oklahoma.

LeBlanc, S. L., 2014, High resolution sequence stratigraphy and reservoir characterization of the "Mississippian Limestone" in north-central Oklahoma, master's thesis, Oklahoma State University, Stillwater, Oklahoma, 455 p.

Lindzey, K., 2015, Geologically constrained seismic characterization and 3-D reservoir modeling of Mississippian reservoirs, north-central Anadarko shelf, Oklahoma, master's thesis, University of Oklahoma, Norman, Oklahoma, 97 p.

LoCricchio, E., 2012, Granite Wash play overview, Anadarko Basin: Stratigraphic framework and controls on Pennsylvanian Granite Wash production, Anadarko Basin, Texas and Oklahoma, AAPG Annual Convention and Exhibition: Long Beach, California, p. 1-17.

Mazzullo, S. J., 2004, Overview of porosity evolution in carbonate reservoirs, Kansas Geological Survey Bulletin, v. 79, n. 1.

Mazzullo, S. J., 2011, Mississippian oil reservoirs in the southern Midcontinent: new exploration concepts for a mature reservoir objective: Search and DiscoveryArticle #10373.

Mazzullo, S., H. Cao, and B. W. Wilhite, 2008, Chert reservoirs in the Cowley formation (Mississippian) south-central Kansas: paragenesis, oxygen and silicon isotope geochemistry, and timing of silicification and porosity formation: Kansas Geological Society Bulletin, v. 93, no. 12, p. 1649-1689.

Mazzullo, S., B. W. Wilhite, and I. W. Woolsey, 2009, Petroleum reservoirs within a spiculite dominated depositional sequence: Cowley Formation (Mississippian: Lower Carboniferous), south-central Kansas: AAPG Bulletin, v. 93, no. 12, p. 164-1689.

Mazzullo, S. J., D. R. Boardman, B. W. Wilhite, C. Godwin, and B. T. Morris, 2013, Revisions of Outcrop Lithostratigraphic Nomenclature in the Lower to Middle Mississippian Subsystem (Kinderhookian to Basal Meramecian Series) Along the Shelf-Edge in Southwest Missouri, Northwest Arkansas, and Northeast Oklahoma, Oklahoma City Geological Society, The Shale Shaker Digest, v. 63, no. 6, p. 414-454.

Mazzullo, S. J., B. W. Wilhite, D. R. Boardman, B. T. Morris, and C. J. Godwin, 2016, Stratigraphic architecture and petroleum reservoirs in lower to middle Mississippian strata (Kinderhookian to basal Meramecian in subsurface, central to southern Kansas and northern Oklahoma: Shale Shaker, v. 67, p. 20-49.

McConnell, D. A., M. J. Goydas, G. N. Smith, and J. P. Chitwood, 1989, Morphology of the frontal fault zone, southwest Oklahoma: Implications for deformation and deposition in the Wichita uplift and Anadarko basin: Geology, v. 18, no. 7, p. 34-637.

Middleton, G. V., M. J. Church, M. Coniglio, L. A. Hardie, and F. J. Longstaffe, 2003, Encyclopedia of Sediments and Sedimentary Rocks, The Netherlands, Kluwer Academic Publishers, 821 p.

Miller, J. C., 2018, Regional stratigraphy and organic richness of the Mississippian Meramec and associated strata, Anadarko Basin, Central Oklahoma, master's thesis, University of Oklahoma, Norman, Oklahoma, 154 p.

Montgomery, S. L., J. C. Mullarkey, M. W. Longman, W. M. Colleary, and J. P. Rogers, 1998, Mississippian chat reservoirs, south Kansas: Low-resistivity pay in a complex chert reservoir, AAPG Bulletin, v. 82, p. 187-205.

Northcutt, R. A. and J. A. Campbell, 1995, Geologic provinces of Oklahoma: Oklahoma Geological Survey, Open-File Report 5-95, 6 p.

Northcutt, R. A., K. S. Johnson, and G. C. Hinshaw, 2001, Geology and petroleum reservoirs in Silurian, Devonian and Mississippian rock in Oklahoma: Oklahoma Geological Survey Circular, p. 1-15.

Perry, W. J., 1989, Tectonic evolution of the Anadarko Basin region, Oklahoma: Department of Interior, U.S. Geological Survey, no. 1866-A, p. A1-A19.

Pranter, M. J., A. Turnini, K. Marfurt, and D. Devegowda, 2016, Multidisciplinary characterization and modeling of Mississippian carbonate and silica-rich reservoirs, northern Oklahoma, AAPG Mid-Continent Section in Tulsa, Oklahoma, October 4-6, 2015, Search and Discovery Article #51231.

Price, B. J., 2014, High resolution sequence stratigraphic architecture and reservoir characterization of the Mississippian Burlington/Keokuk Formation, northwestern Arkansas, master's thesis, Oklahoma State University, Stillwater, OK, 154 p.

Price, B. J., and G. M. Grammer, 2018, High resolution sequence stratigraphic architecture and reservoir characterization of the Mississippian Burlington/Keokuk

Formation, northwestern Arkansas, *in* G. M. Grammer, J. M. Gregg, J. O. Puckette, P. Jaiswal, S. J. Mazzullo, M. J. Pranter, and R. H. Goldstein, eds., Mississippian Reservoirs of the Midcontinent: AAPG Memoir 116, doi: 10.1306/13632147m1163787.

Price, B., K. Haustveit, and A. Lamb, 2017, Influence of stratigraphy on barriers to fracture growth and completion optimization in the Meramec Stack Play, Anadarko Basin, Oklahoma: Unconventional Resources Technology Conference (URTEC), Article #2697585, 8 p.

Qi, L., T. R. Carr, and R. H. Goldstein, 2007, Geostatistical three-dimensional modeling of oolite shoals, St. Louis Limestone, southwest Kansas, AAPG Bulletin, v. 91, p. 69-96.

Ramaker, E. M., R. H. Goldstein, E. K. Franseen, and L. W. Watney, 2014, What controls porosity in cherty fine-grained carbonate reservoir rocks? Impact of stratigraphy, unconformities, structural setting and hydrothermal fluid flow: Mississippian, SE Kansas: *in* S. Agar and S. Geiger, eds., Fundamental Controls on Fluid Flow in Carbonates: Current Workflows to Emerging Technologies, Geological Society London, Special publication, v. 406, p. 179-208.

Read, J., 1985, Carbonate Platform Facies Models: AAPG Bulletin, v. 69, no. 1, p. 1-21.

Read, J. F., 1995, Overview of Carbonate Platform Sequences, Cycle Stratigraphy and Reservoirs in Greenhouse and Icehouse Worlds, In: Read, J. F., Kerans, C., Weber, L. J., Sarg, J. F., and Wright, F. M. (eds.), Milankovitch Sea Level Changes, Cycles, and Reservoirs on Carbonate Platforms in Greenhouse and Ice-House Worlds: SEPM Short Course 35, p. 1-102.

Rider, M., and D. Laurier, 1979, Sedimentology using a computer treatment of well logs, Trans. Soc. of Well Log Analysts, 6th European Symposium, London, Paper J.

Rogers, S. M., 2001, Deposition and diagenesis of Mississippian chat reservoirs, north-central Oklahoma: AAPG Bulletin, v. 85, p. 115-130.

Russell, S. D., M. Abkar, B. Vissapragada, and G. M. Walkden, 2002. Rock types and permeability prediction from dipmeter and image logs: Shuaiba reservoir (Aptian), Abu Dhabi: AAPG Bulletin v. 86, p. 1709–1732.

Saggaf, M. M., and E. L. Nebrija, 2000, Estimation of lithologies and depositional facies from wireline logs: AAPG Bulletin v. 84, p. 1633–1646.

Scholle, P. A., and D. S. Ulmer-Scholle, 2003, A color guide to the petrography of carbonate rocks: grains, textures, porosity, diagenesis, AAPG Memoir 77, Tulsa, The American Association of Petroleum Geologists, 474 p.

Serra, O., and H. T. Abbott, 1980, The contribution of logging data to sedimentary sedimentology and stratigraphy, SPE-9270: Society of Petroleum Engineers, presented at 55th Annual Technical Conference and Exhibition [Dallas], preprint, 19 p. Later published in 1982, Society of Petroleum Engineers Journal, v. 22, no. 1, p. 117-131.

Shapiro, L. G., and G. C. Stockman, 2000, Computer vision: Upper Saddle River, NJ, Prentice Hall, p. 170.

Shelley, S., G. M. Grammer, and M. J. Pranter, 2017, Reservoir characterization and modeling of a subsurface Meramec analog from a quarry in northeastern Oklahoma: The Shale Shaker, v. 68, no. 5, p. 224-243.

Shelley, S., G. M. Grammer, and M. J. Pranter, 2018, Outcrop-based reservoir characterization and modeling of an Upper Mississippian mixed carbonate-siliciclastic ramp, Northeastern Oklahoma, *in* Grammer, G.M., J. Gregg, J. Puckette, P. Jaiswal, M. Pranter, S. Mazzullo, and R. Goldstein, editors, Mississippian Reservoirs of the Mid-Continent, U.S.A., American Association of Petroleum Geologists Memoir 116, doi: 10.1306/136321482158M1163788

Sloss, L. L., 1963, Sequences in the cratonic interior of North America: Geological Society of America Bulletin 74, p. 93-114.

Sullivan, K. B., J. S. Campbell, and K. E. Dahlberg, 2003, Petrofacies: enhancing the deepwater reservoir characterization effort in West Africa, Petrophysics, v. 44, no. 3, p. 177-189.

Suriamin, F., and M. J. Pranter, 2018, Stratigraphic and lithofacies control on pore characteristics of Mississippian limestone and chert reservoirs of north-central Oklahoma, Interpretation, v. 6, no. 6, p. 1-22.

Ting, K. M., 2011, Confusion matrix, in C. Sammut and G.I. Webb, eds., Encyclopedia of machine learning, 1st ed.: New York, Springer, 209 p.

Vanden Berg, B., and G. M. Grammer, 2016, Qualitative and Quantitative Characterization of Carbonate Mudrock Pore Architecture: An example from the Mid-Continent "Mississippian" Limestone, *in* T. Olson (ed), AAPG Memoir 112, Imaging Unconventional Reservoir Pore Systems. p. 185-232, doi: 10.1306/13592022M1123698

Vanden Berg, B., B. S. LeBlanc, and G. M. Grammer, 2017, Integrated reservoir characterization to provide insight into porosity and permeability in a mixed carbonate-siliciclastic reservoir, *in* Grammer, G.M., J. Gregg, J. Puckette, P. Jaiswal, M. Pranter, S. Mazzullo, and R. Goldstein, editors, Mississippian Reservoirs of the Mid-Continent, U.S.A., American Association of Petroleum Geologists Memoir 116, doi: 10.1306/13632150M1163698

Van Siclen, D. C., 1958, Depositional topography-examples and theory: AAPG Bulletin, v 42, p. 1897-1913.

Wang, Y., T. Thompson, and G. M. Grammer, 2017, Fracture Characterization and Prediction in Unconventional Reservoirs of the "Mississippian Limestone", North-Central Oklahoma, USA, *in* Grammer, G.M., J. Gregg, J. Puckette, P. Jaiswal, M. Pranter, S. Mazzullo, and R. Goldstein, editors, Mississippian Reservoirs of the Mid-Continent, U.S.A., American Association of Petroleum Geologists Memoir 116, doi: 10.1306/13632151M1163789

Watney, W. L., W. J. Guy, and A. P. Bynes, 2001, Characterization of the Mississippian chat in south-central Kansas: AAPG Bulletin, v. 85, p. 85-113.

Wethington, N. W., and M. J. Pranter, 2018, Stratigraphic Architecture of the Mississippian Limestone through integrated electrofacies classification, Hardtner Field area, Kansas and Oklahoma, Interpretation, v. 6, no. 4, 22 p.

Wilhite, B. W., and S. J. Mazzullo, 2013, Regional aspects of stratal architecture of the subsurface Mississippian in Kansas based on wireline log cross-sections and seismic: AAPG Search and Discovery Article #30307.

Witzke, B. J., 1990, Paleoclimatic constraints for Paleozoic paleolatitudes of Laurentia and Euramerica, W. S. McKerrow and C. R. Scotese, eds. Paleogeography and biogeography: Geological Society (London) Memoir 12, p. 57-73.

Wolff, M., and J. Pelissier-Combescure, 1982, FACIOLOG- Automatic electrofacies determination, paper FF, in 23rd Annual Logging Symposium Transactions: Society of Professional Well Log Analysts, p. 22.

Young, E. M., 2010, Controls on reservoir character in carbonate-chert strata, Mississippian (Osagean-Meramecian), southeast Kansas, master's thesis, The University of Nebraska, Omaha, Nebraska 198 p.

Appendix A: Geologic Setting

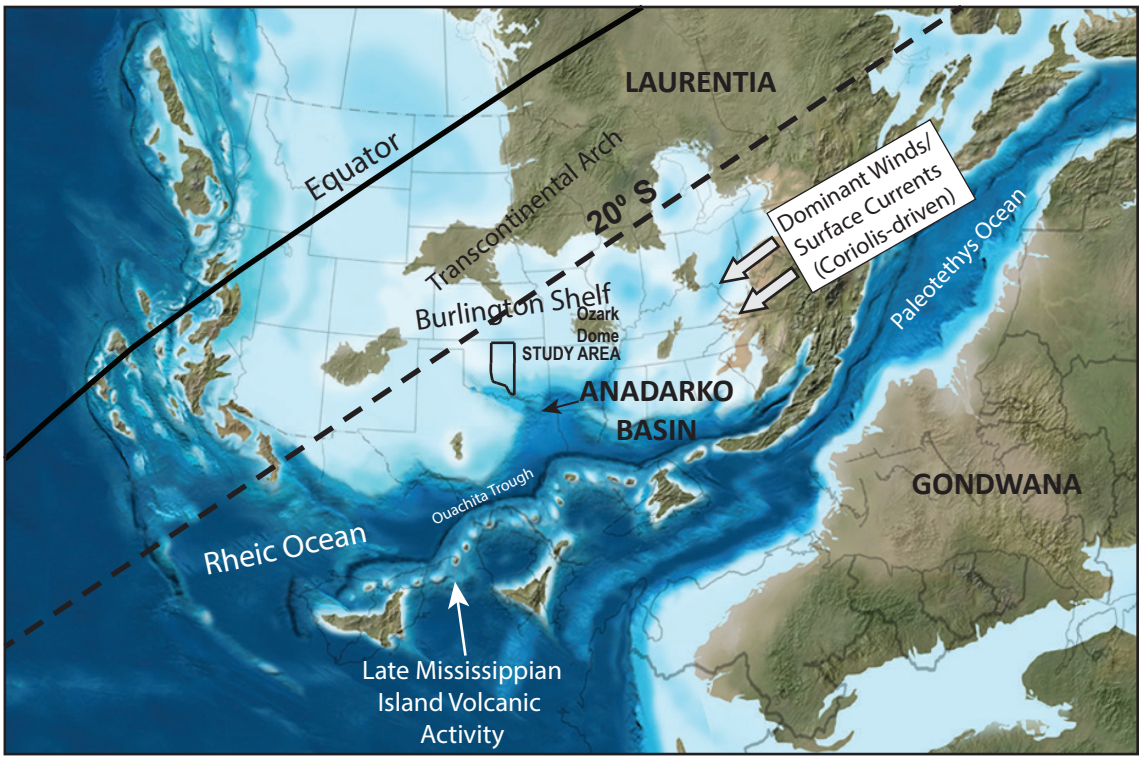

Appendix A-1. Paleogeographic map of the Early Mississippian. The study area is located on the Anadarko shelf and in the basin, which is positioned between 20-30º S. Deposition occurred 25-30º south of the paleoequator. A warm shallow sea was present with a starved basin to the south. Blue represents the water depth during this time, light blue indicating shallow waters and dark blue indicating deep waters (modified from Blakey, 2011; Gutschick and Sandberg, 1983).

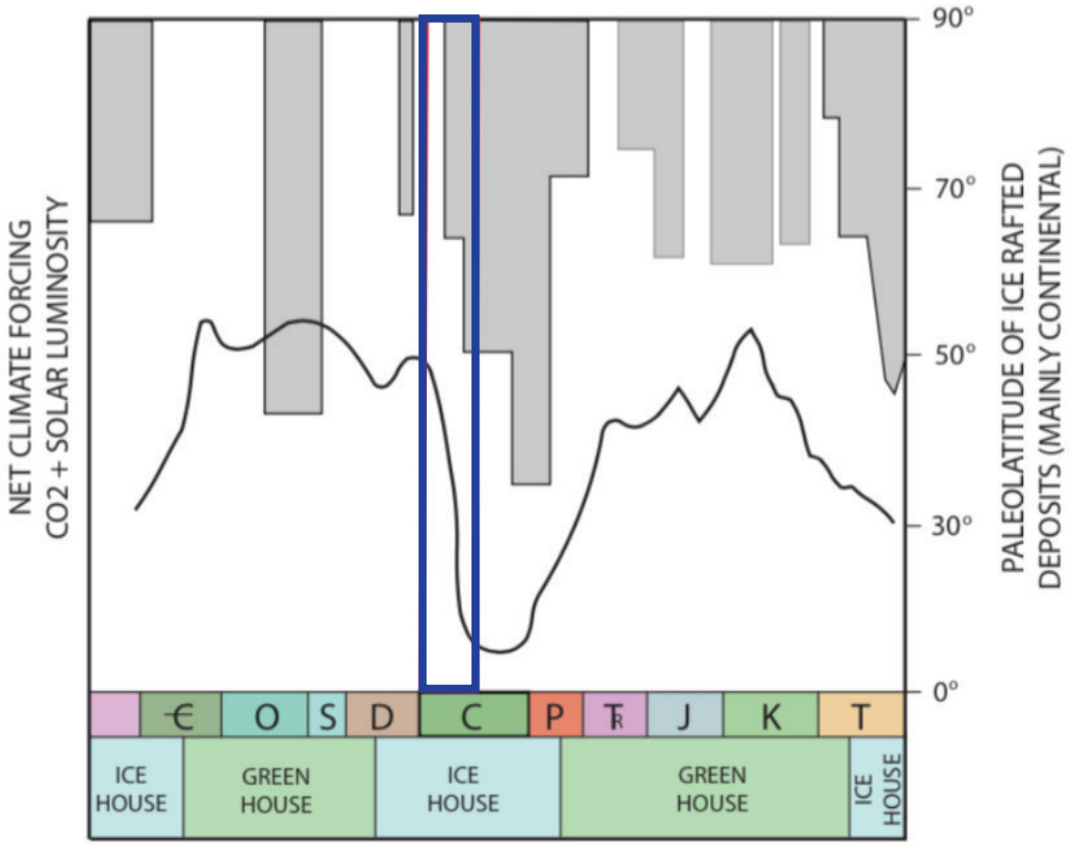

Figure A-2: Distribution of icehouse an greenhouse conditions. Gray boxes with black outline illustrate paleolatitudes of ice rafted glacial deposits data. Gray boxes with black outline illustrate marine ice in CO_2 and solar intensity data, which represents that the Mississippian time was a transitional period from greenhouse conditions (existing during the Devonian) to icehouse conditions in the Pennsylvanian. Blue box highlights the Mississippian (modified from Read 1995).

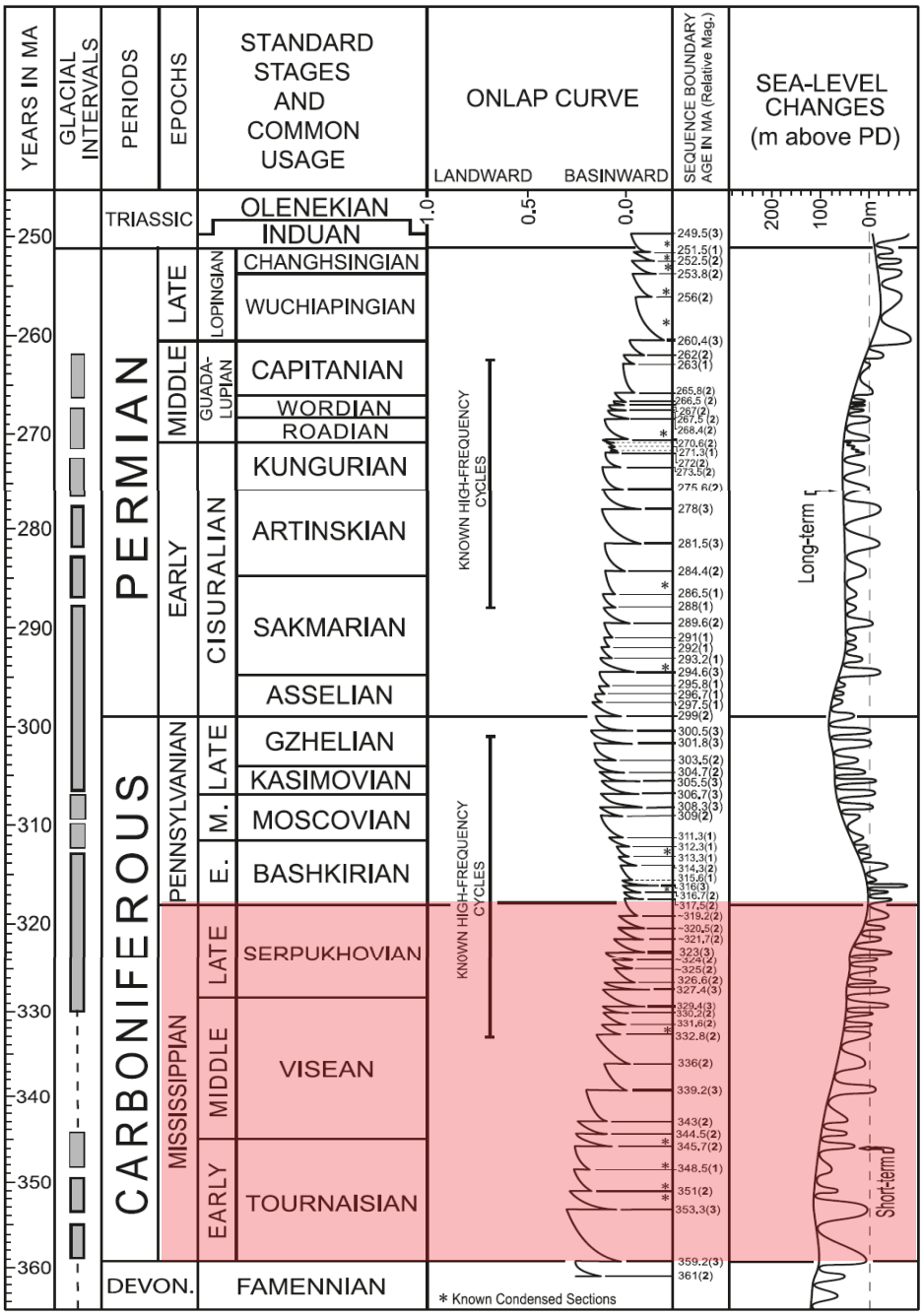

Appendix A-3. Global sea level and onlap curve for Carboniferous-Permian Period with Mississippian Epoch highlighted in orange. The interval of interest was deposited during a global second-order sea level fall with higher order cyclicity within, Increased cycle frequency and relative decrease in cycle duration in the late Meramecian and Chesterian likely reflects the transition from greenhouse in the Early Mississippian to icehouse in the Pennsylvanian (modified from Haq and Schutter, 2008).

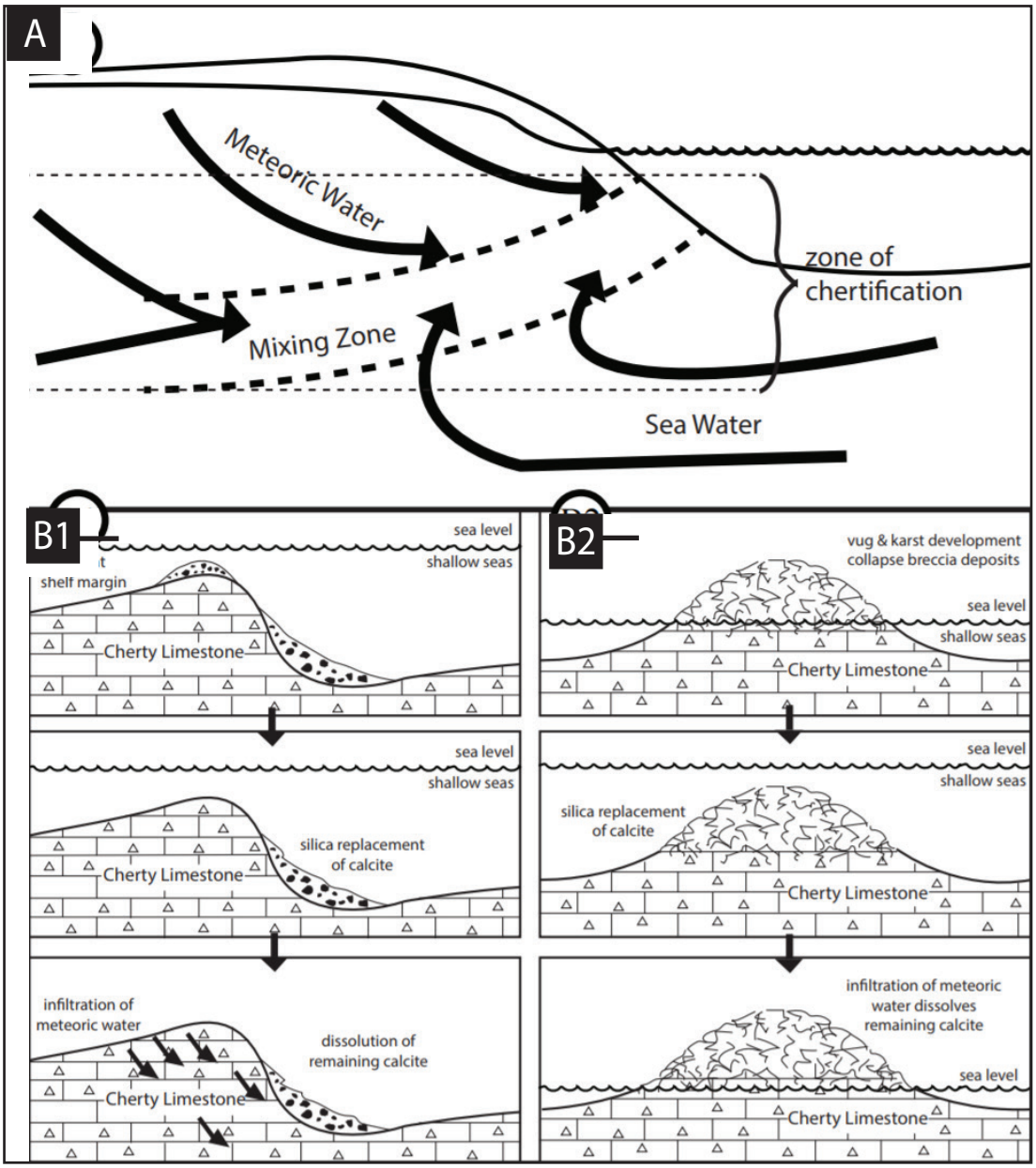

Appendix A-4: (A) Proposed method for chert replacement of carbonate (modified from Knauth, 1979). Pore waters were supersaturated with calcite and oversaturated with silica in the zone of mixing between meteoric and sea water, leading to dissolution of carbonates and replacement with chert. (B) Pathways forming porous chert reservoirs (modified from Rogers, 2001). (B1) Transported tripolite from a reef washed downslope from the shelf margin and silica replacement of calcite occurred within the mixing zone illustrated in (A) and a final fall in sea level led to creation of increased porosity. (B2) In-situ formation of tripolite from initial fall in sea level developing porosity and karst features, a rise in sea level allowed for replacement of calcite with silica in the mixing zone shown in (A) and a final fall in sea level led to further porosity creation.

Appendix B: Core Descriptions

Appendix B-1: Gulf Oil1-23 Shaffer

Well Name: Shaffer 1-23	
Operator: Gulf Oil Corporation	**UWI No.:** 35011215220000
Basin: Anadarko	**Latitude:** 35.8428394
Country: United States	**Longitude:** -98.2355156
State: Oklahoma	**KB:** 1,250 ft
County: Blaine	**Well TD:** 10,784 ft
Field: Omega West	**Top of Core Description:** 9,645 ft
Date: 8/30/1980	**Bottom of Core Description:** 9,557 ft

Lithologies

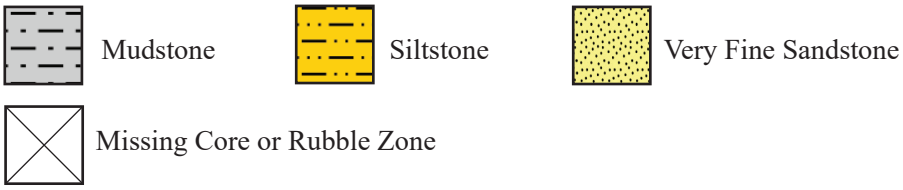

Lithofacies

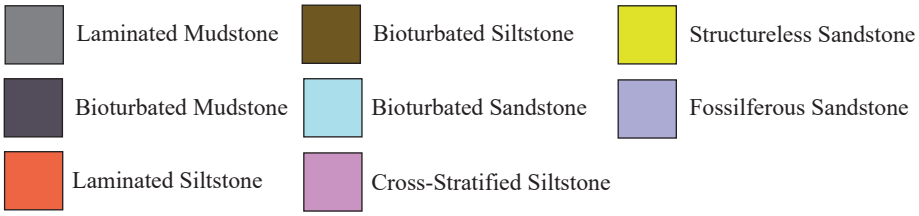

Admixture

Structure

Fossils

Trace Fossils

Sedimentary Structures

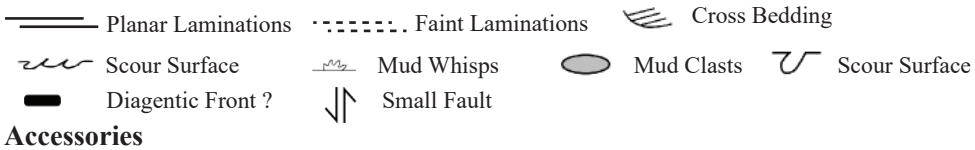

Accessories

Contacts

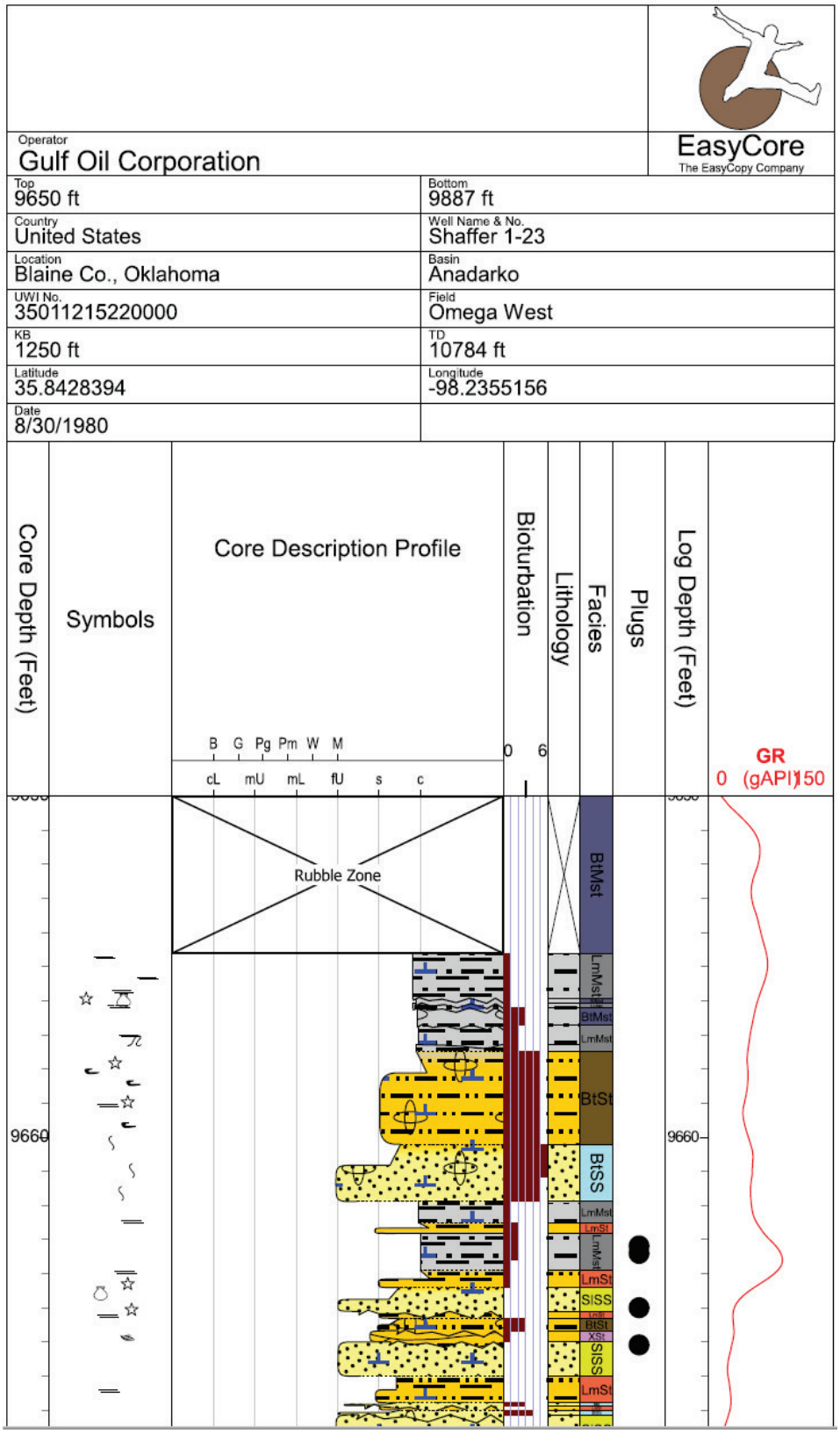
EasyCore
The EasyCopy Company
Operator
Gulf Oil Corporation
Top
9650 ft
Bottom
9887 ft
Country
United States
Well Name & No.
Shaffer 1-23
Location
Blaine Co., Oklahoma
Basin
Anadarko
UWI No.
35011215220000
Field
Omega West
KB
1250 ft
TD
10784 ft
Latitude
35.8428394
Longitude
-98.2355156
Date
8/30/1980
Core Depth (Feet)
Symbols
Core Description Profile
B G Pg Pm W M
cL mU mL fU s c
Bioturbation
0 6
Lithology
Facies
Plugs
Log Depth (Feet)
GR
0 (gAPI) 150
Rubble Zone
BtMst
BtSt
BtSS
LmSt
SlSS
XSt
9660
9660

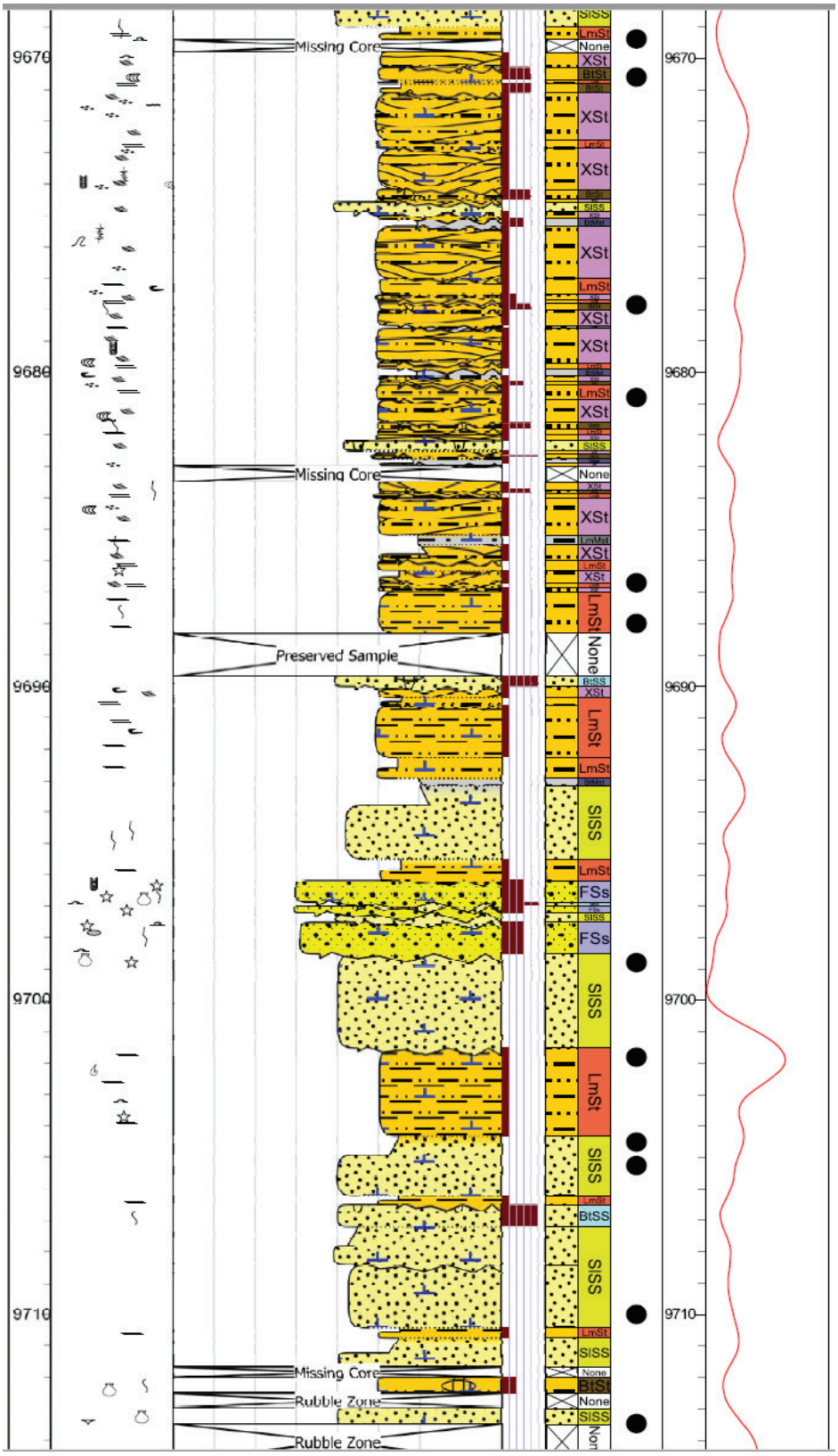
9670
9680
9690
9700
9710
Missing Core
Missing Core
Preserved Sample
Missing Core
Rubble Zone
Rubble Zone
XSt
LmSt
SiSS
FSs
BtSS
None
BtSt

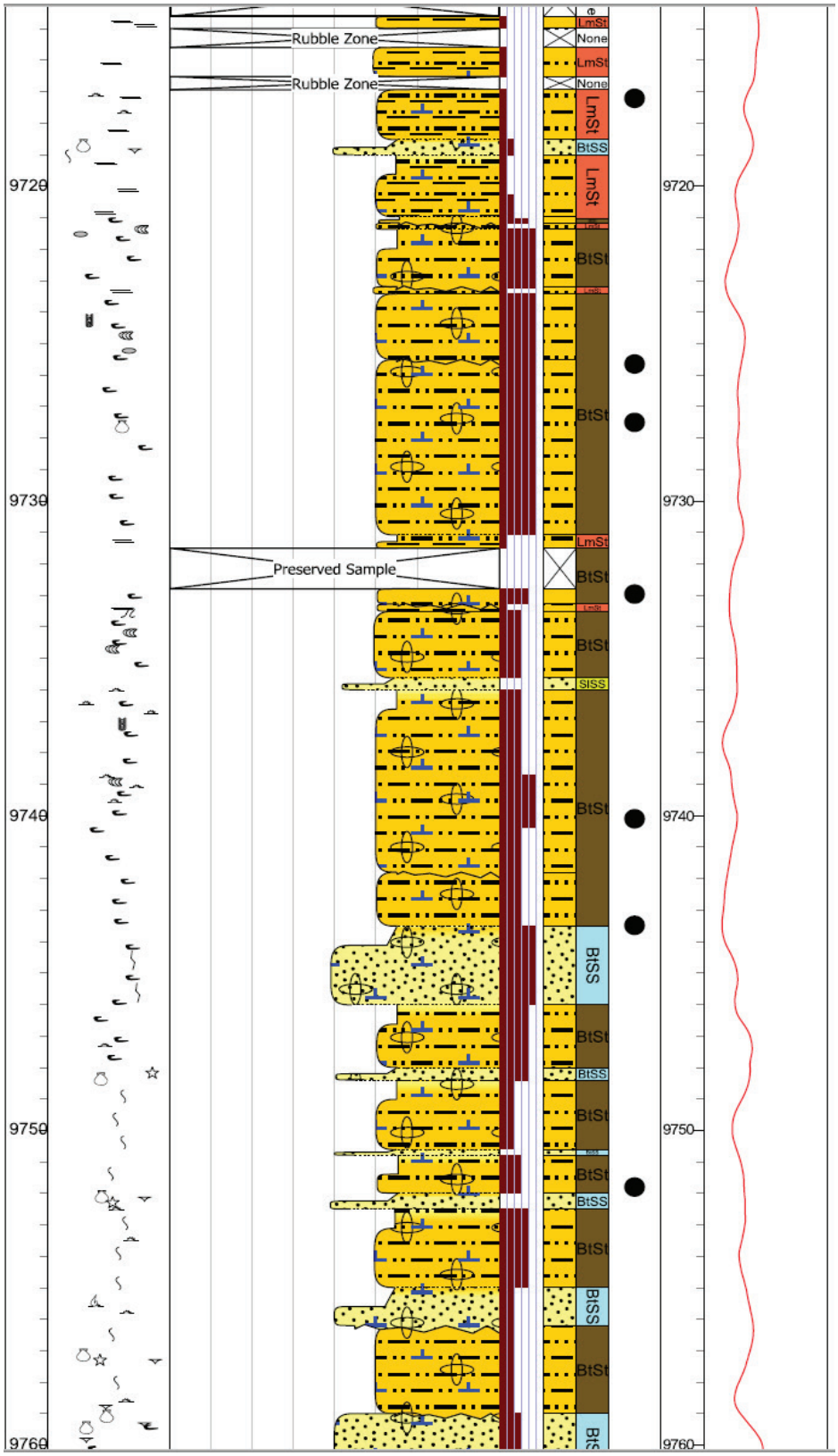
Rubble Zone
Rubble Zone
Preserved Sample
LmSt
None
LmSt
None
LmSt
BtSS
LmSt
BtSS
BtSS
BtSS
BtSS
9720
9730
9740
9750
9760

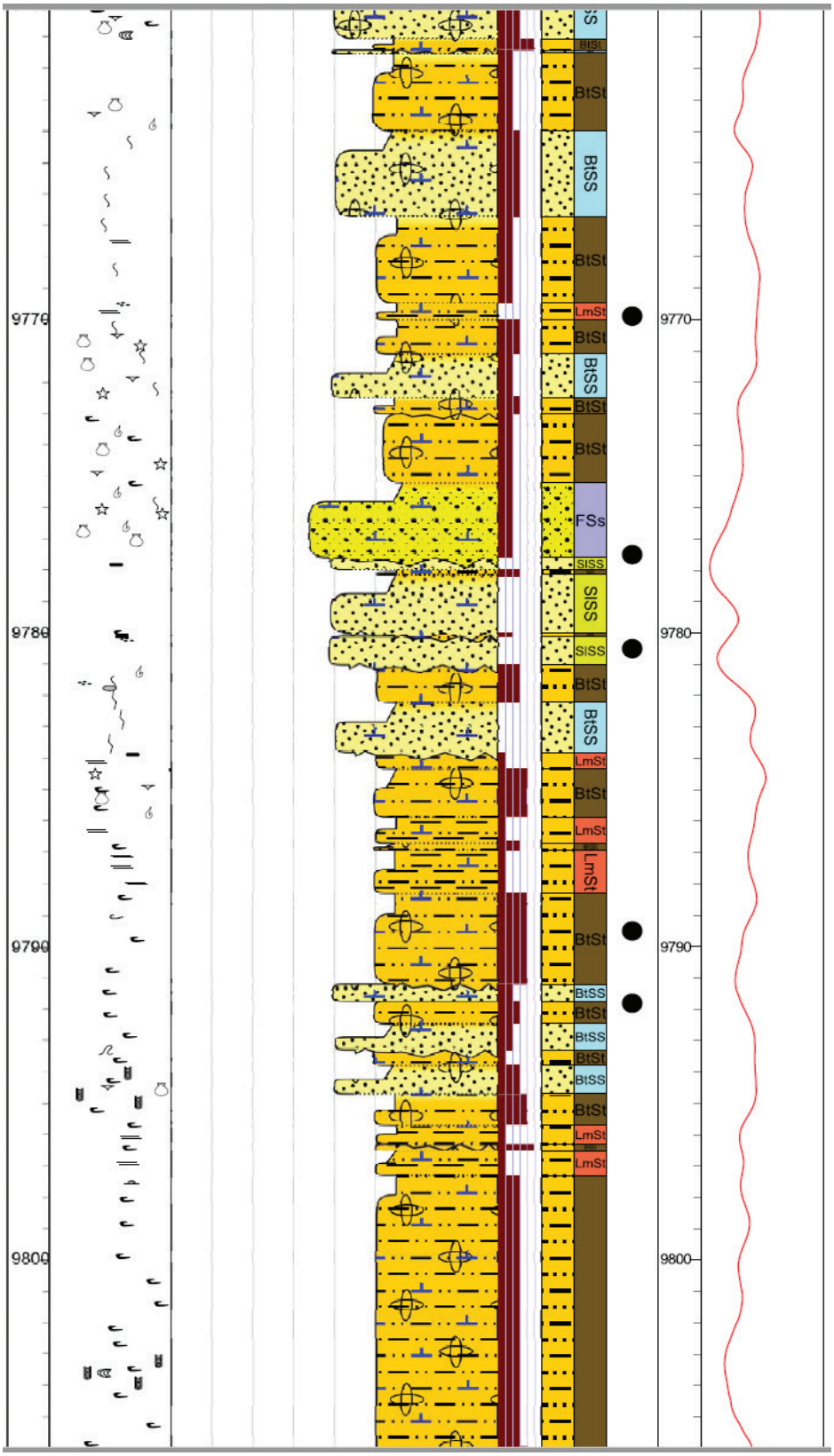
9770
9780
9790
9800
BtSS
BtSt
LmSt
FSs
SlSS

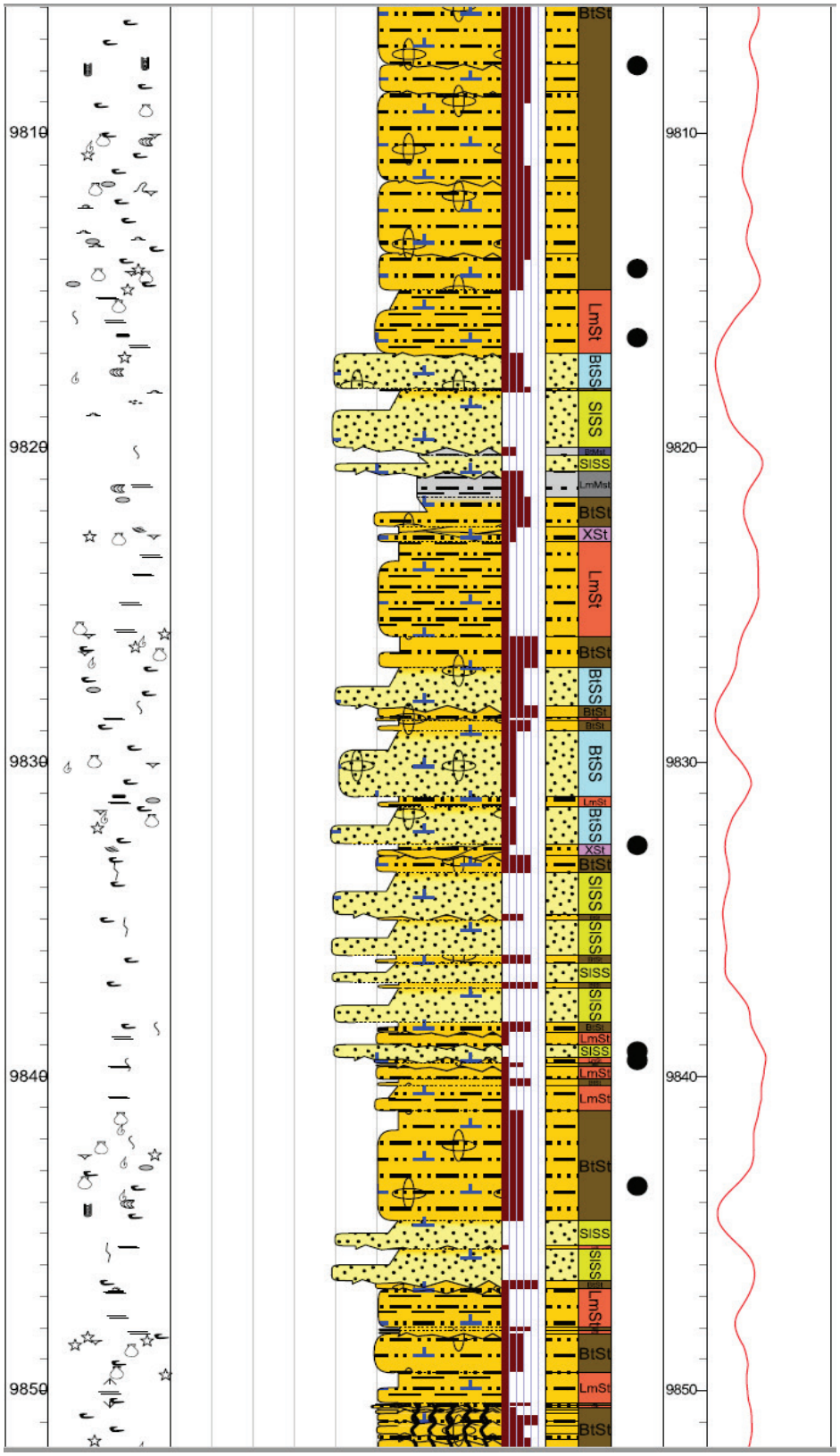
9810
9820
9830
9840
9850
BtSt
LmSt
BtSS
SlSS
LmMst
XSt

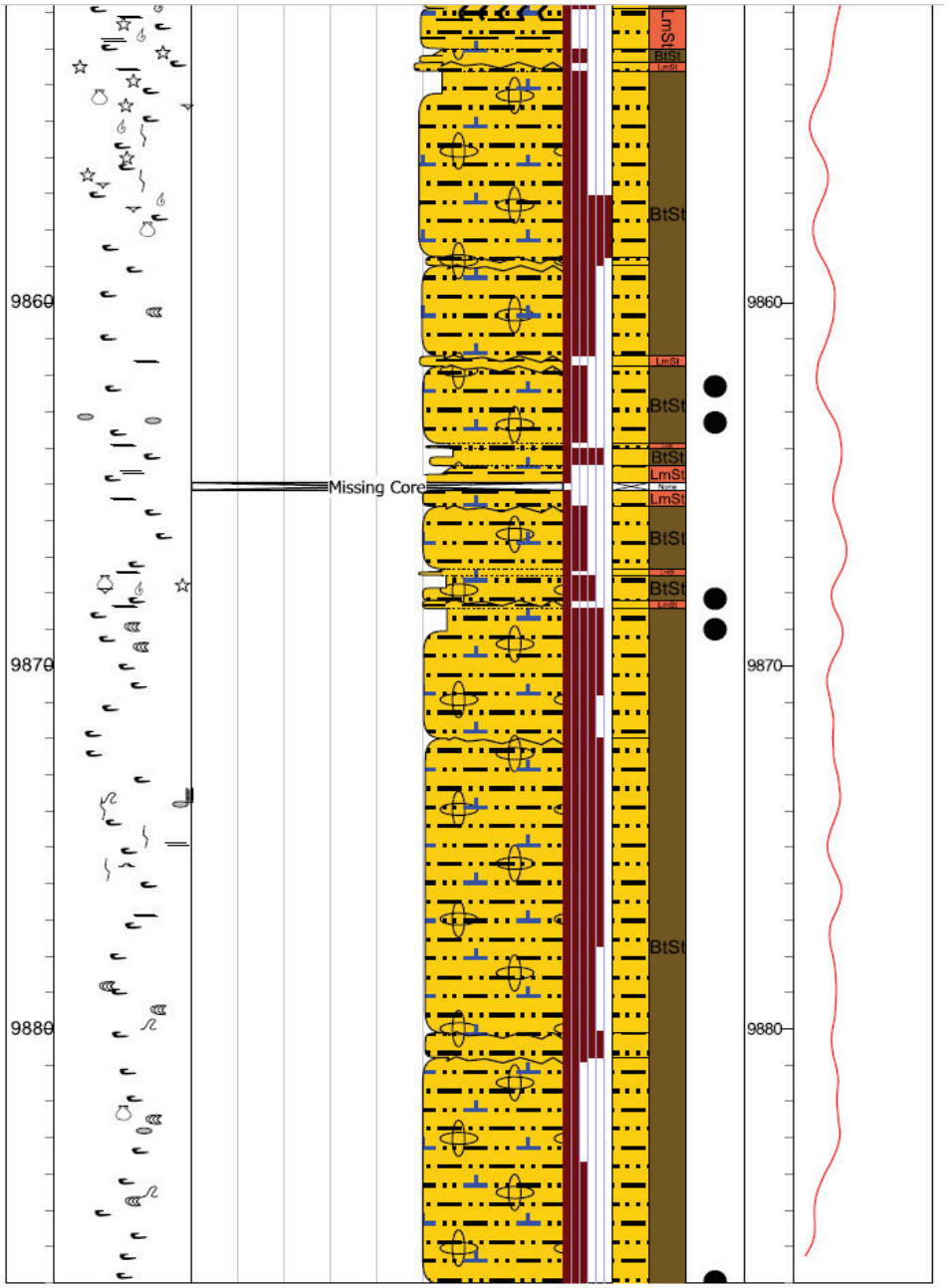
9860
9870
9880
Missing Core
LmSt
BtSt
LmSt
BtSt
BtSt
LmSt
None
LmSt
BtSt
BtSt
LmSt
BtSt
9860
9870
9880

Appendix B-2: Gulf Oil 1-25 Rohling

Well Name: Rohling 1-25	
Operator: Gulf Oil Corporation	**UWI No.:** 35011215690000
Basin: Anadarko	**Latitude:** 35.8383013
Country: United States	**Longitude:** -98.2211144
State: Oklahoma	**KB:** 1,220 ft
County: Blaine	**Well TD:** 10,732 ft
Field: Omega West	**Top of Core Description:** 9,714ft
Date: 2/25/1981	**Bottom of Core Description:** 9,924 ft

Lithologies


Mudstone


Siltstone


Very Fine Sandstone


Missing Core or Rubble Zone

Lithofacies


Laminated Mudstone


Bioturbated Siltstone


Structureless Sandstone


Bioturbated Mudstone


Bioturbated Sandstone


Laminated Siltstone


Cross-Stratified Siltstone

Admixture


Calcareous

Structure


Biotubated


Planar Laminated


Cross-bedded


Faintly Laminated

Fossils


Crinoids


Brachiopods


Bivalves


Fossil Fragments

Trace Fossils


Chrondrites


Phycosiphon


Skolithos


Zoophycus


Bioturbation Undifferentiated

Sedimentary Structures

Planar Laminations

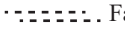
Faint Laminations


Cross Bedding

Scour Surface

Mud Whisps


Mud Clasts


Scour Surface

Diagentic Front ?


Small Fault

Accessories


Cemented Fractures


Ptygmatic Fractures

Py Pyrite

Contacts


Erosional


Striaght


Gradational


Scoured

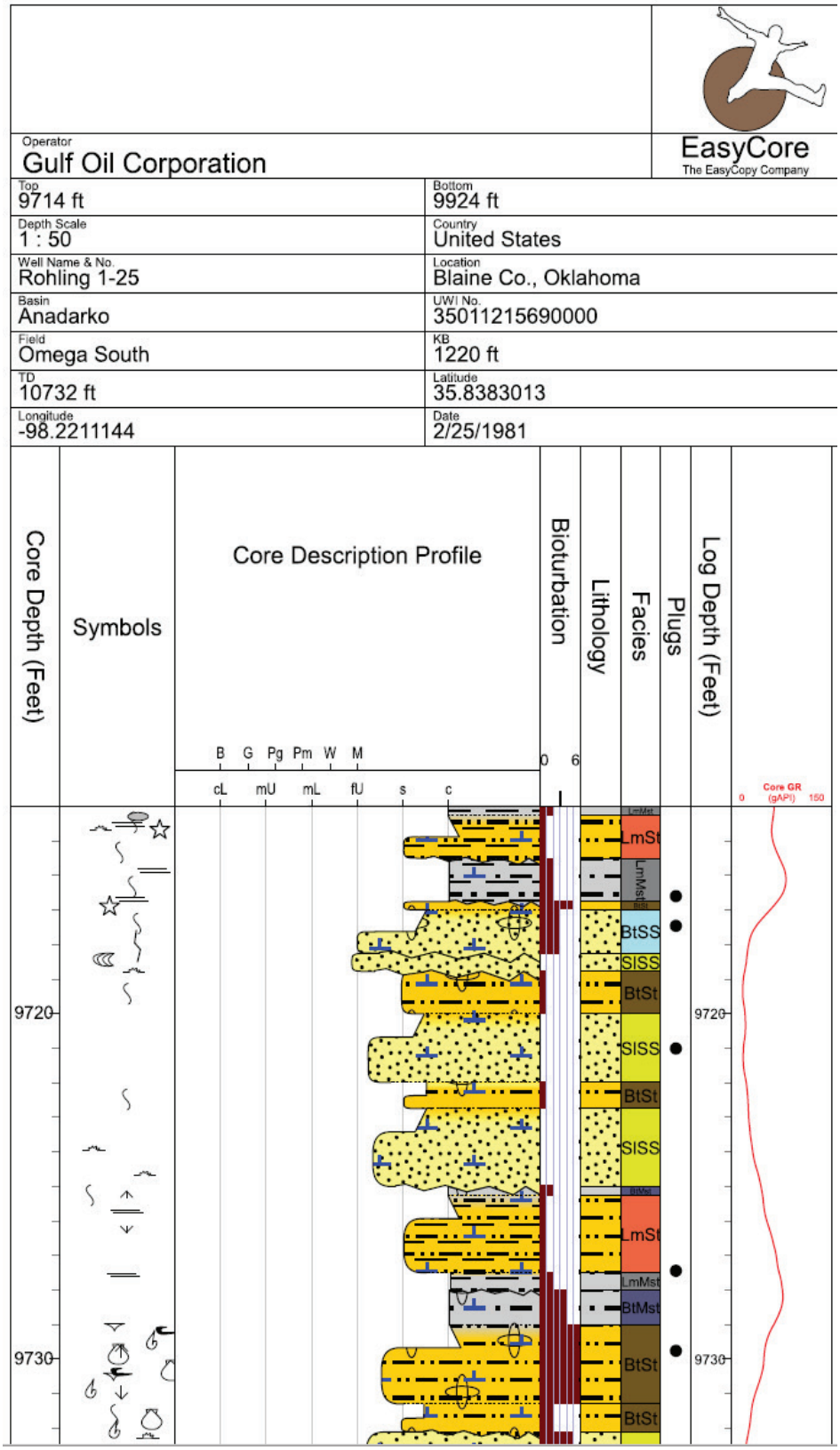
EasyCore
The EasyCopy Company
Operator
Gulf Oil Corporation
Top
9714 ft
Bottom
9924 ft
Depth Scale
1 : 50
Country
United States
Well Name & No.
Rohling 1-25
Location
Blaine Co., Oklahoma
Basin
Anadarko
UWI No.
35011215690000
Field
Omega South
KB
1220 ft
TD
10732 ft
Latitude
35.8383013
Longitude
-98.2211144
Date
2/25/1981
Core Depth (Feet)
Symbols
Core Description Profile
B G Pg Pm W M
cL mU mL fU s c
Bioturbation
0 6
Lithology
Facies
Plugs
Log Depth (Feet)
Core GR
0 (gAPI) 150
9720
9730
LmSt
LmMst
BtSS
SlSS
BtSt
SlSS
BtSt
SlSS
LmSt
LmMst
BtMst
BtSt
BtSt

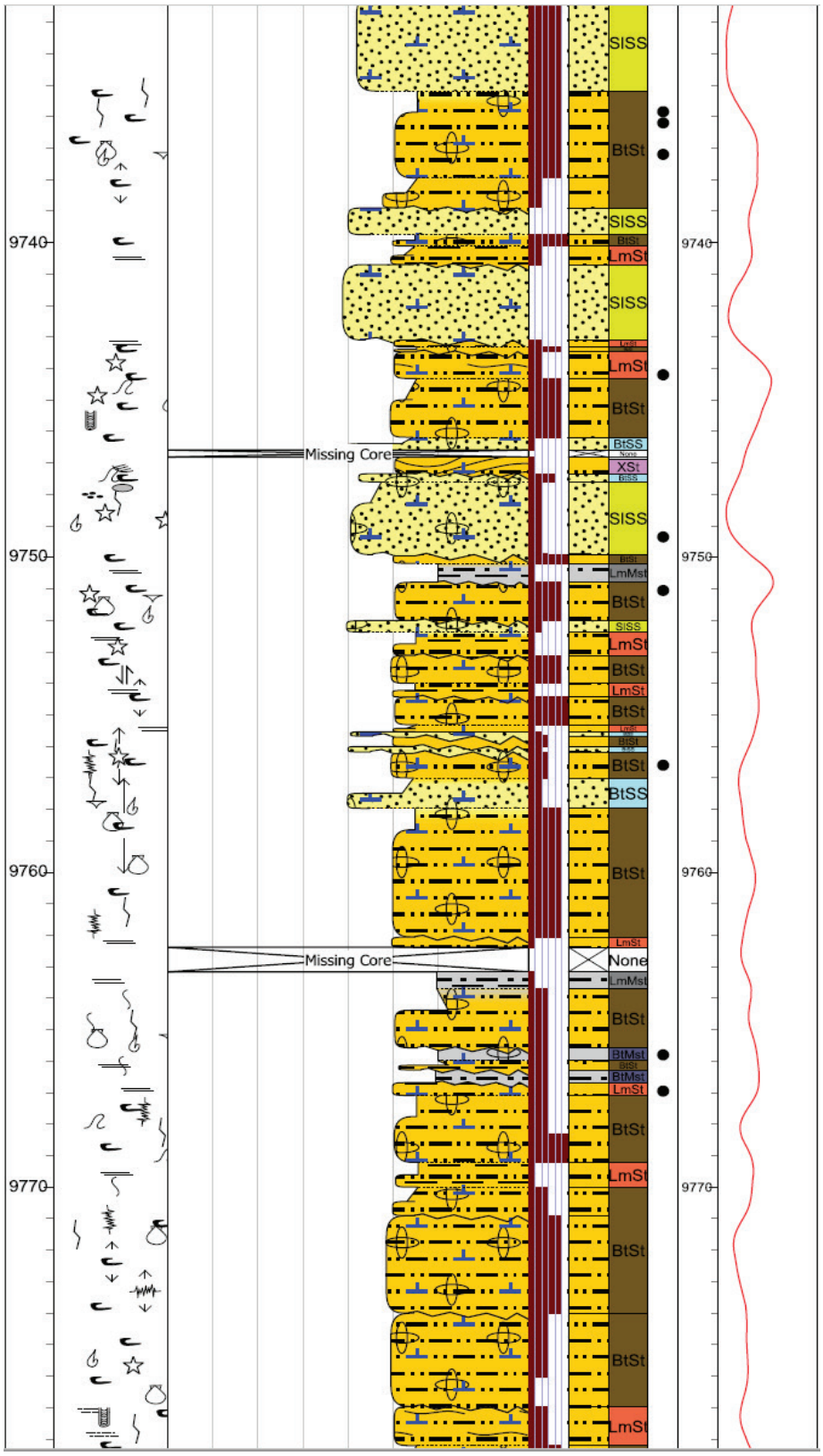
9740
9750
9760
9770
Missing Core
Missing Core
None
SISS
BtSt
LmSt
BtSS
XSt
LmMst
BtMst

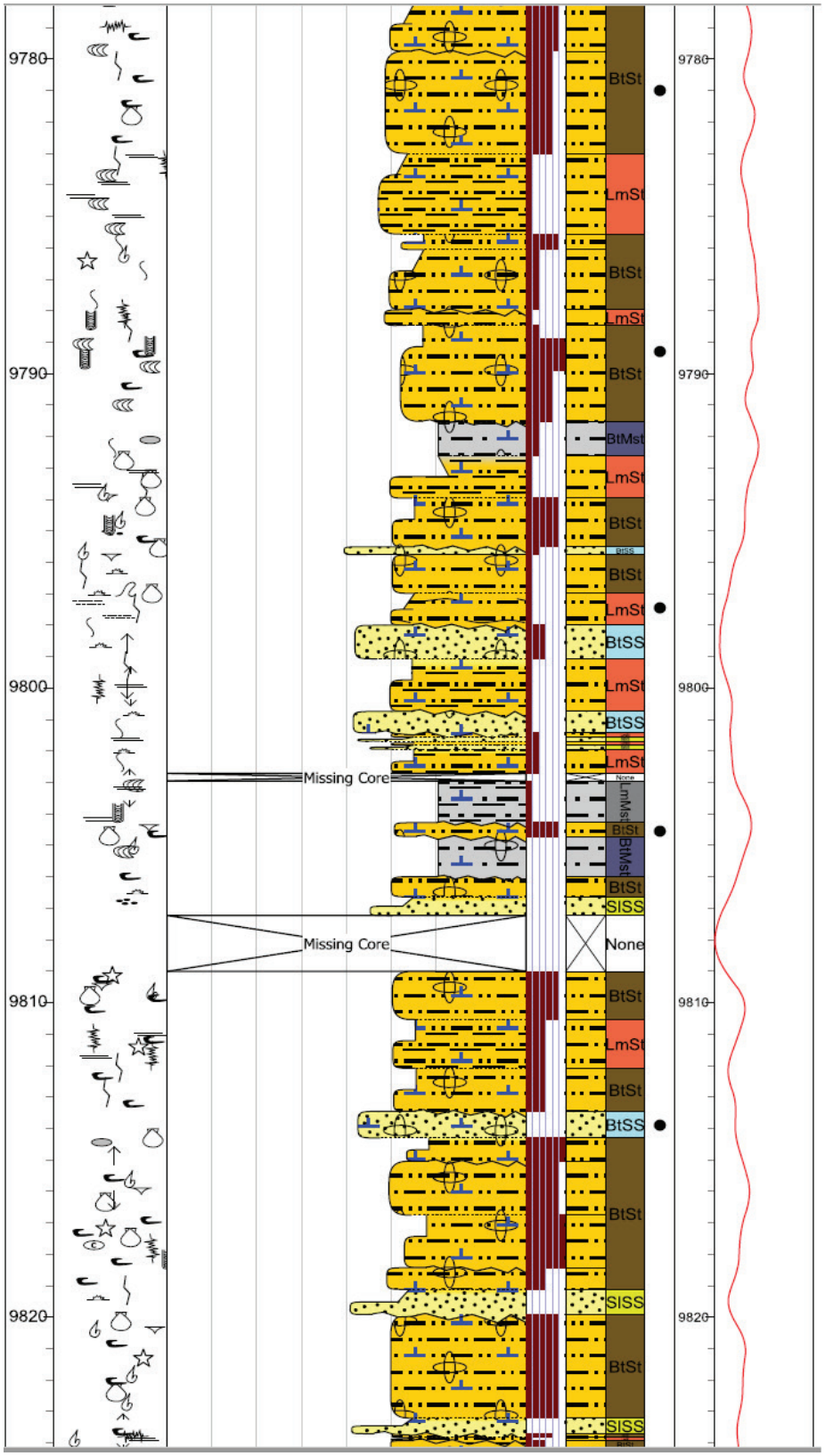
9780
9790
9800
9810
9820
Missing Core
Missing Core
BtSt
LmSt
BtSt
LmSt
BtSt
BtMst
LmSt
BtSt
SISS
BtSt
LmSt
BtSS
LmSt
BtSS
LmSt
None
LmMst
BtSt
BtMst
BtSt
SISS
None
BtSt
LmSt
BtSt
BtSS
BtSt
SISS
BtSt
SISS

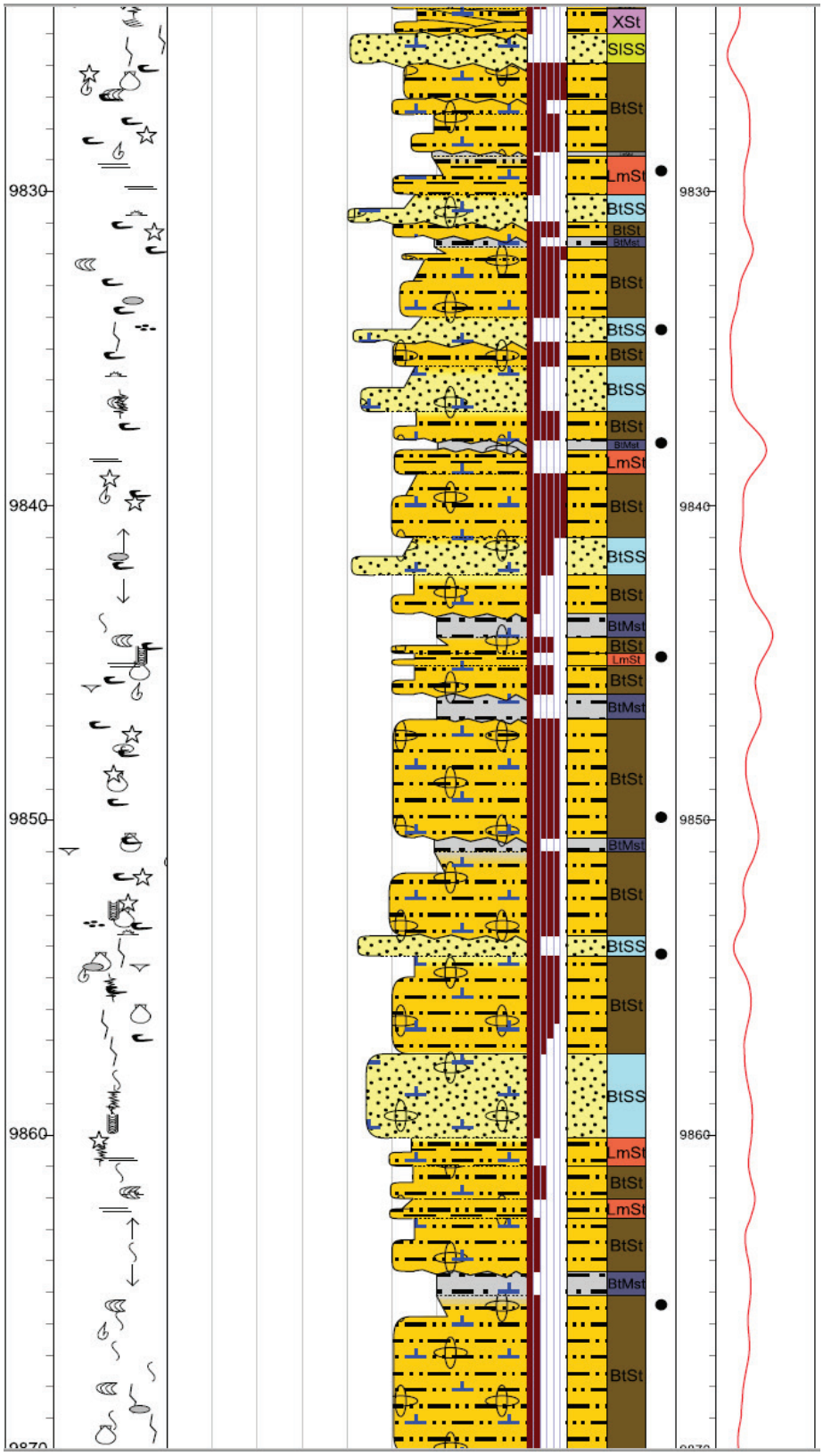
XSt
SlSS
BtSt
LmSt
BtSS
BtSt
BtMst
BtSt
BtSS
BtSt
BtSS
BtSt
BtMst
LmSt
BtSt
BtSS
BtSt
BtMst
BtSt
LmSt
BtSt
BtMst
BtSt
BtMst
BtSt
BtSS
BtSt
BtSS
LmSt
BtSt
LmSt
BtSt
BtMst
BtSt
9830
9840
9850
9860
9870

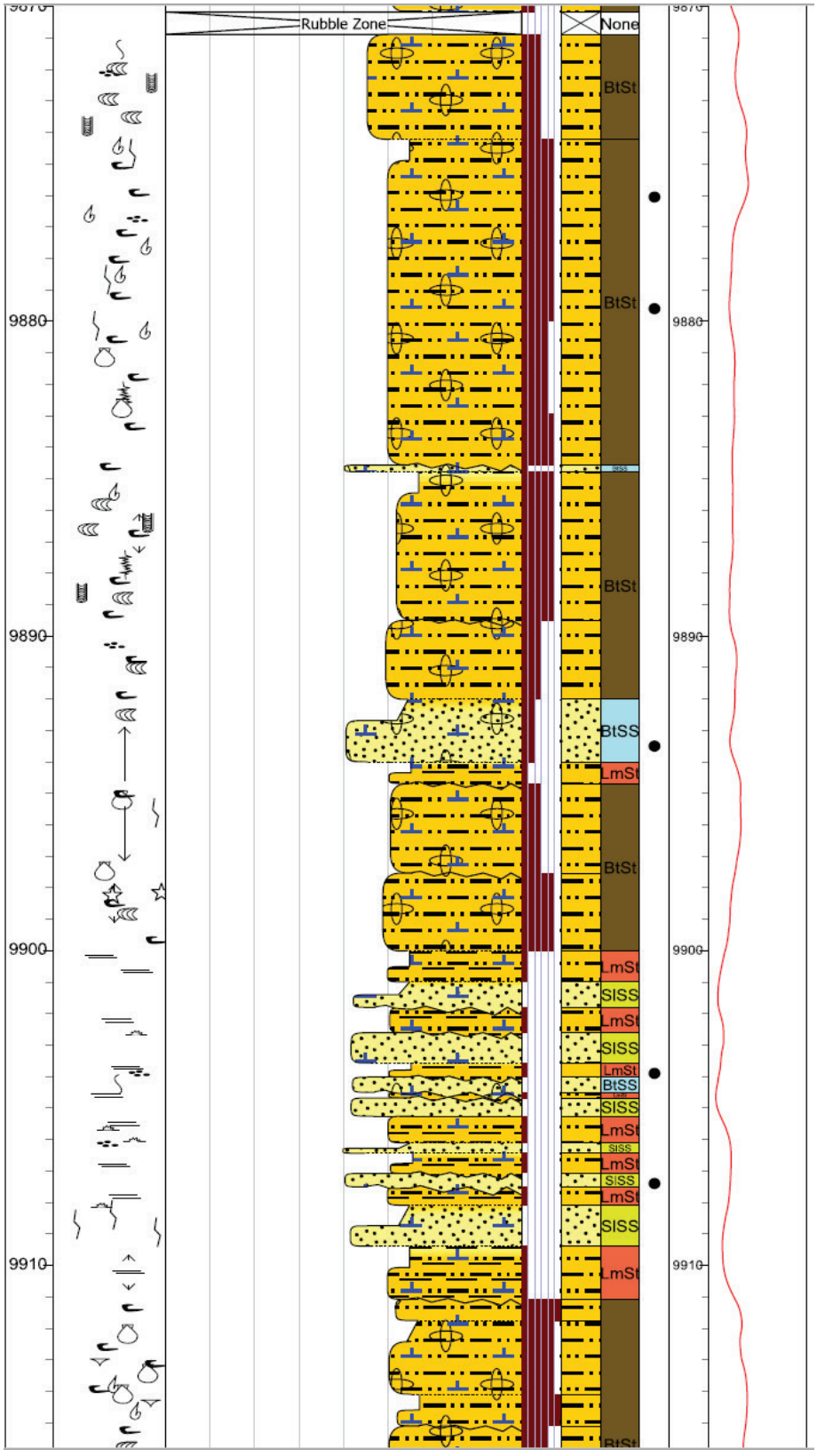
Rubble Zone
None
BtSt
BtSt
BtSt
BtSS
LmSt
BtSt
LmSt
SISS
LmSt
SISS
LmSt
BtSS
SISS
LmSt
SISS
LmSt
SISS
LmSt
SISS
LmSt
BtSt
9880
9890
9900
9910

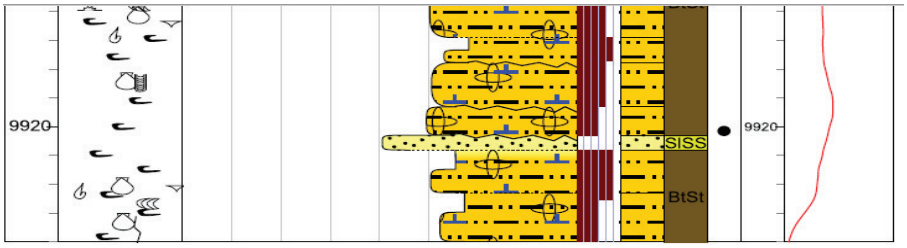
9920
SISS
BtSt
9920

Appendix B-3: Gulf Oil 1-14 Musselman

Well Name: Musselman 1- 14	
Operator: Gulf Oil Corporation	**UWI No.:** 35011210140000
Basin: Anadarko	**Latitude:** 35.8655820
Country: United States	**Longitude:** -98.2366910
State: Oklahoma	**KB:** 1,232 ft
County: Blaine	**Well TD:** 11,070 ft
Field: Omega West	**Top of Core Description:** 9,965 ft
Date: 8/24/1979	**Bottom of Core Description:** 10,058 ft

Lithologies

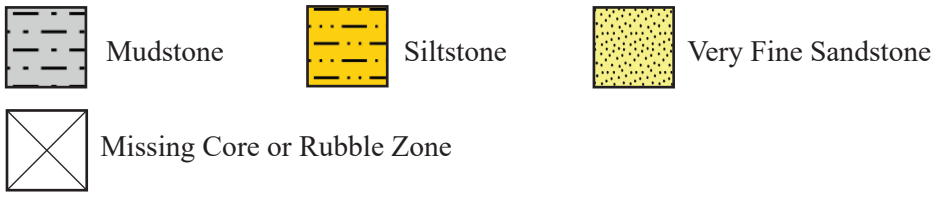

Lithofacies

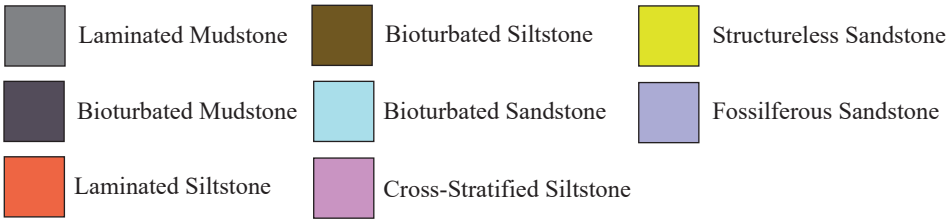

Admixture

Structure

Fossils

Trace Fossils

Sedimentary Structures

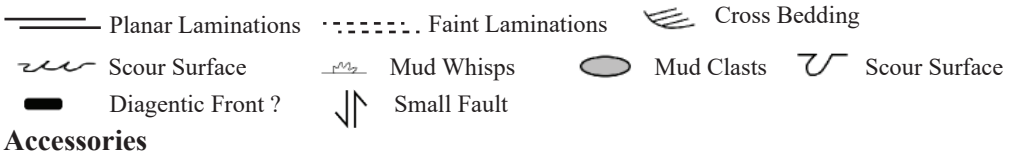

Accessories

Contacts

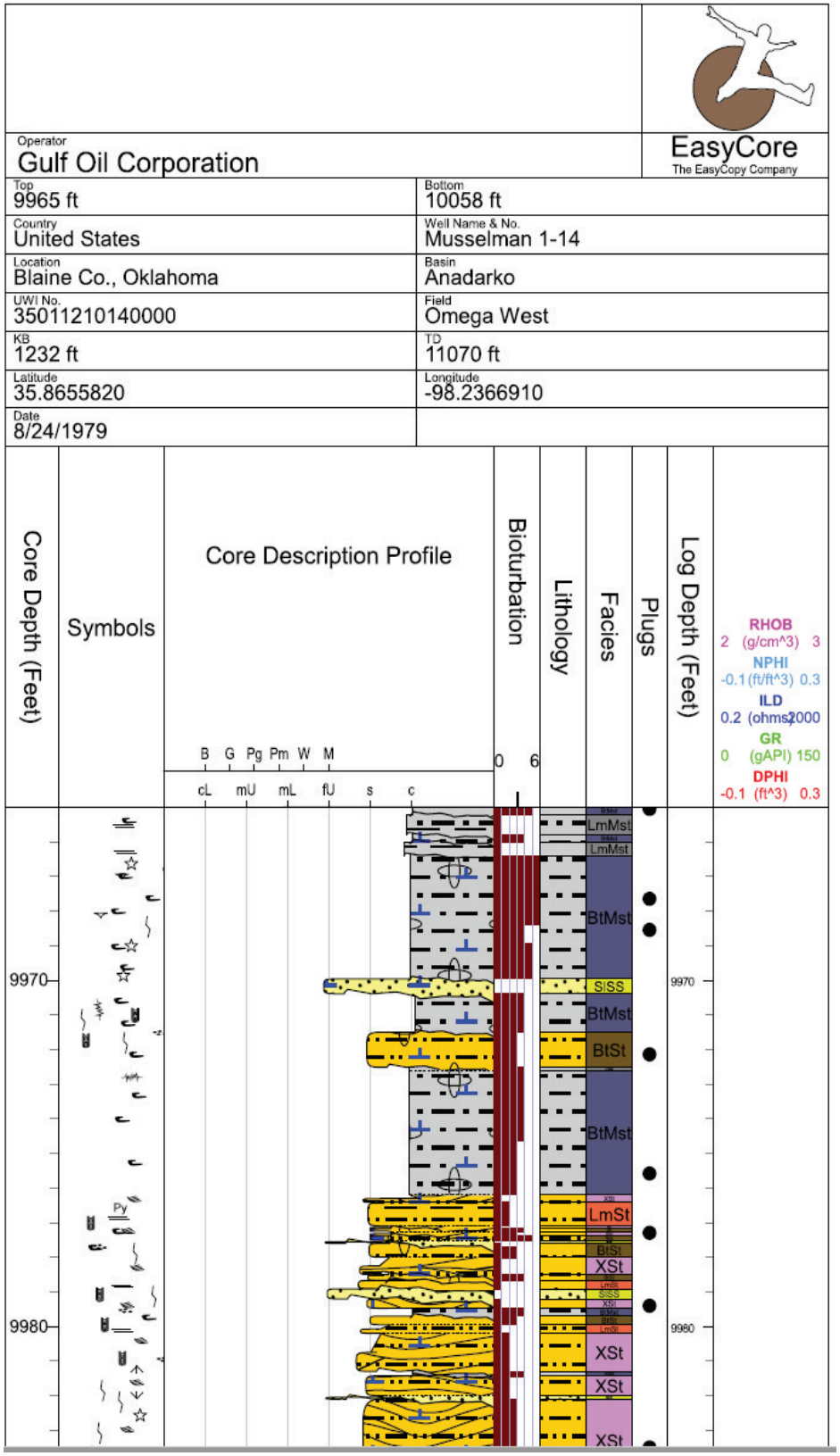
EasyCore
The EasyCopy Company
Operator
Gulf Oil Corporation
Top
9965 ft
Bottom
10058 ft
Country
United States
Well Name & No.
Musselman 1-14
Location
Blaine Co., Oklahoma
Basin
Anadarko
UWI No.
35011210140000
Field
Omega West
KB
1232 ft
TD
11070 ft
Latitude
35.8655820
Longitude
-98.2366910
Date
8/24/1979
Core Depth (Feet)
Symbols
Core Description Profile
B G Pg Pm W M
cL mU mL fU s c
Bioturbation
0 6
Lithology
Facies
Plugs
Log Depth (Feet)
RHOB
2 (g/cm^3) 3
NPHI
-0.1 (ft/ft^3) 0.3
ILD
0.2 (ohms) 2000
GR
0 (gAPI) 150
DPHI
-0.1 (ft^3) 0.3
9970
9980
LmMst
BtMst
SiSS
BtMst
BtSt
BtMst
LmSt
BtSt
XSt
SiSS
XSt
XSt
XSt
Py

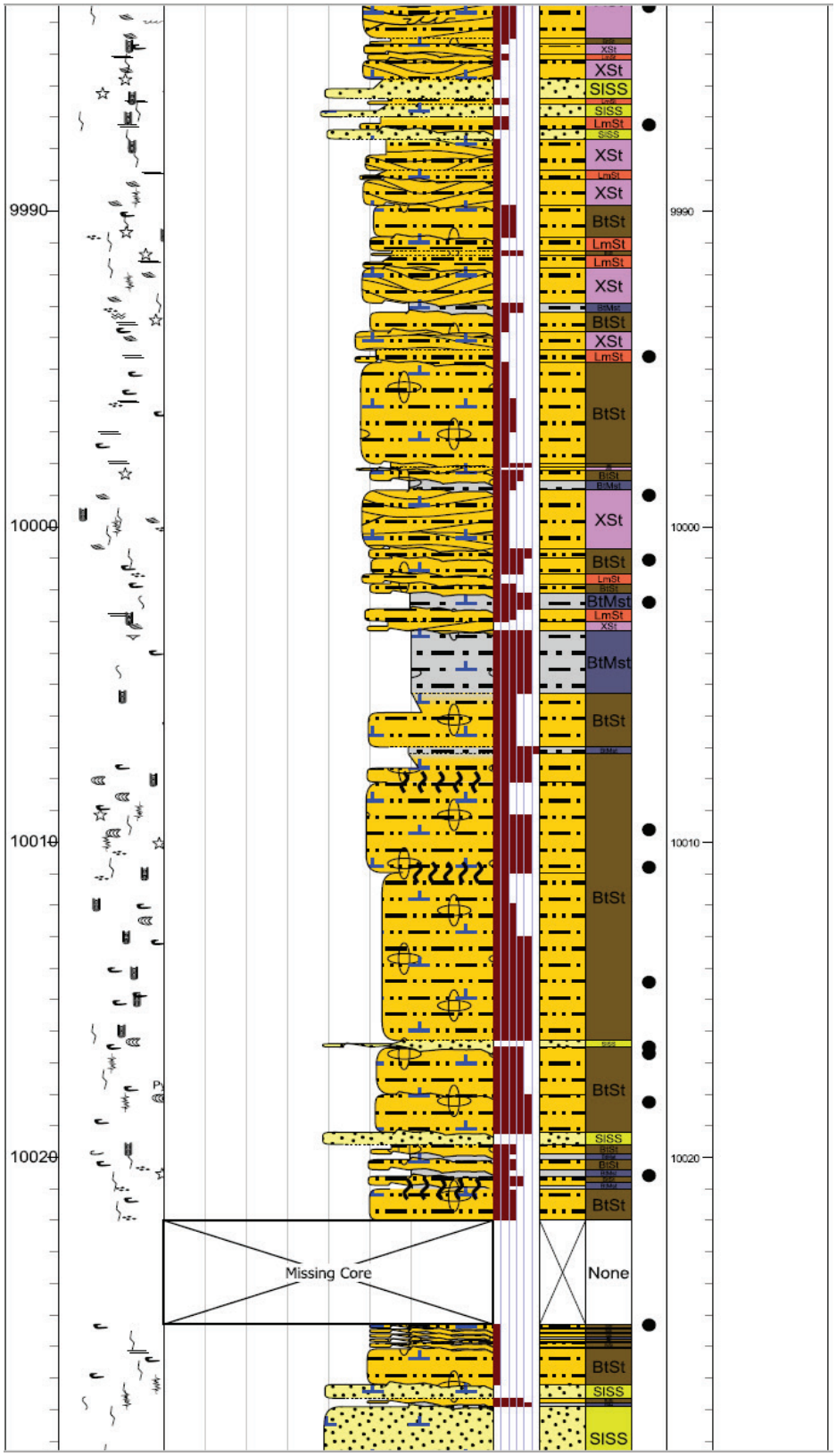
9990
10000
10010
10020
XSt
SlSS
LmSt
BtSt
BtMst
Missing Core
None

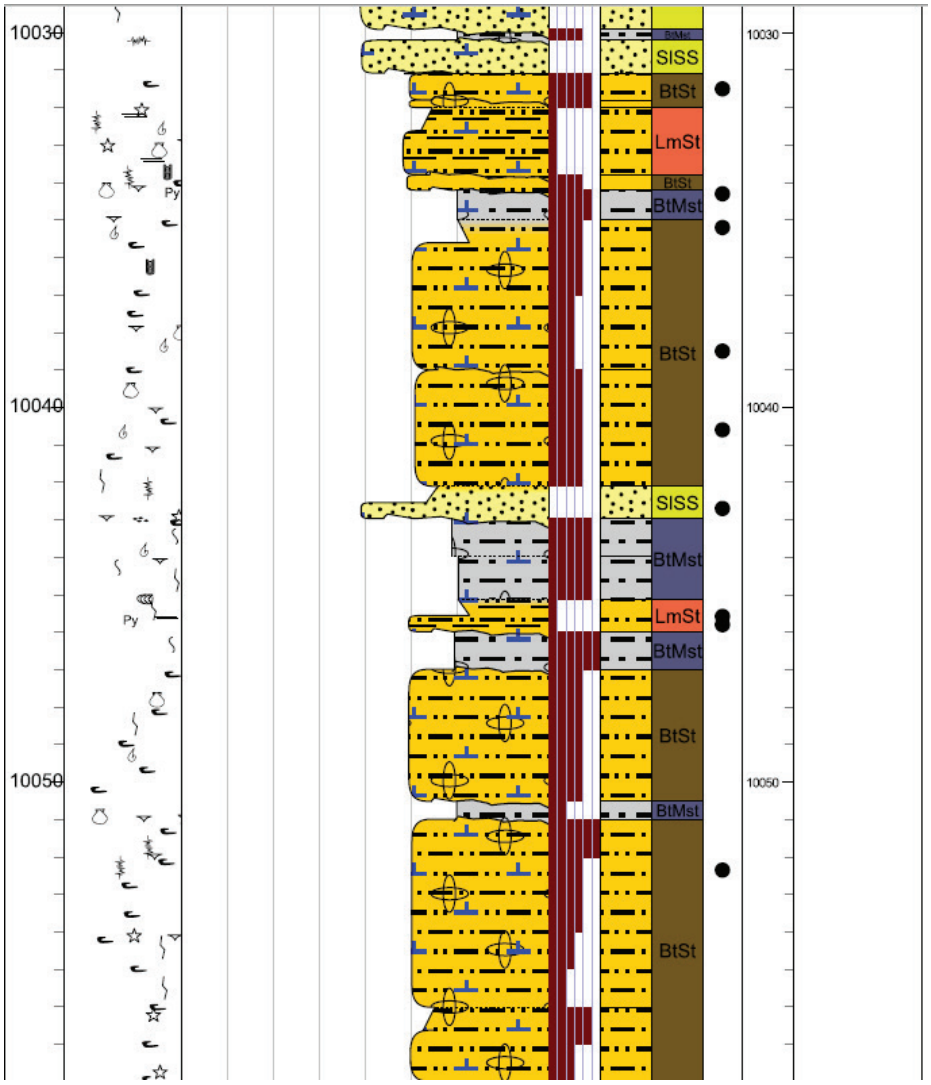
10030
10040
10050
Py
Py
SlSS
BtSt
LmSt
BtSt
BtMst
BtSt
SlSS
BtMst
LmSt
BtMst
BtSt
BtMst
BtSt
10030
10040
10050

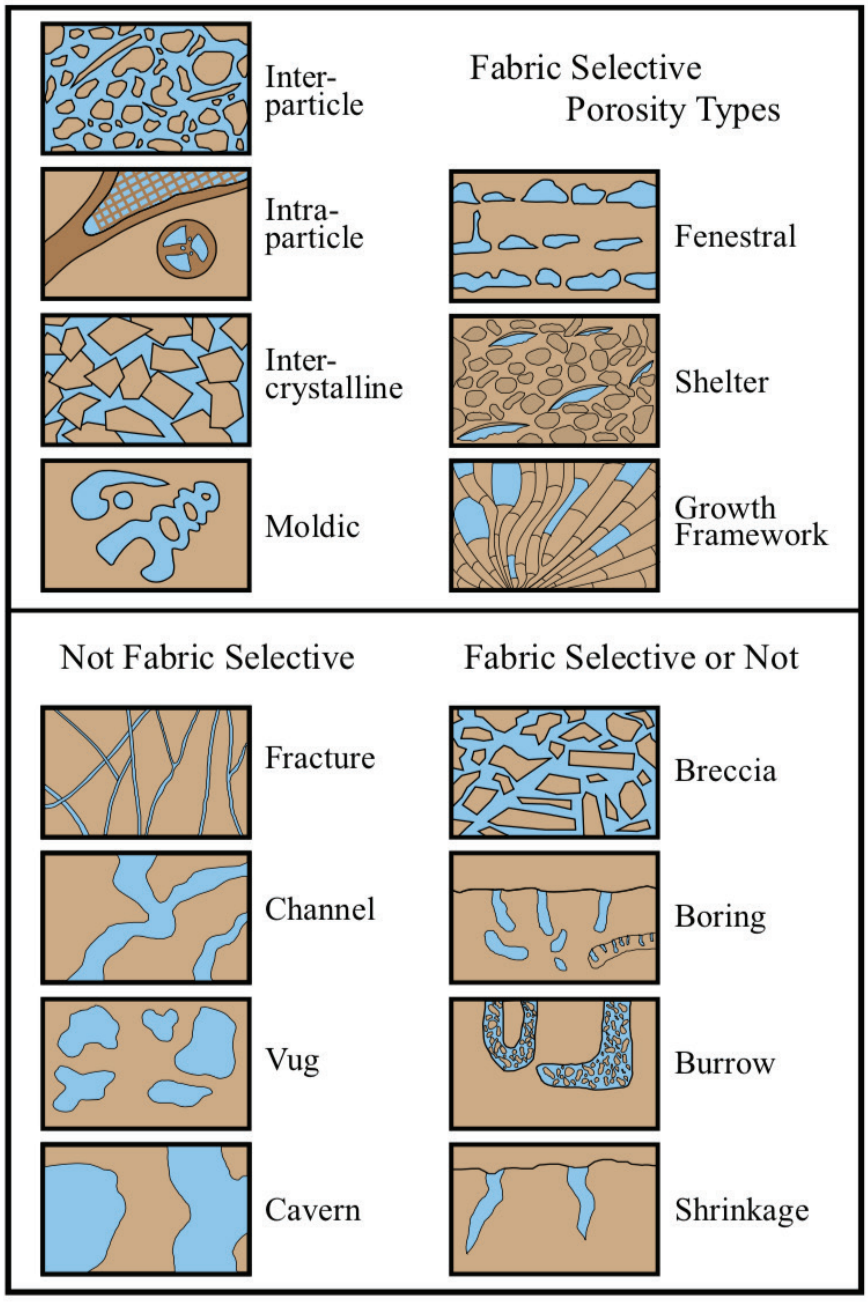

Appendix B-4: Diagram representing the Choquette and Pray (1970) classification of fabric selective andnon-fabric selective porosity types (modified from Sholle and Ulmer-Scholle, 2013).

Appendix C: Lithofacies Descriptions and Interpretations

Appendix C-1: Proximal Lithofacies

Facies 1: Skeletal Grainstone

Skeletal grainstone is light gray to white in color, grain-supported consisting of echinoderms, brachiopods, peloids, sponge spicules, bryozoans, crinoids, and undifferentiated fossil fragments (Figure 6A, Figure 7A). Spicules are less frequent than the fragments. No micrite is observed in these facies. This facies exhibits an average porosity of about 2.5% with an average permeability of 0.003 mD (Figure 10). Moldic porosity is detected where some skeletal grains were dissolved out. This facies occasionally exhibits bleaching, silica replacement, dolomitization, and concentrated zones of chert. Skeletal grainstone is interpreted to have been deposited proximal to a skeletal shoal on the mid-to-inner carbonate ramp, near fair weather wave base (FWWB) based on the diverse fossil assemblages and observed Truncation surfaces and laminations (Figure 8).

Facies 2: Peloidal Packstone to Grainstone

The peloidal packstone to grainstone is light gray, grain-supported consisting of abundant peloids and skeletal fossil fragments, including: brachiopods, crinoids, and some spicules (Figure 6B, Figure 7B). Some micrite is observed despite being grain-dominated. Sedimentary structures include bioturbation and styolites. Chert-rich zones are frequent from silica replacement. Fluid invasion completely altered the original fabric with silica and dolomite from the diagenetic fronts observed. Average porosity value is

about 3.9% (Figure 10). Higher porosity correlates to the alteration related to dissolution and fluid invasion. This facies is interpreted as being deposited on the mid-ramp, proximal to skeletal shoals (Figure 8). The presence of peloids suggests a more restricted environment, inactive portion of a shoal.

Facies 3: Bioturbated Wackestone to Packstone

Bioturbated wackestone to packstone is a medium gray facies composed of peloids, sponge spicules, crinoids, and brachiopods, often exhibiting abundant bioturbation (Figure 6C, Figure 7C). Average porosity and permeability values are 2.1% and 0.05 mD (Figure 10). This facie represents the transitional region of ramp from to mid to outer (Figure 8).

Facies 4: Bioturbated Mudstone to Wackestone

Bioturbated mudstone to wackestone is gray, matrix-supported calcareous mudstone with micrite as the principle constituent (Figure 6D, Figure 7D). Sponge spicules are the most common skeletal fragments. Bioturbation and occasional laminations are present and show mottled texture from the intense burrowing. This lithofacies is interpreted to be deposited on the outer ramp, below FWWB in a low energy environment (Figure 8).

Facies 5: Dolomitized wackestone

Dolomitized wackestone is a medium grey, mud-dominated rock with micrite as the main constituent (Figure 6E, Figure 7E). This facies is characterized by euhedral

rhombs suggesting a restricted marine to supratidal depositional environment (Figure 8). Restriction could have resulted from poor circulation over a broad shelf with weak to no currents in an area blocked form open water by a shoal, creating favorable condition for dolomite formation with higher saturations of CaMg in the water (Deffeyes et al., 1965). Chert-rich zone are often observed throughout. Dolomitized wackestone exhibits an average porosity is 3.2 % (Figure 10).

Facies 6: Altered Chert

Altered chert is characterized by abundant chert clasts marked by silica replacement of limestone, tripolite, and residual calcite dissolution from subaerial exposure and fluid invasion. (Figure 6F, Figure 7F). Typically, the originally fabric has been destroyed. Exhibits the highest porosity (>20%) and permeability values, due to the dissolution creating vuggy, and moldic porosity (Figure 10). Creation of this lithofacies is related to regions of the carbonate ramp directly affected by sea level changes.

Facies 7: Glauconitic Sandstone

The glauconitic sandstone is composed of green, sub-rounded, moderately sorted, fine-sized grains of glaucontie (25%) (Figure 6G, Figure 7G). The glauconitic grains are encompassed in a matrix of fine to medium sized quartz grains. Rare fossil fragments are observed. Porosity value for this facies is 1.7 % (Figure 10) and typically displays partial moldic porosity within skeletal fragments. Syntaxial cement was observed to reduce this porosity. Glaucontie can be formed in a variety of depositional environments, but typically during initial transgression in a low-energy, low oxygen submarine environment

with very low sedimentation rates (Middleton et al. 2003; Flinton, 2016). Formation of glaucontie requires abundant potassium and iron from smectite clays and forms authigenically in reducing environments (Burst, 1958; Bentor and Kastner, 1965). The presence of quartz, glaucontie, and thin-shelled brachiopods suggest a low energy environment. In this case the glauconitic sandstone was interpreted to be deposited in a restricted, low energy and oxygen, deep water setting below storm weather wave base (SWWB) (Figure 8).

Facies 8: Siliceous Shale

Siliceous shale is very dark gray to black in color and consist predominantly well sorted, fine-grained clays with varying amounts of quartz grains. (Figure 6H, Figure 7H).

Appendix C-2: Distal Lithofacies

Facies 1: Fossiliferous Calcareous Very-Fine Sandstone

Medium gray calcareous fossiliferous sandstones contain well-sorted, sub-angular, very-fine sized quartz grains and calcite (Figure 11A, Figure 12A). This lithofacies is composed of abundant fossil fragments, including: bivalves (2%), bryozoans (2%), crinoids (8%), brachiopods (7%), and peloids (25%). Calcite cement (35%) is observed surrounding the fossil fragment leading to cement occluding the pore space and the contributing to the low porosity values (<2%) (Figure 10). Observations of faint laminations suggest deposition on the mid-ramp near FWWB (Figure 8).

Facies 2: Structureless Calcareous Very-Fine Sandstone

Structureless calcareous sandstones are light gray in color and consist of well-sorted, sub-angular to sub-rounded, very-fine sized quartz grains and calcite (Figure 11B, Figure 12B). Sedimentary structures are not observed, making it structureless in nature. These siltstones are highly calcite-cemented (45-70%) leading to low porosities (<1%) (Figure 10). Many calcite-filled fractures are present within this facies. These fractures terminate at the bedding plane of other softer lithofacies, indicating there is a change in the mechanically stratigraphy. Rare fossil fragments and no sedimentary structures are present suggesting a low-oxygenated and low-energy environment likely on the outer ramp to the basin floor settings (Figure 8).

Facies 3: Bioturbated Calcareous Very-Fine Sandstone

Bioturbated calcareous sandstones are gray and composed of well-sorted, sub-angular, very-fine sized quartz grains, calcite and clays (20%) (Figure 11C, Figure 12C). This facies is characterized by abundant bioturbation, typically phycosiphons trace fossils. Clay in-filled these trace fossils making them relatively darker than the surrounding matrix and therefore providing lesser amounts of calcite cement. Some fossils are present, including crinoids and brachiopods. These siltstones are also calcite cemented. Bioturbation indicates deposited occurred along the mid-ramp within FWWB (Figure 8).

Facies 4: Laminated Calcareous Siltstone

Laminated calcareous siltstones are gray and composed of sub-angular to sub-rounded, well-sorted silt sized quartz grains, calcite and clays (30 %) (Figure 11D, Figure 12D). This facies is characterized by planar laminations. Higher amounts of calcite cement are observed (35%). Occasional fossil fragments include peloids, brachiopods and crinoids. Laminated siltstones are interpreted to be deposited along the transition from middle to outer ramp as suggested the laminations like caused by tidal of storm waves within FFWB (Figure 8).

Facies 5: Cross-bedded Calcareous Siltstone

Cross-bedded calcareous siltstones are gray and composed of sub-angular, silt sized quartz grains, calcite, and clays (Figure 11E, Figure 12E). Some fossils include brachiopods and crinoids. This facies is characterized by cross-bedded laminations. These

features tend to mark a calmer, deeper setting, transitioning to offshore environment. Cross-bedding suggests that these siltstones are wave-action influenced in a high-energy nearshore environment of the prograding shoreline (Figure 8). Also likely to have been influenced by storm waves and tidal motion near fair-weather wave base (FWWB). Successions of stacked siltstone litholfacies have been identified to represent Bouma turbidite sequences (Miller, 2018) (Appendix C-3).

Facies 6: Bioturbated Calcareous Siltstone

Bioturbated calcareous siltstones are medium to dark gray and composed of moderately sorted, sub-angular, silt sized quartz grains, calcite, clays (~35%) (Figure 11F, Figure 12F). This facies is characterized by abundant bioturbation, including: phycosiphon, zoophycos, and skilithos. Clay filled in these trace fossils, which led to clay obstructing calcite cementation within the pore space creating higher average porosities of 4.3% (Figure 10 A-B). Some fossils are present including crinoids and brachiopods. Bioturbated siltstones are interpreted to be deposited along the transition from middle to outer ramp due to the increase in clay content and evident abundant bioturbation (Figure 8). These features tend to mark a calmer, deeper setting, transitioning to offshore environment.

Facies 7: Laminated Calcareous Mudstone

Laminated calcareous mudstone is dark gray to black in color and composed of mostly of clay minerals (>55%) and calcite (Figure 11G, Figure 12G). Some silt-sized quartz grains and infrequent fossil fragments are observed throughout. Lesser amounts of

calcite-cement are observed (<12%). Faint laminations mark this lithofacies. This facies is interpreted as one of deepest depositional environments, likely deposited offshore in the basin floor near or below storm wave base (SWB) (Figure 8). Increase in clay content with faint laminations indicates lower energy, calmer deeper environments.

Facies 8: Bioturbated Calcareous Mudstone

Bioturbated calcareous mudstone is dark gray to black in color and composed mostly of clay minerals (>60%) and calcite (Figure 11H, Figure 12H). Some silt-sized quartz grains and infrequent fossil fragments are observed throughout, little to no calcite-cement is present in this facies. Light bioturbation marks this lithofacies. Bioturbated mudstones exhibit higher porosities due to lesser amounts of calcite-cement (3.5 %) (Figure 10 A-B). This facies is interpreted as one of deepest depositional environments, likely deposited offshore in the basin floor near or below storm wave base (SWB) due to the lack of fossils and sedimentary features (Figure 8).

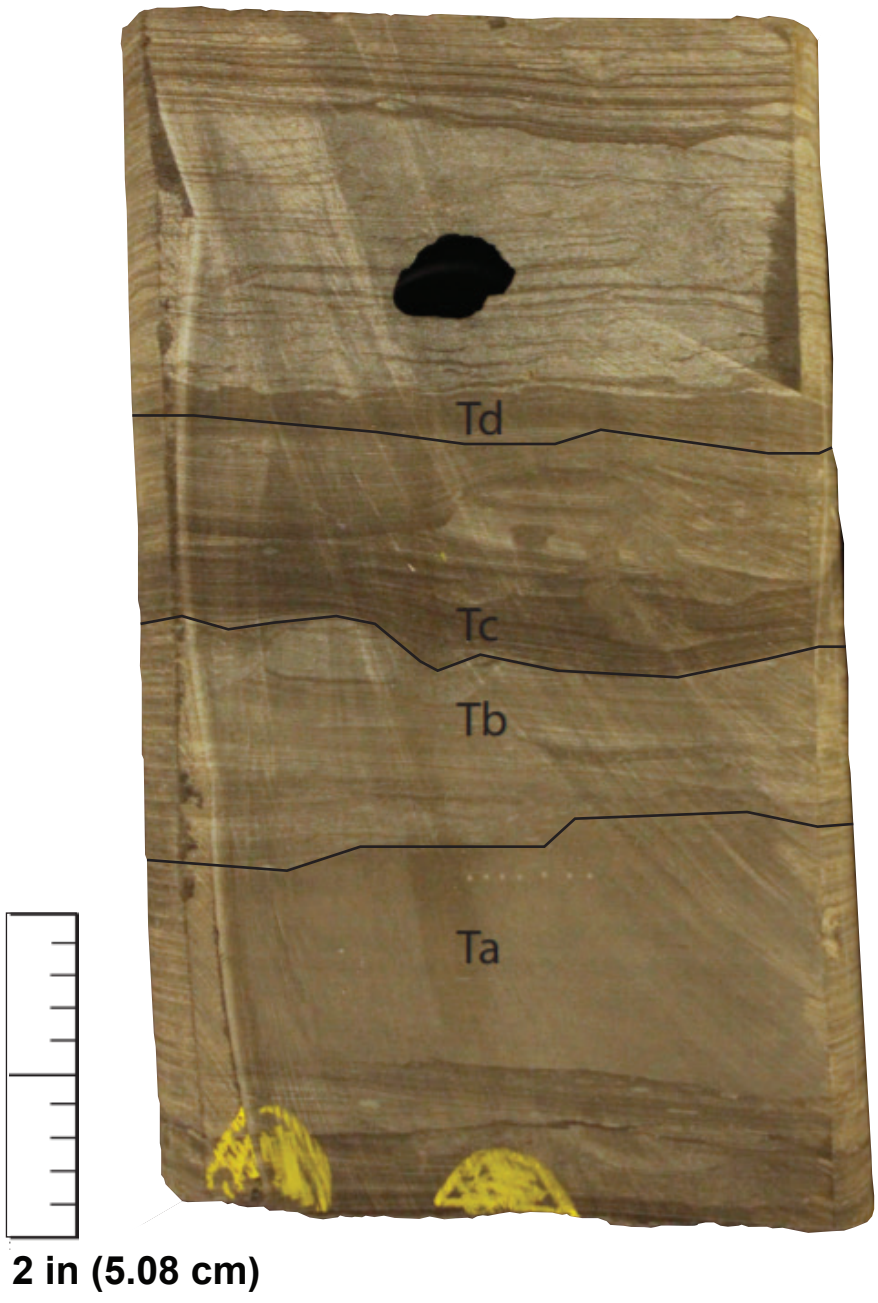

Appendix C-3: Possible Bouma sequence of a turbidite flow from the Gulf Oil 1-23 Shaffer (9678 ft [2950 m] MD) that are fining-upward sequences with increasing mud content from Ta to Td. Consists of: (Ta) structureless calcareous very-fine sandstone, (Tb) laminated calcareous siltstone, (Tc) cross-bedded calcareous siltstone, and (Td) faintly laminated calcareous siltstone to calcareous mudstone.

Appendix D: Electrofacies Classification and Lithology

Appendix D-1: Log Normalization

Due to the sensitivity of electrofacies classification to well-log values, normalization is an important step to ensure accurate lithology prediction. The normalization process recalibrates the log measurements to match to neighboring wells to make the data compatible with the other wells. In order to not remove any of the natural geological variations, normalization was only carried out on wells that did not fit in with the majority of the wells in the same area. For this study, gamma ray curves were normalized to a nearby by type well for GR distributions. The GR log from the type wells were used to create GR histograms for the zone of interest. The histograms shows the character of the GR log and the frequency in which the desired log statistics should be for the zone. The GR curves that required normalization were then normalized to the GR histogram of the nearby type well by the Base Line Shift method. The base line shift method adjusts each curve to a common scale by subtracting or adding the curve's current baseline and adding or subtracting back in the desired baseline value (Figure C-1). The baseline is defined from the histogram by determining the average. Other curves used in this study including: NPHI, RESD, and DPHI were not normalized because of the high risk of creating erroneous values during normalization (Shier, 2004).

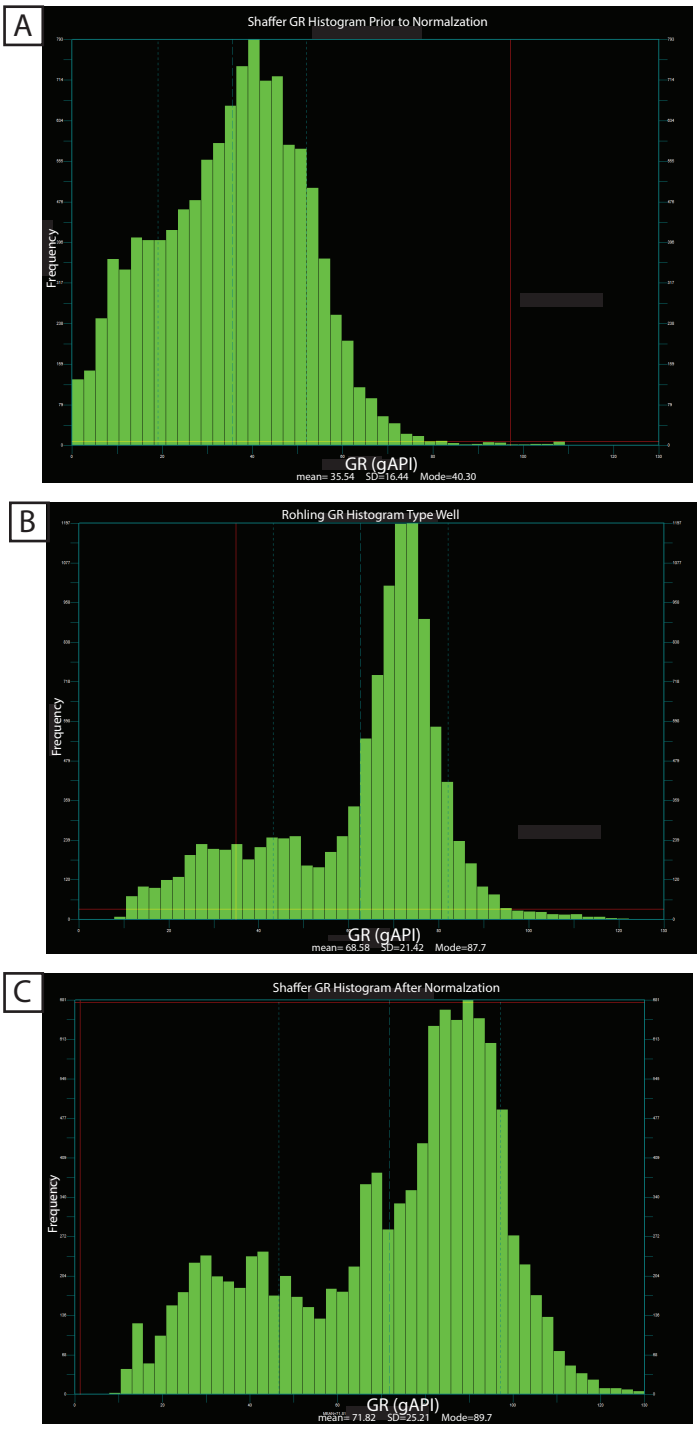

Appendix D-1: (A) Example of a histogram of a GR curve of the top Meramec to top of the Woodford prior to normaization. (B) Histogram of the GR curve from a neighboring well that the GR cuve in (A) will be normalized to using the base line shift method. (C) Resulting histogram of the GR curve from well in (A) after normaliztion.

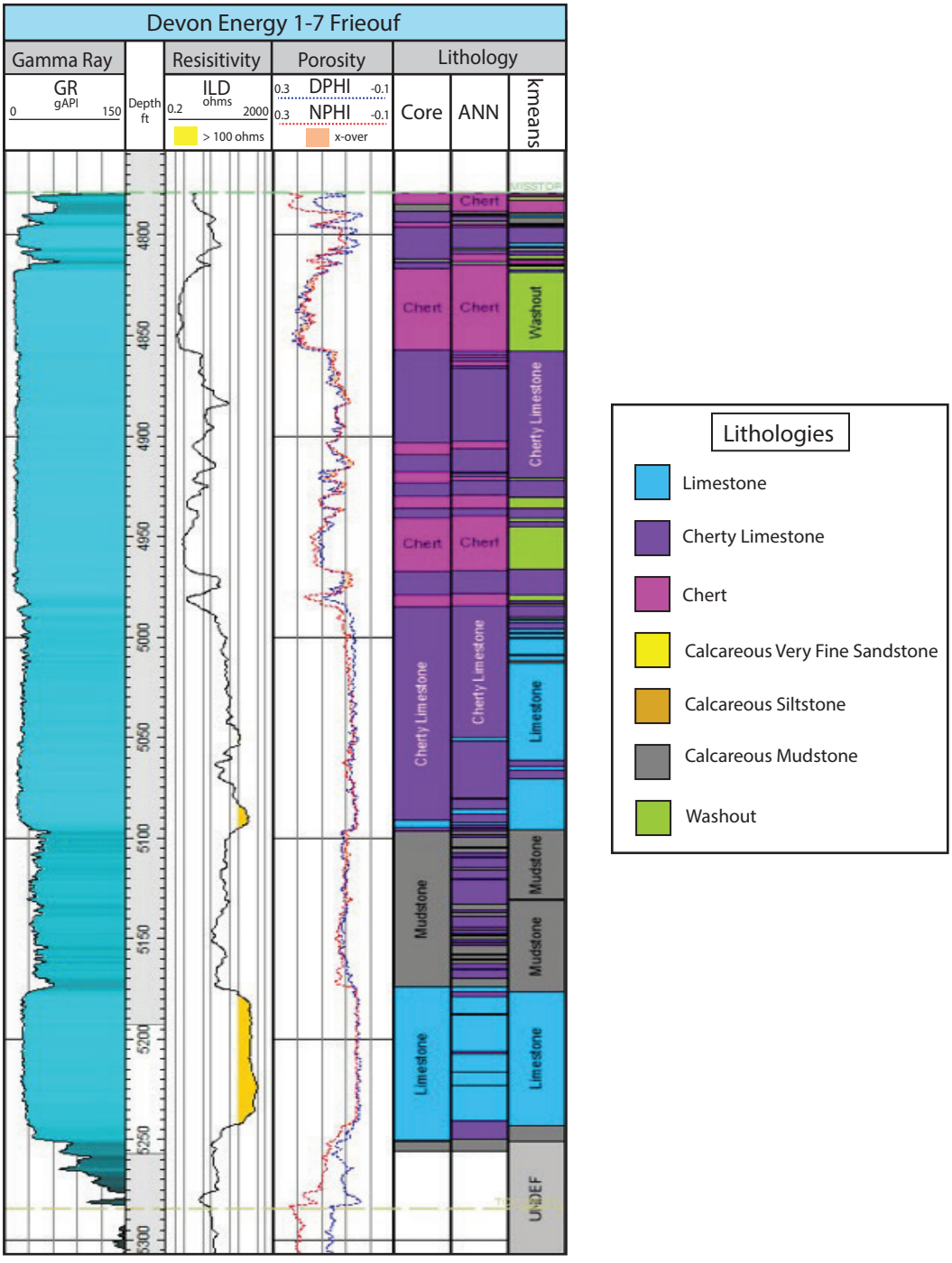

Appendix D-2: Well-log signatures through the Mississippian interval of interest for the Devon Energy 1-7 Frieouf with gamma ray. deep resisitivity, density porosity, and neutron porosity. The lithology tracks on the right illustrate the core-defined lithology, lithology estimated from ANN, and lithology estimated from k-means.

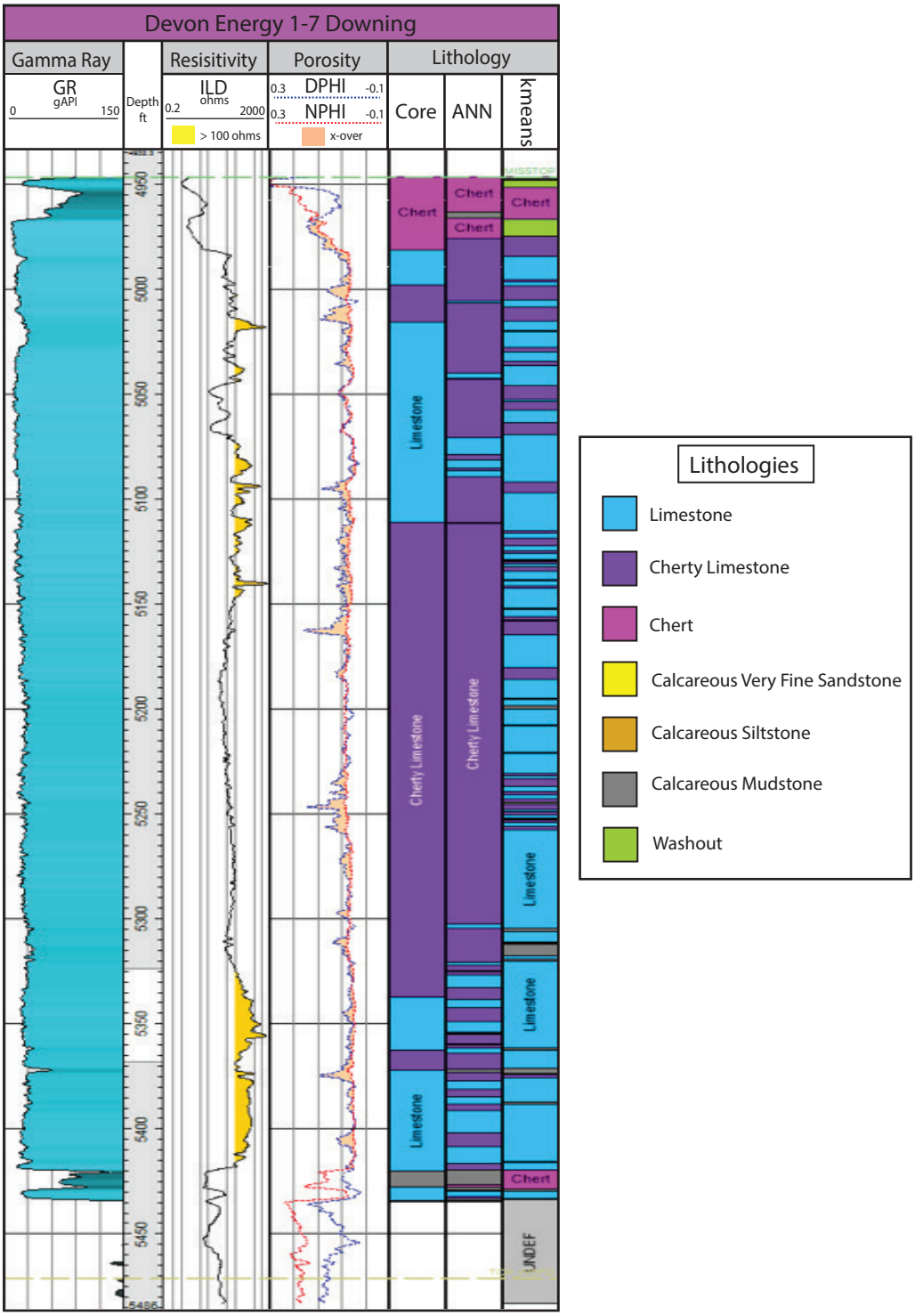

Appendix D-3: Well-log signatures through the Mississippian interval of interest for the Devon Energy 1-7 Downing with gamma ray. deep resisitivity, density porosity, and neutron porosity. The lithology tracks on the right illustrate the core-defined lithology, lithology estimated from ANN, and lithology estimated from k-means.

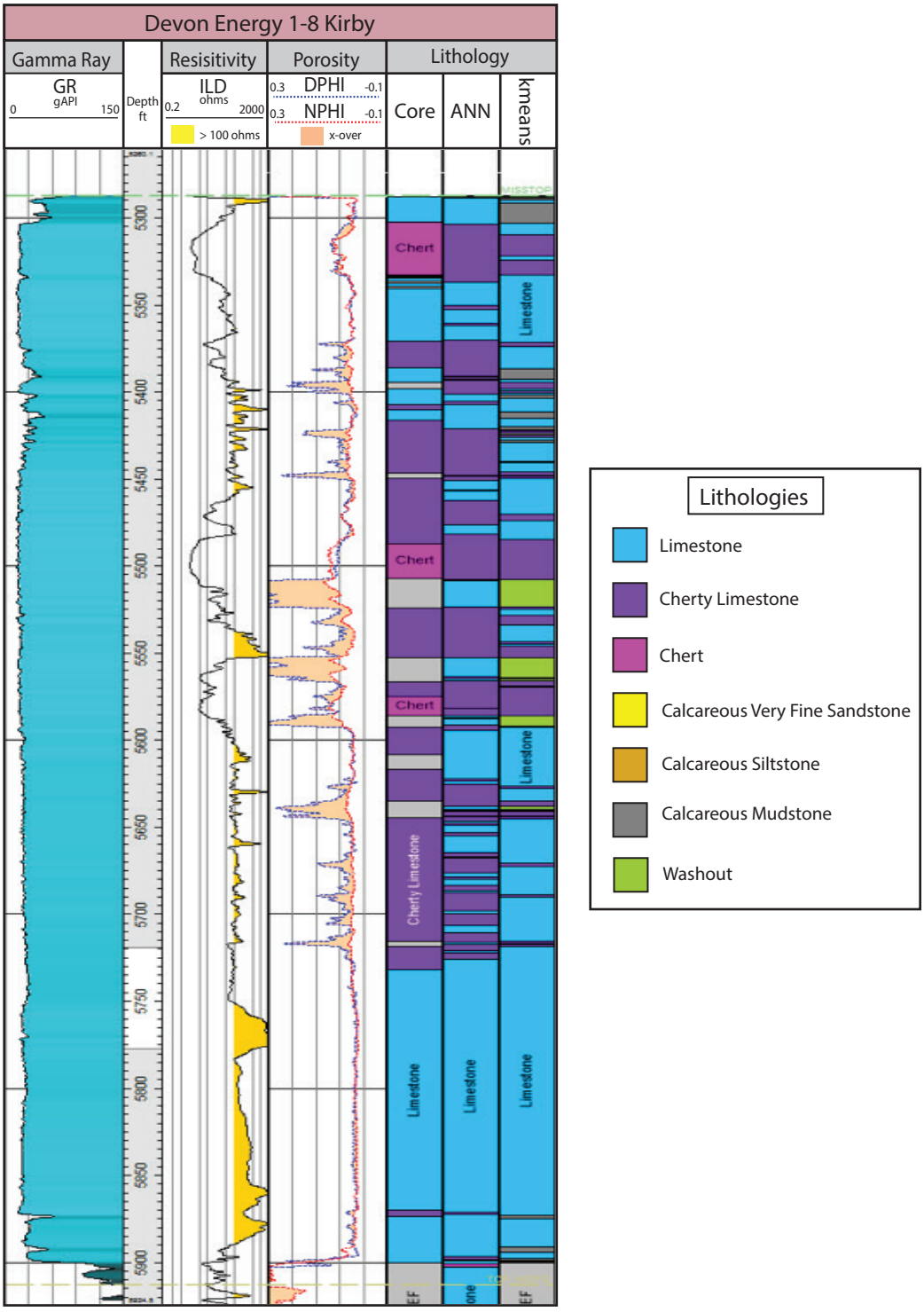

Appendix D-4: Well-log signatures through the Mississippian interval of interest for the Devon Energy 1-8 Kirby with gamma ray. deep resisitivity, density porosity, and neutron porosity. The lithology tracks on the right illustrate the core-defined lithology, lithology estimated from ANN, and lithology estimated from k-means.

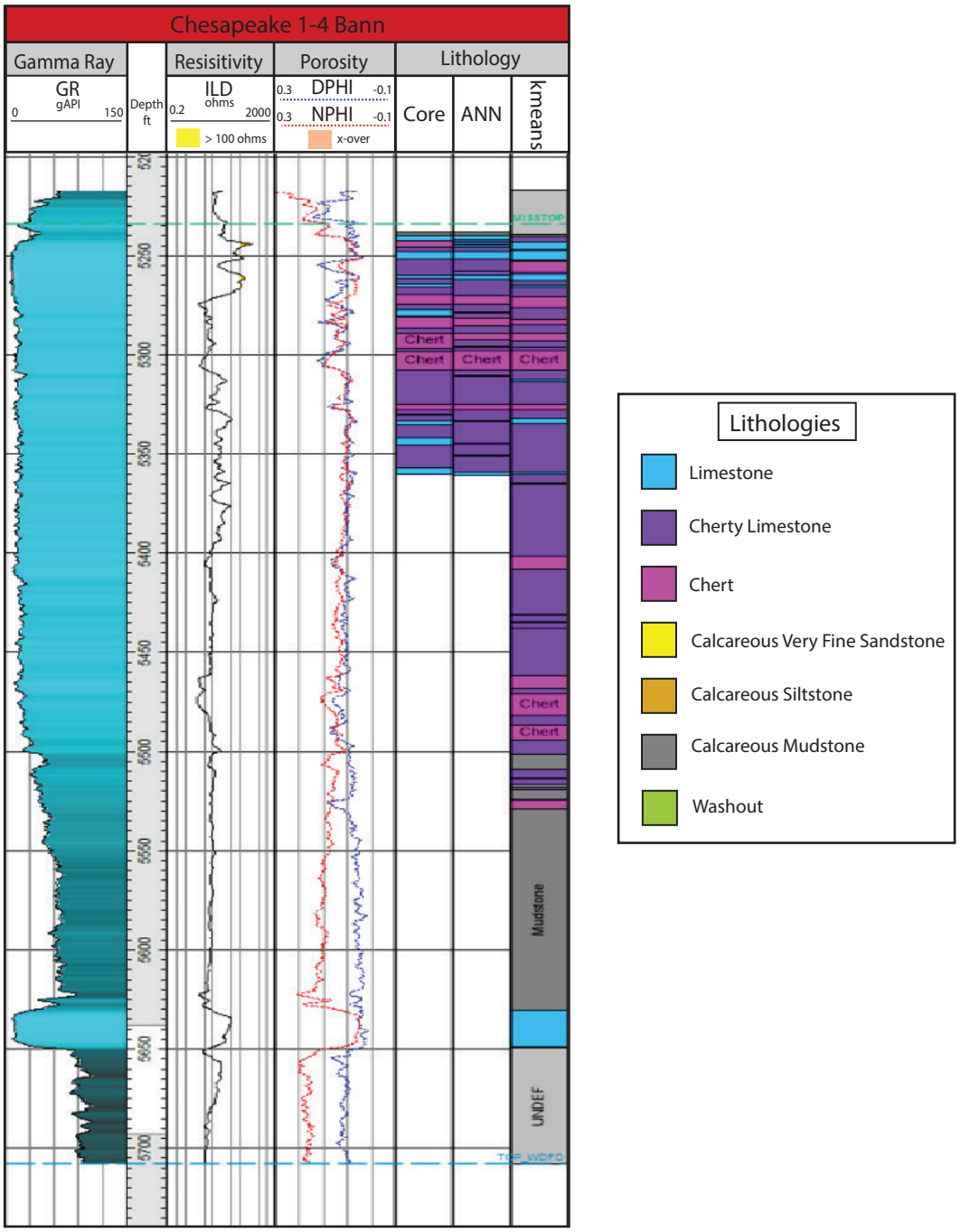

Appendix D-5: Well-log signatures through the Mississippian interval of interest for the Chesapeake 1-4 Bann with gamma ray. deep resisitivity, density porosity, and neutron porosity. The lithology tracks on the right illustrate the core-defined lithology, lithology estimated from ANN, and lithology estimated from k-means.

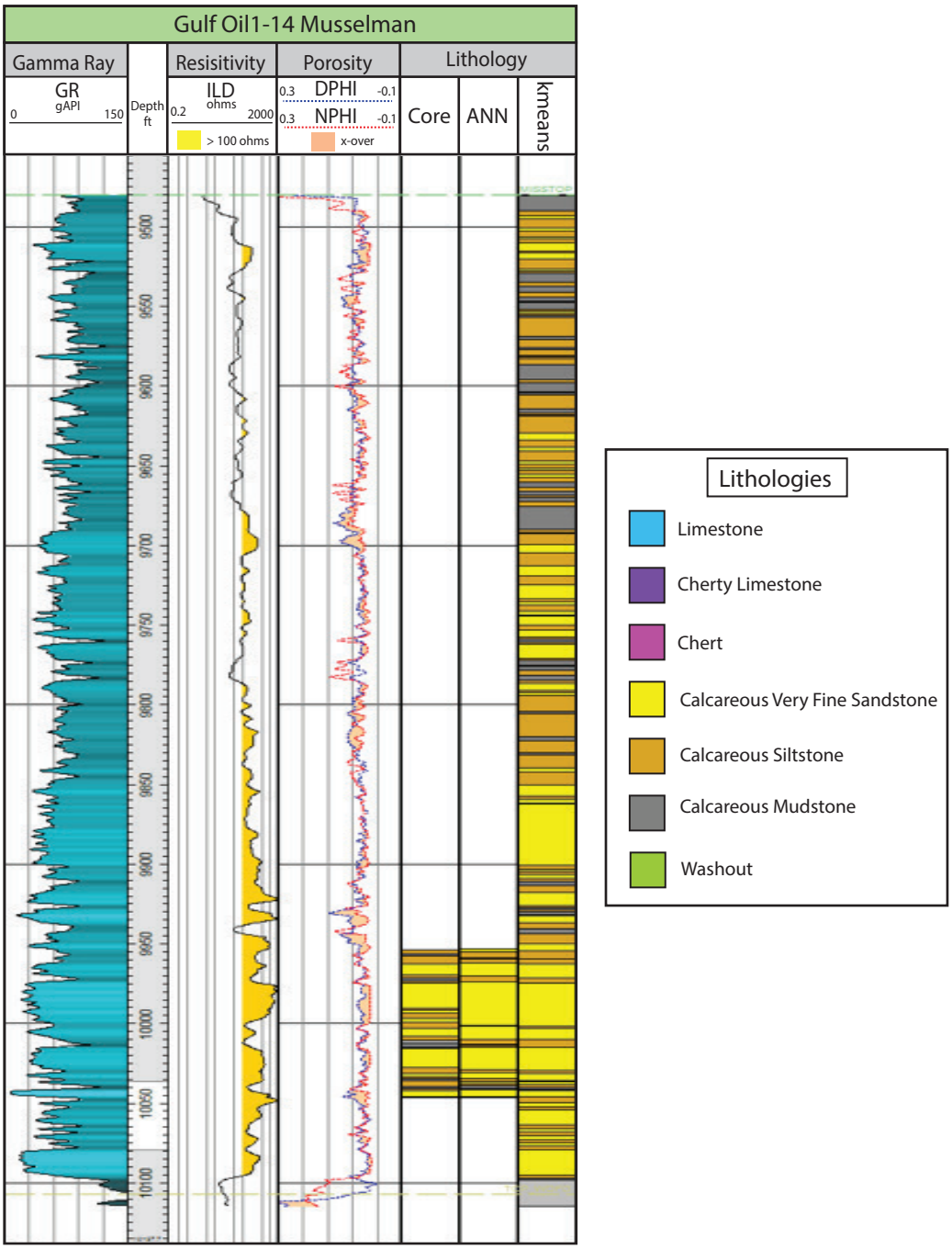

Appendix D-6: Well-log signatures through the Mississippian interval of interest for the Gulf Oil 1-14 Musselman with gamma ray. deep resisitivity, density porosity, and neutron porosity. The lithology tracks on the right illustrate the core-defined lithology, lithology estimated from ANN, and lithology estimated from k-means.

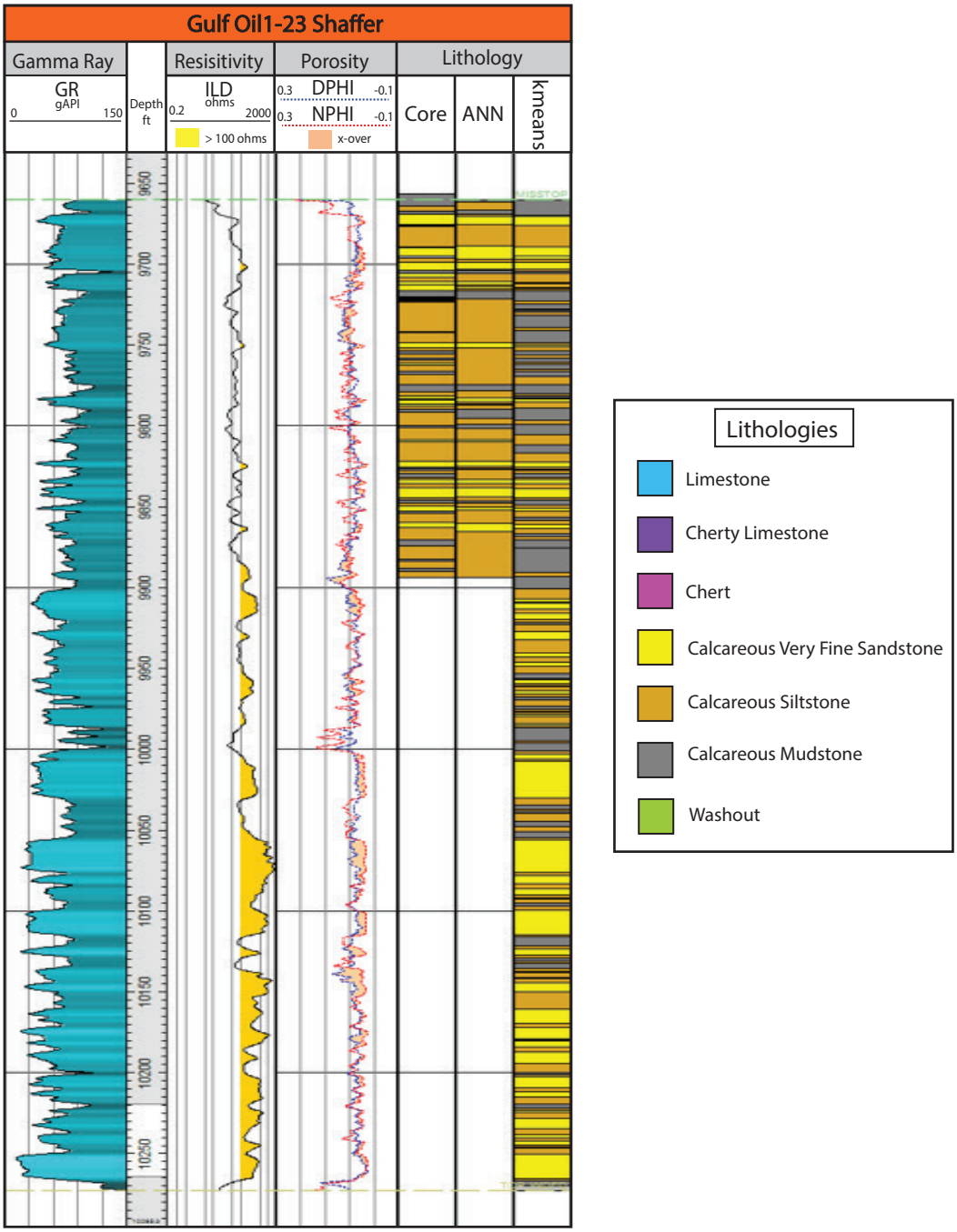

Appendix D-7: Well-log signatures through the Mississippian interval of interest for the Gulf Oil 1-23 Shaffer with gamma ray. deep resisitivity, density porosity, and neutron porosity. The lithology tracks on the right illustrate the core-defined lithology, lithology estimated from ANN, and lithology estimated from k-means.

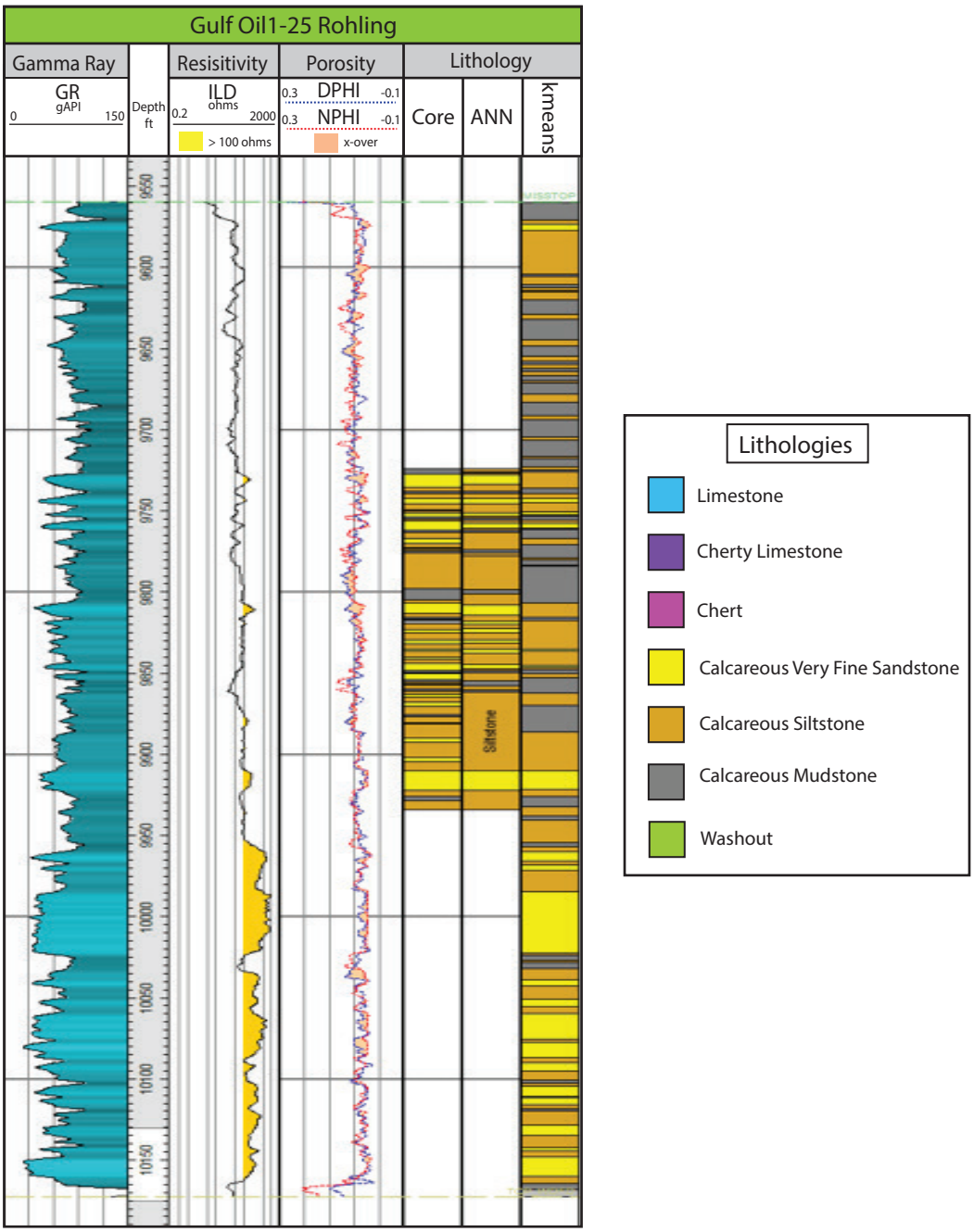

Appendix D-8: Well-log signatures through the Mississippian interval of interest for the Gulf Oil 1-25 Rohling with gamma ray. deep resisitivity, density porosity, and neutron porosity. The lithology tracks on the right illustrate the core-defined lithology, lithology estimated from ANN, and lithology estimated from k-means.

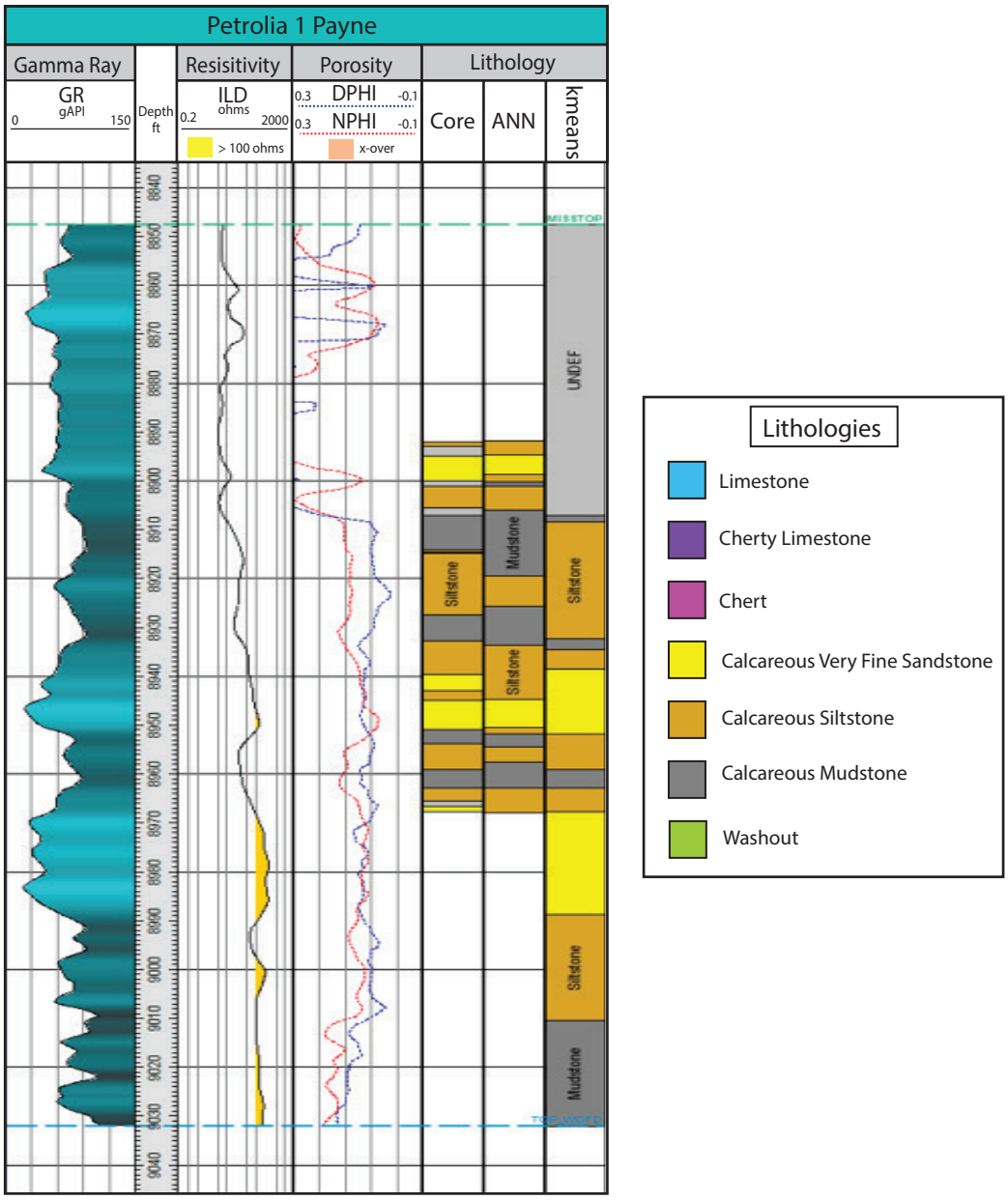

Appendix D-9: Well-log signatures through the Mississippian interval of interest for the Petrolia 1 Payne with gamma ray. deep resisitivity, density porosity, and neutron porosity. The lithology tracks on the right illustrate the core-defined lithology, lithology estimated from ANN, and lithology estimated from k-means.

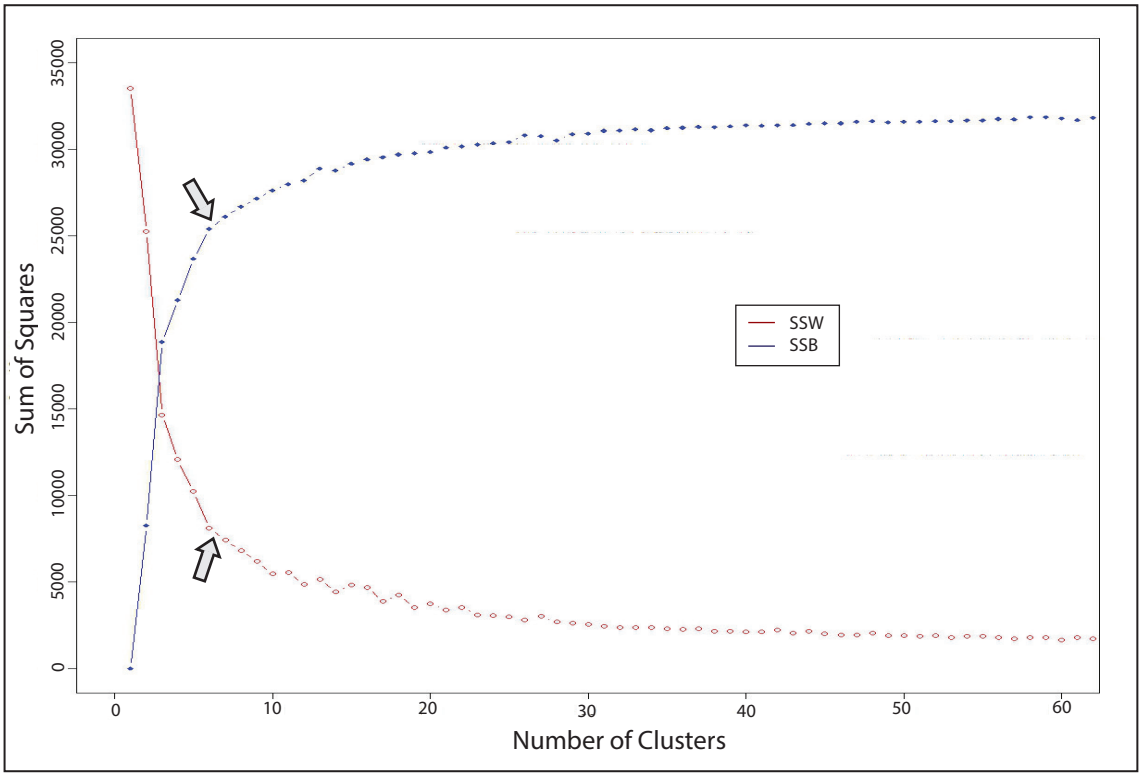

Appendix D-10: Plot of Sum-of-Squares Between (SSB) and Sum-of-Squares Within (SSW). SSW plot compares the cumulative distance of each data point to its centroid with increasing K values. The distance between the centroids and the data points decreases as more classes/lithologies are adding (increasing the K value). SSB plot compares cumulative distance of each centroid to the global centroid with increaing K values. The most favorable K value is picked at the infection point where the slope of the SSB and SSW plots decrease, known as the elbow point (arrows) (Wethington, 2017). The data used to create these plots were GR, DPHI, and NPHI logs and the optimum K value at the elbow point is 6.

A1

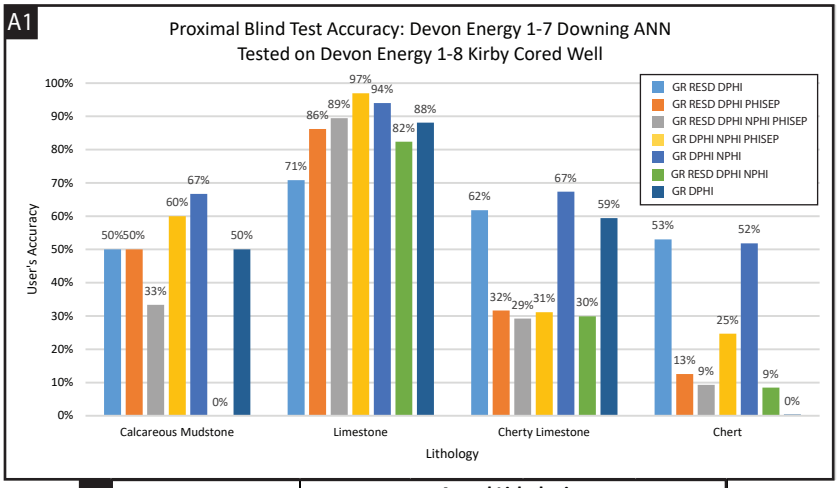

A2

Predicted Lithologies	Actual Lithologies			
	Calcareous Mudstone	Limestone	Cherty Limestone	Chert
Calcareous Mudstone	2	0	0	0
Limestone	1	892	322	24
Cherty Limestone	0	52	664	95
Chert	0	5	0	128
Accuarcy	67%	94%	67%	52%

B1

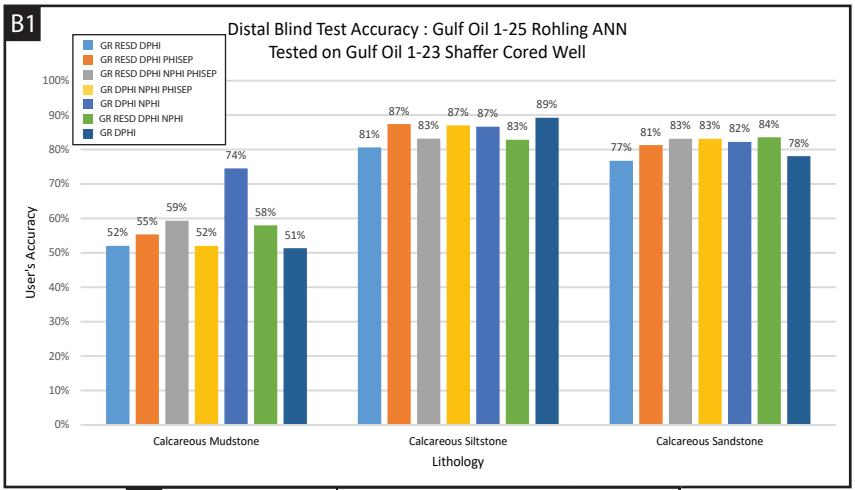

B2

Predicted Lithologies	Actual Lithologies		
	Calcareous Mudstone	Calcareous Siltstone	Calcareous Siltsone
Calcareous Mudstone	111	19	2
Calcareous Siltsone	30	474	37
Calcareous Sandstone	8	54	180
Accuarcy	74%	87%	82%

Appendix D-11: (A) Proximal blind test of the Devon Energy 1-7 Downing ANNs tested on the Devon Energy 1-8 Kirby cored well. (A1) Histogram compaing the user's accuarcy of prediting lithologies from each well log assemblage. ANN with the well log assemblage of GR, DPHI, and NPHI had the highest overall accuracy of prediciting each lithology (77%). (A2) Confusion matrix of the highest overall accuracy (77%) which shows common misclassification errors. (B) Distal blind test of the Gulf Oil 1-25 Rohling ANNs tested on the Gulf Oil 1-23 Shaffer cored well. (B1) Histogram compaing the user's accuarcy of prediting lithologies from each well log assemblage. ANN with the well log assemblage of GR, DPHI, and NPHI had the highest overall accuracy of prediciting each lithology (84%). (A2) Confusion matrix of the highest overall accuracy (84%) which shows common misclassification errors.

A1

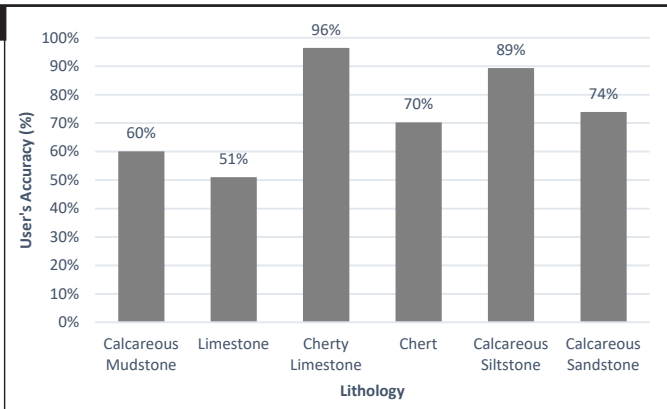

A2

Predicted Lithologies	Actual Lithology					
	Calcareous Mudstone	Limestone	Cherty Limestone	Chert	Calcareous Siltstone	Calcareous Sandstone
Calcareous Mudstone	220	3	0	0	45	2
Limestone	0	48	4	7	0	0
Cherty Limestone	0	41	243	34	0	0
Chert	0	2	5	97	0	0
Calcareous Siltstone	146	0	0	0	1153	191
Calcareous Sandstone	0	0	0	0	92	547
Accuracy	**60%**	**51%**	**96%**	**70%**	**89%**	**74%**

B1

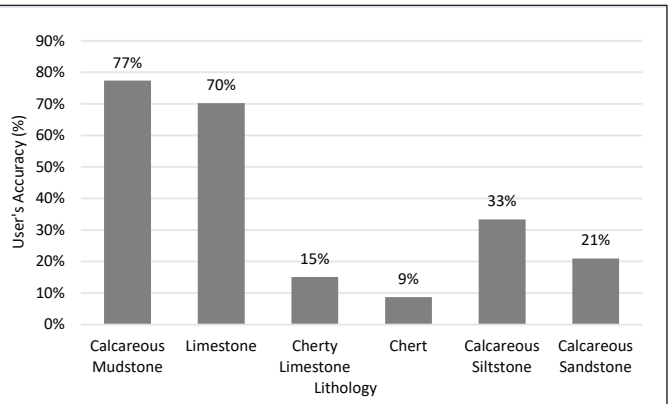

B2

Predicted Lithologies	Actual Lithology					
	Calcareous Mudstone	Limestone	Cherty Limestone	Chert	Calcareous Siltstone	Calcareous Sandstone
Calcareous Mudstone	280	1	0	0	815	133
Limestone	0	66	186	16	0	0
Cherty Limestone	0	0	38	110	0	0
Chert	0	27	28	12	0	0
Calcareous Siltstone	81	0	0	0	423	436
Calcareous Sandstone	1	0	0	0	30	151
Accuracy	**77%**	**70%**	**15%**	**9%**	**33%**	**21%**

Appendix D-12: (A1) Histogram of user's accuracy predicting each lithology using the ANN with well log inputs: GR, DPHI, and ILD from 5 cores in the dip-oriented (C-C') section. (A2) Confusion matrix of the ANN showing misclassifications and accuracies. (B1) Histogram of user's accuracy of a each lithology using k-means with the same well log inputs in the C-C' section. (B2) Confusion matrix from k-means.

A1

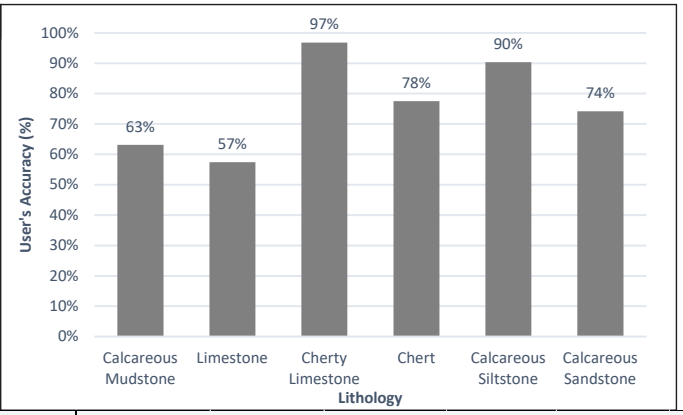

A2

Predicted Lithologies	Actual Lithology					
	Calcareous Mudstone	Limestone	Cherty Limestone	Chert	Calcareous Siltstone	Calcareous Sandstone
Calcareous Mudstone	231	0	0	0	45	2
Limestone	0	54	4	3	0	0
Cherty Limestone	0	40	244	28	0	0
Chert	0	0	4	107	0	0
Calcareous Siltstone	135	0	0	0	1165	189
Calcareous Sandstone	0	0	0	0	80	549
Accuracy	**63%**	**57%**	**97%**	**78%**	**90%**	**74%**

B1

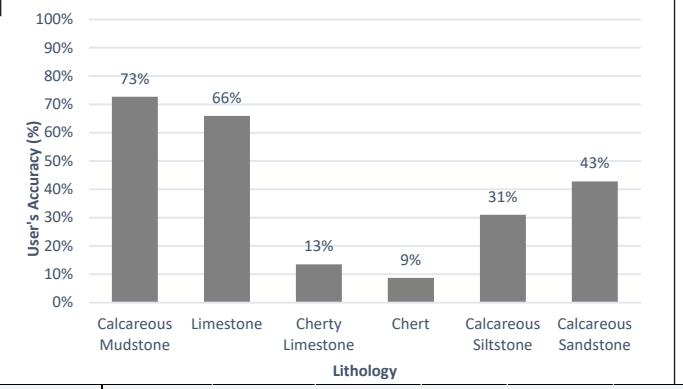

B2

Predicted Lithologies	Actual Lithology					
	Calcareous Mudstone	Limestone	Cherty Limestone	Chert	Calcareous Siltstone	Calcareous Sandstone
Calcareous Mudstone	263	3	0	0	766	136
Limestone	0	62	189	17	0	0
Cherty Limestone	0	0	34	109	0	0
Chert	0	29	29	12	0	0
Calcareous Siltstone	92	0	0	0	393	276
Calcareous Sandstone	7	0	0	0	109	308
Accuracy	**73%**	**66%**	**13%**	**9%**	**31%**	**43%**

Appendix D-13: (A1) Histogram of user's accuracy predicting each lithology using the ANN with well log inputs: GR, DPHI, ILD, and PHISEP from 5 cores in the dip-oriented (C-C') section. (A2) Confusion matrix of the ANN showing misclassifications and accuracies. (B1) Histogram of user's accuracy of a each lithology using k-means with the same well log inputs in the C-C' section. (B2) Confusion matrix from k-means.

A1

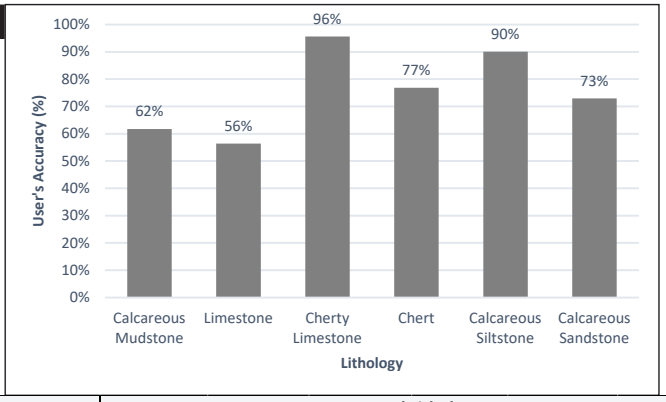

A2

Predicted Lithologies	Actual Lithology					
	Calcareous Mudstone	Limestone	Cherty Limestone	Chert	Calcareous Siltstone	Calcareous Sandstone
Calcareous Mudstone	226	0	0	0	43	1
Limestone	0	53	5	3	0	0
Cherty Limestone	0	41	241	29	0	0
Chert	0	0	6	106	0	0
Calcareous Siltstone	140	0	0	0	1162	199
Calcareous Sandstone	0	0	0	0	85	540
Accuracy	**62%**	**56%**	**96%**	**77%**	**90%**	**73%**

B1

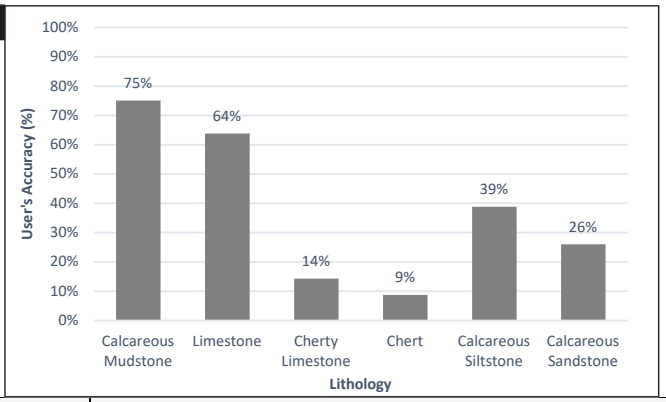

B2

Predicted Lithologies	Actual Lithology					
	Calcareous Mudstone	Limestone	Cherty Limestone	Chert	Calcareous Siltstone	Calcareous Sandstone
Calcareous Mudstone	272	3	0	0	733	76
Limestone	0	60	179	17	0	0
Cherty Limestone	0	0	36	109	0	0
Chert	0	31	37	12	0	0
Calcareous Siltstone	85	0	0	0	492	457
Calcareous Sandstone	5	0	0	0	43	187
Accuracy	**75%**	**64%**	**14%**	**9%**	**39%**	**26%**

Appendix D-14: (A1) Histogram of user's accuracy predicting each lithology using the ANN with well log inputs: GR, DPHI, NPHI, ILD, and PHISEP from 5 cores in the dip-oriented (C-C') section. (A2) Confusion matrix of the ANN showing misclassifications and accuracies. (B1) Histogram of user's accuracy of a each lithology using k-means with the same well log inputs in the C-C' section. (B2) Confusion matrix from k-means.

A1

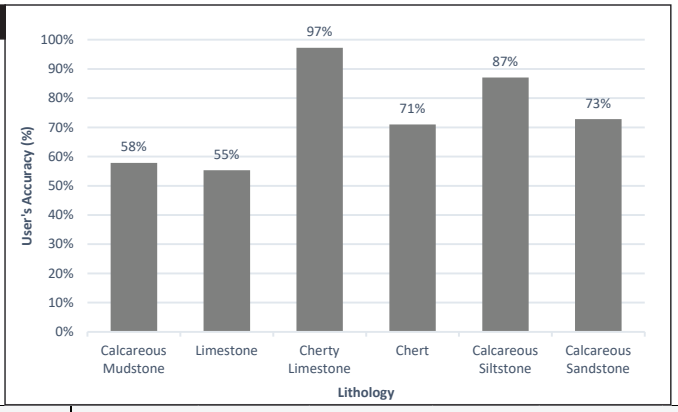

A2

Predicted Lithologies	Actual Lithology					
	Calcareous Mudstone	Limestone	Cherty Limestone	Chert	Calcareous Siltstone	Calcareous Sandstone
Calcareous Mudstone	211	0	0	0	66	2
Limestone	0	52	6	7	0	0
Cherty Limestone	0	42	245	33	0	0
Chert	0	0	1	98	0	0
Calcareous Siltstone	153	0	0	0	1123	199
Calcareous Sandstone	1	0	0	0	101	539
Accuracy	**58%**	**55%**	**97%**	**71%**	**87%**	**73%**

B1

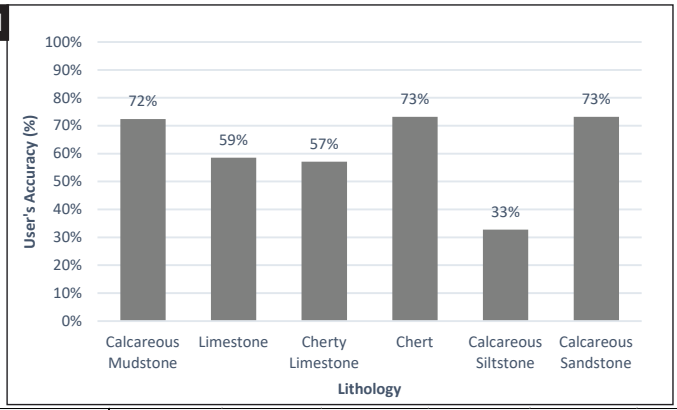

B2

Predicted Lithologies	Actual Lithology					
	Calcareous Mudstone	Limestone	Cherty Limestone	Chert	Calcareous Siltstone	Calcareous Sandstone
Calcareous Mudstone	262	3	0	0	567	92
Limestone	0	55	80	15	0	0
Cherty Limestone	0	36	144	22	0	0
Chert	0	0	28	101	0	0
Calcareous Siltstone	80	0	0	0	415	103
Calcareous Sandstone	20	0	0	0	286	532
Accuracy	**72%**	**59%**	**57%**	**73%**	**33%**	**73%**

Appendix D-15: (A1) Histogram of user's accuracy predicting each lithology using the ANN with well log inputs: GR, DPHI, NPHI, and PHISEP from 5 cores in the dip-oriented (C-C') section. (A2) Confusion matrix of the ANN showing misclassifications and accuracies. (B1) Histogram of user's accuracy of a each lithology using k-means with the same well log inputs in the C-C' section. (B2) Confusion matrix from k-means.

A1

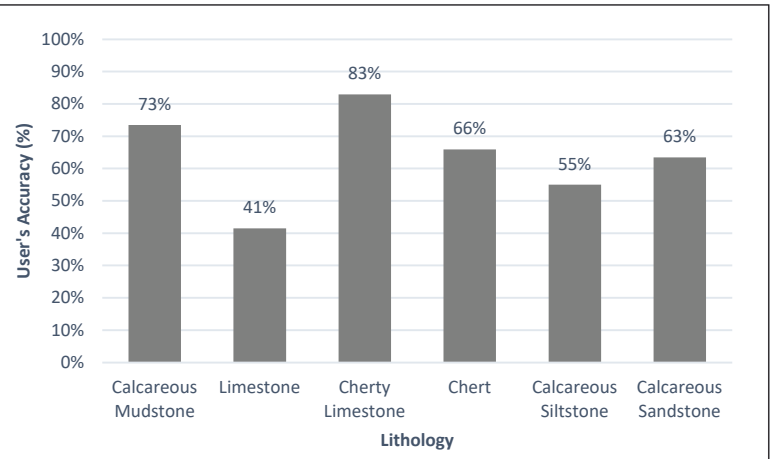

A2

Predicted Lithologies	Actual Lithology					
	Calcareous Mudstone	Limestone	Cherty Limestone	Chert	Calcareous Siltstone	Calcareous Sandstone
Calcareous Mudstone	266	3	0	0	480	25
Limestone	0	39	17	12	0	0
Cherty Limestone	0	52	209	35	0	0
Chert	0	0	26	91	0	0
Calcareous Siltstone	89	0	0	0	698	238
Calcareous Sandstone	7	0	0	0	90	457
Accuracy	**73%**	**41%**	**83%**	**66%**	**55%**	**63%**

Appendix D-16: (A1) Histogram of user's accuracy predicting each lithology using k-means with well log inputs: GR, DPHI, and NPHI from 5 cores in the dip-oriented (C-C') section. (A2) Confusion matrix of k-means showing misclassifications and accuracies.

A1

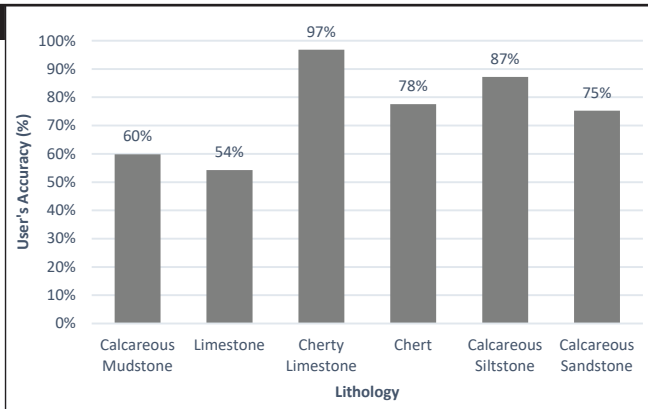

A2

Predicted Lithologies	Actual Lithology					
	Calcareous Mudstone	Limestone	Cherty Limestone	Chert	Calcareous Siltstone	Calcareous Sandstone
Calcareous Mudstone	219	0	0	0	72	2
Limestone	0	51	4	3	0	0
Cherty Limestone	0	43	244	28	0	0
Chert	0	0	4	107	0	0
Calcareous Siltstone	147	0	0	0	1125	181
Calcareous Sandstone	0	0	0	0	93	557
Accuracy	**60%**	**54%**	**97%**	**78%**	**87%**	**75%**

B1

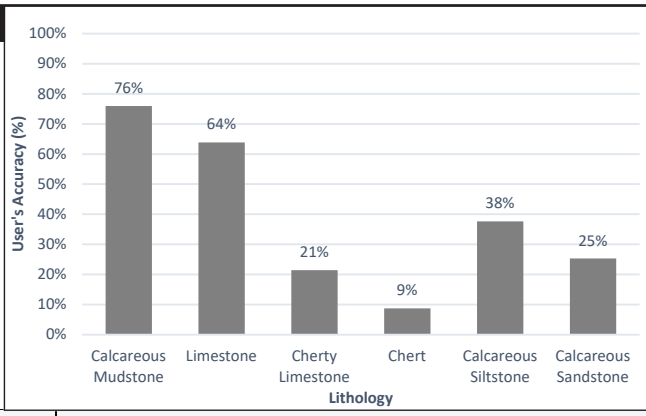

B2

Predicted Lithologies	Actual Lithology					
	Calcareous Mudstone	Limestone	Cherty Limestone	Chert	Calcareous Siltstone	Calcareous Sandstone
Calcareous Mudstone	275	2	0	0	753	87
Limestone	0	60	169	18	0	0
Cherty Limestone	0	3	54	108	0	0
Chert	0	29	29	12	0	0
Calcareous Siltstone	84	0	0	0	477	451
Calcareous Sandstone	3	0	0	0	38	182
Accuracy	**76%**	**64%**	**21%**	**9%**	**38%**	**25%**

Appendix D-17: (A1) Histogram of user's accuracy predicting each lithology using the ANN with well log inputs: GR, DPHI, NPHI, and ILD from 5 cores in the dip-oriented (C-C') section. (A2) Confusion matrix of the ANN showing misclassifications and accuracies. (B1) Histogram of user's accuracy of a each lithology using k-means with the same well log inputs in the C-C' section. (B2) Confusion matrix from k-means.

A1

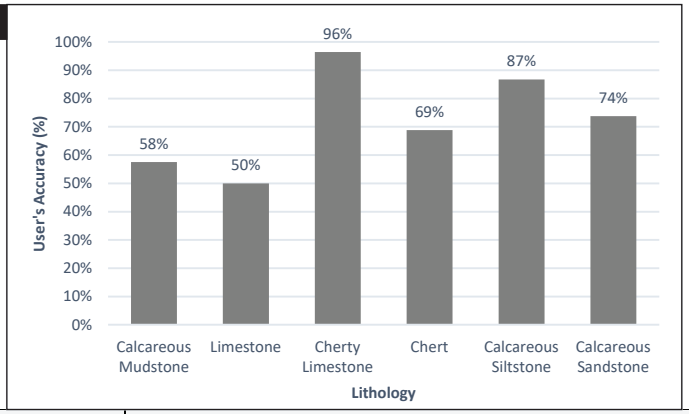

A2

Predicted Lithologies	Actual Lithology					
	Calcareous Mudstone	Limestone	Cherty Limestone	Chert	Calcareous Siltstone	Calcareous Sandstone
Calcareous Mudstone	210	0	0	0	72	2
Limestone	0	47	7	9	0	0
Cherty Limestone	0	47	243	34	0	0
Chert	0	0	2	95	0	0
Calcareous Siltstone	155	0	0	0	1119	192
Calcareous Sandstone	0	0	0	0	99	546
Accuracy	**58%**	**50%**	**96%**	**69%**	**87%**	**74%**

B1

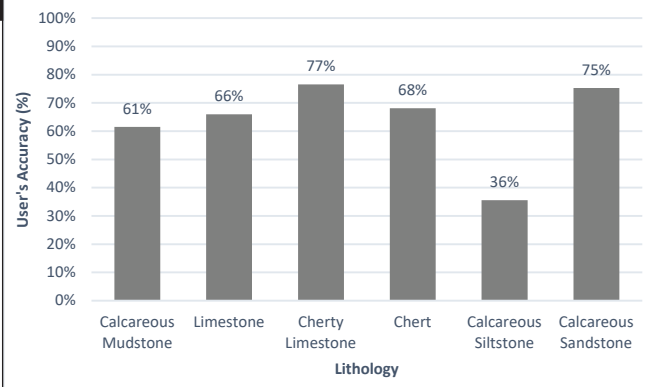

B2

Predicted Lithologies	Actual Lithology					
	Calcareous Mudstone	Limestone	Cherty Limestone	Chert	Calcareous Siltstone	Calcareous Sandstone
Calcareous Mudstone	222	0	0	0	656	100
Limestone	0	62	34	12	0	0
Cherty Limestone	0	32	193	32	0	0
Chert	0	0	25	94	0	0
Calcareous Siltstone	136	0	0	0	451	78
Calcareous Sandstone	3	0	0	0	161	542
Accuracy	**61%**	**66%**	**77%**	**68%**	**36%**	**75%**

Appendix D-18: (A1) Histogram of user's accuracy predicting each lithology using the ANN with well log inputs: GR and DPHI from 5 cores in the dip-oriented (C-C') section. (A2) Confusion matrix of the ANN showing misclassifications and accuracies. (B1) Histogram of user's accuracy of a each lithology using k-means with the same well log inputs in the C-C' section. (B2) Confusion matrix from k-means.

A1

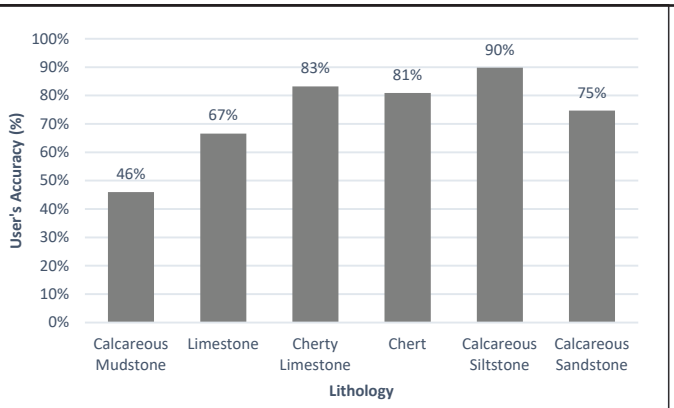

A2

Predicted Lithologies	Actual Lithology					
	Calcareous Mudstone	Limestone	Cherty Limestone	Chert	Calcareous Siltstone	Calcareous Sandstone
Calcareous Mudstone	308	26	17	46	26	1
Limestone	2	1353	374	0	0	0
Cherty Limestone	202	653	2367	103	0	0
Chert	17	0	87	630	0	0
Calcareous Siltstone	141	0	0	0	1032	170
Calcareous Sandstone	0	0	0	0	91	504
Accuracy	**46%**	**67%**	**83%**	**81%**	**90%**	**75%**

B1

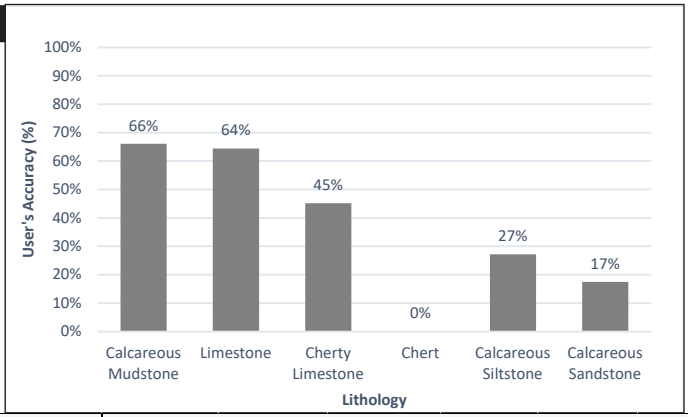

B2

Predicted Lithologies	Actual Lithology					
	Calcareous Mudstone	Limestone	Cherty Limestone	Chert	Calcareous Siltstone	Calcareous Sandstone
Calcareous Mudstone	428	87	18	80	815	133
Limestone	210	1303	1499	18	0	0
Cherty Limestone	0	489	1274	485	0	0
Chert	0	144	30	0	0	0
Calcareous Siltstone	10	0	0	0	312	424
Calcareous Sandstone	0	0	0	0	22	118
Accuracy	**66%**	**64%**	**45%**	**0%**	**27%**	**17%**

Appendix D-19: (A1) Histogram of user's accuracy predicting each lithology using the ANN with well log inputs: GR, DPHI, and ILD from 6 cores in the oblique-oriented (D-D') section. (A2) Confusion matrix of the ANN showing misclassifications and accuracies. (B1) Histogram of user's accuracy of a each lithology using k-means with the same well log inputs in the D-D' section. (B2) Confusion matrix from k-means.

A1

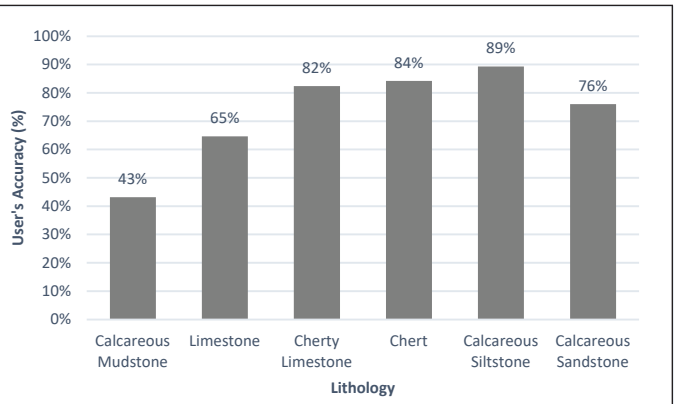

A2

Predicted Lithologies	Actual Lithology					
	Calcareous Mudstone	Limestone	Cherty Limestone	Chert	Calcareous Siltstone	Calcareous Sandstone
Calcareous Mudstone	289	26	20	27	31	1
Limestone	1	1313	400	1	0	0
Cherty Limestone	224	689	2345	95	0	0
Chert	26	4	80	656	0	0
Calcareous Siltstone	130	0	0	0	1026	161
Calcareous Sandstone	0	0	0	0	92	513
Accuracy	**43%**	**65%**	**82%**	**84%**	**89%**	**76%**

B1

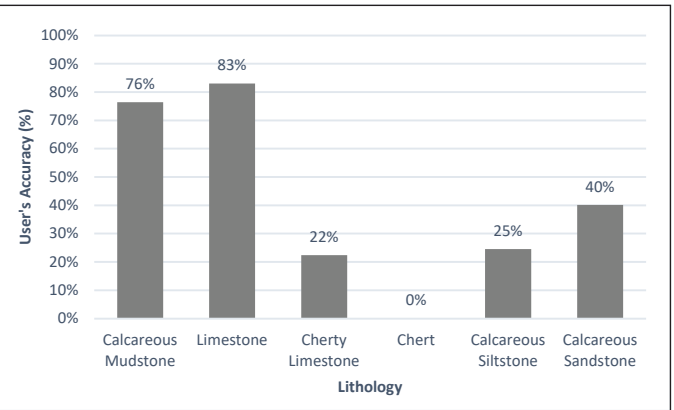

B2

Predicted Lithologies	Actual Lithology					
	Calcareous Mudstone	Limestone	Cherty Limestone	Chert	Calcareous Siltstone	Calcareous Sandstone
Calcareous Mudstone	495	115	24	90	766	136
Limestone	125	1684	2153	165	0	0
Cherty Limestone	0	80	636	517	0	0
Chert	0	149	30	0	0	0
Calcareous Siltstone	24	0	0	0	282	268
Calcareous Sandstone	4	0	0	0	101	271
Accuracy	**76%**	**83%**	**22%**	**0%**	**25%**	**40%**

Appendix D-20: (A1) Histogram of user's accuracy predicting each lithology using the ANN with well log inputs: GR, DPHI, ILD and PHISEP from 6 cores in the oblique-oriented (D-D') section. (A2) Confusion matrix of the ANN showing misclassifications and accuracies. (B1) Histogram of user's accuracy of a each lithology using k-means with the same well log inputs in the D-D' section. (B2) Confusion matrix from k-means.

A1

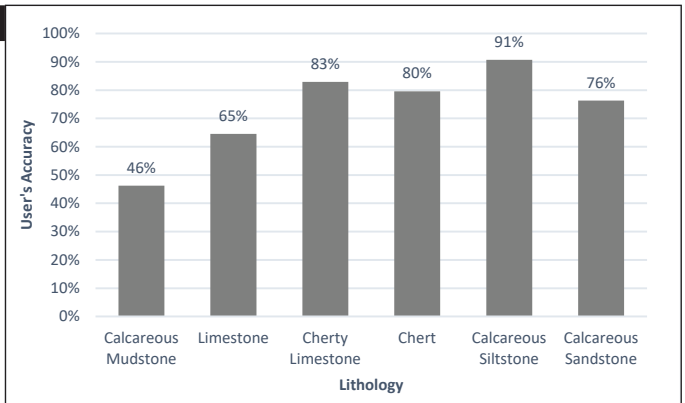

A2

Predicted Lithologies	Actual Lithology					
	Calcareous Mudstone	Limestone	Cherty Limestone	Chert	Calcareous Siltstone	Calcareous Sandstone
Calcareous Mudstone	310	25	22	45	23	0
Limestone	0	1311	364	3	0	0
Cherty Limestone	197	692	2360	111	0	0
Chert	28	4	99	620	0	0
Calcareous Siltstone	135	0	0	0	1042	160
Calcareous Sandstone	0	0	0	0	84	515
Accuracy	**46%**	**65%**	**83%**	**80%**	**91%**	**76%**

B1

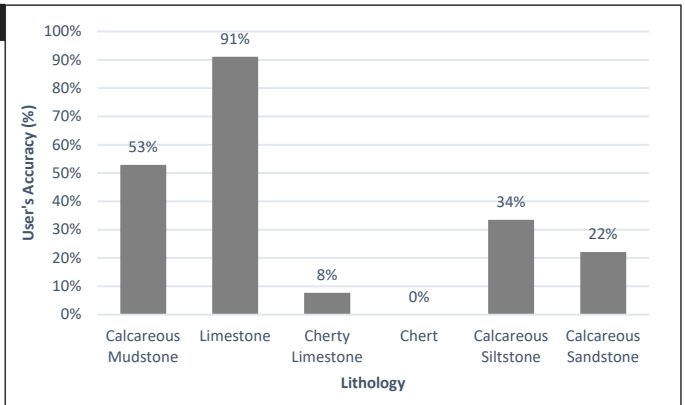

B2

Predicted Lithologies	Actual Lithology					
	Calcareous Mudstone	Limestone	Cherty Limestone	Chert	Calcareous Siltstone	Calcareous Sandstone
Calcareous Mudstone	343	21	13	86	733	76
Limestone	285	1844	2558	143	0	0
Cherty Limestone	1	6	218	543	0	0
Chert	0	154	33	0	0	0
Calcareous Siltstone	19	0	0	0	385	450
Calcareous Sandstone	0	0	0	0	31	149
Accuracy	**53%**	**91%**	**8%**	**0%**	**34%**	**22%**

Appendix D-21: (A1) Histogram of user's accuracy predicting each lithology using the ANN with well log inputs: GR, DPHI, NPHI, ILD and PHISEP from 6 cores in the oblique-oriented (D-D') section. (A2) Confusion matrix of the ANN showing misclassifications and accuracies. (B1) Histogram of user's accuracy of a each lithology using k-means with the same well log inputs in the D-D' section. (B2) Confusion matrix from k-means.

A1

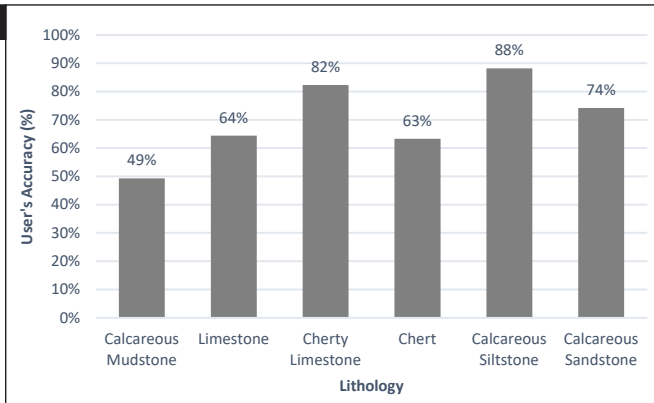

A2

Predicted Lithologies	Actual Lithology					
	Calcareous Mudstone	Limestone	Cherty Limestone	Chert	Calcareous Siltstone	Calcareous Sandstone
Calcareous Mudstone	330	22	23	16	35	1
Limestone	4	1309	392	4	0	0
Cherty Limestone	161	701	2342	266	0	0
Chert	25	0	88	493	0	0
Calcareous Siltstone	149	0	0	0	1013	173
Calcareous Sandstone	1	0	0	0	101	501
Accuracy	**49%**	**64%**	**82%**	**63%**	**88%**	**74%**

B1

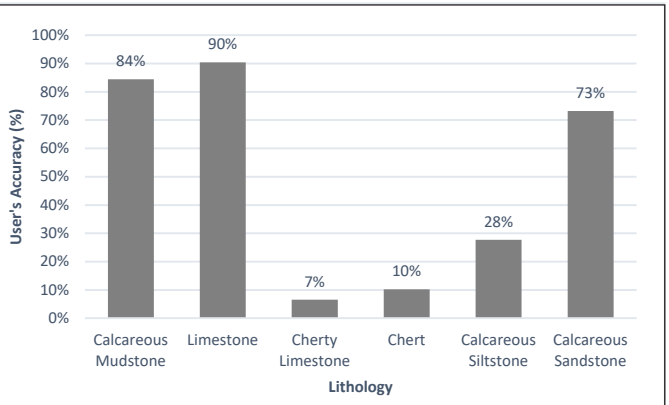

B2

Predicted Lithologies	Actual Lithology					
	Calcareous Mudstone	Limestone	Cherty Limestone	Chert	Calcareous Siltstone	Calcareous Sandstone
Calcareous Mudstone	547	182	141	11	559	85
Limestone	5	1830	2491	182	0	0
Cherty Limestone	1	5	184	500	0	0
Chert	51	8	5	79	0	0
Calcareous Siltstone	30	0	0	0	318	96
Calcareous Sandstone	14	0	0	0	272	494
Accuracy	**84%**	**90%**	**7%**	**10%**	**28%**	**73%**

Appendix D-22: (A1) Histogram of user's accuracy predicting each lithology using the ANN with well log inputs: GR, DPHI, NPHI, and PHISEP from 6 cores in the oblique-oriented (D-D') section. (A2) Confusion matrix of the ANN showing misclassifications and accuracies. (B1) Histogram of user's accuracy of a each lithology using k-means with the same well log inputs in the D-D' section. (B2) Confusion matrix from k-means.

A1

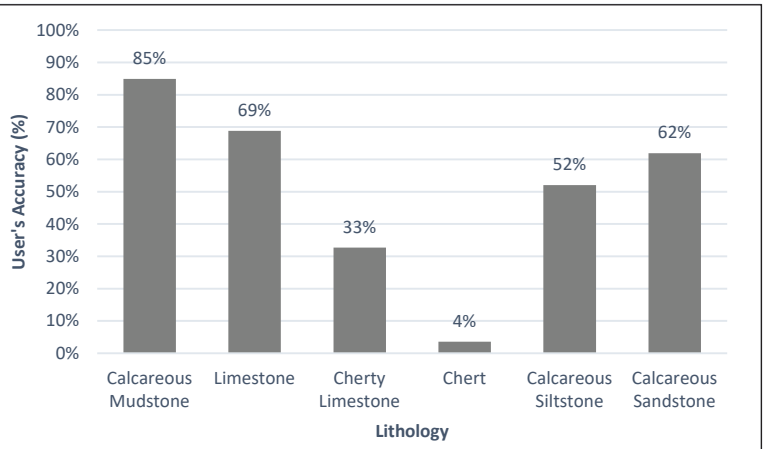

A2

Predicted Lithologies	Actual Lithology					
	Calcareous Mudstone	Limestone	Cherty Limestone	Chert	Calcareous Siltstone	Calcareous Sandstone
Calcareous Mudstone	550	38	40	8	473	25
Limestone	4	413	742	233	0	0
Cherty Limestone	31	8	417	135	0	0
Chert	20	141	77	14	0	0
Calcareous Siltstone	39	0	0	0	598	232
Calcareous Sandstone	4	0	0	0	78	418
Accuracy	**85%**	**69%**	**33%**	**4%**	**52%**	**62%**

Appendix D-23: (A1) Histogram of user's accuracy predicting each lithology using k-means with well log inputs: GR, DPHI, and NPHI from 6 cores in the oblique-oriented (D-D') section. (A2) Confusion matrix of k-means showing misclassifications and accuracies.

A1

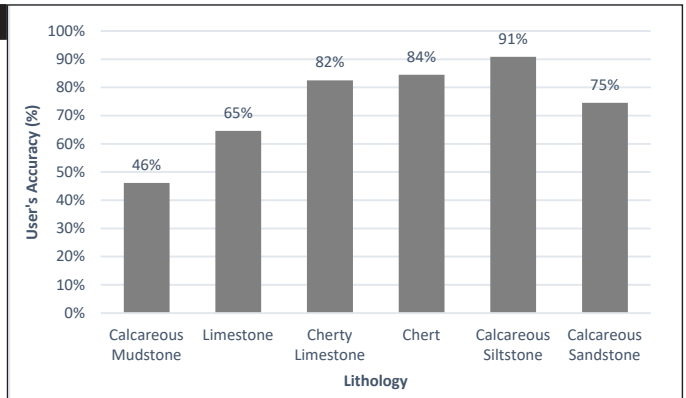

A2

Predicted Lithologies	Actual Lithology					
	Calcareous Mudstone	Limestone	Cherty Limestone	Chert	Calcareous Siltstone	Calcareous Sandstone
Calcareous Mudstone	309	30	33	31	19	1
Limestone	0	1312	359	1	0	0
Cherty Limestone	195	687	2347	89	0	0
Chert	24	3	106	658	0	0
Calcareous Siltstone	142	0	0	0	1044	171
Calcareous Sandstone	0	0	0	0	86	503
Accuracy	**46%**	**65%**	**82%**	**84%**	**91%**	**75%**

B1

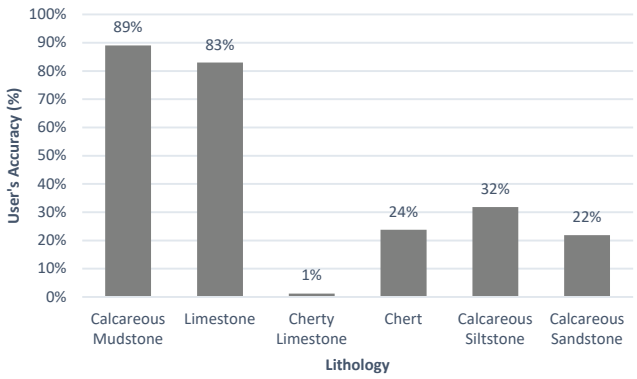

B2

Predicted Lithologies	Actual Lithology					
	Calcareous Mudstone	Limestone	Cherty Limestone	Chert	Calcareous Siltstone	Calcareous Sandstone
Calcareous Mudstone	576	183	141	12	753	87
Limestone	4	1680	2503	231	0	0
Cherty Limestone	0	152	33	0	0	0
Chert	51	10	5	76	0	0
Calcareous Siltstone	16	0	0	0	366	440
Calcareous Sandstone	0	0	0	0	30	148
Accuracy	**89%**	**83%**	**1%**	**24%**	**32%**	**22%**

Appendix D-24: (A1) Histogram of user's accuracy predicting each lithology using the ANN with well log inputs: GR, DPHI, NPHI, and ILD from 6 cores in the oblique-oriented (D-D') section. (A2) Confusion matrix of the ANN showing misclassifications and accuracies. (B1) Histogram of user's accuracy of a each lithology using k-means with the same well log inputs in the D-D' section. (B2) Confusion matrix from k-means.

A1

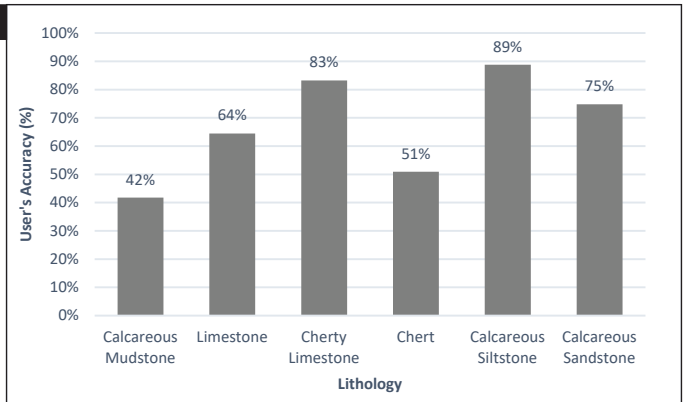

A2

Predicted Lithologies	Actual Lithology					
	Calcareous Mudstone	Limestone	Cherty Limestone	Chert	Calcareous Siltstone	Calcareous Sandstone
Calcareous Mudstone	280	18	15	67	31	1
Limestone	3	1310	406	5	0	0
Cherty Limestone	234	694	2367	310	0	0
Chert	3	10	57	397	0	0
Calcareous Siltstone	150	0	0	0	1020	169
Calcareous Sandstone	0	0	0	0	98	505
Accuracy	**42%**	**64%**	**83%**	**51%**	**89%**	**75%**

B1

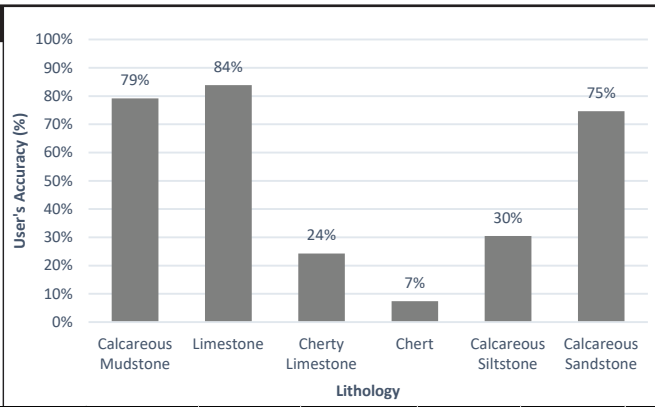

B2

Predicted Lithologies	Actual Lithology					
	Calcareous Mudstone	Limestone	Cherty Limestone	Chert	Calcareous Siltstone	Calcareous Sandstone
Calcareous Mudstone	513	212	110	44	650	100
Limestone	6	1699	2035	54	0	0
Cherty Limestone	0	103	691	502	0	0
Chert	55	12	6	48	0	0
Calcareous Siltstone	72	0	0	0	350	71
Calcareous Sandstone	2	0	0	0	149	504
Accuracy	**79%**	**84%**	**24%**	**7%**	**30%**	**75%**

Appendix D-25: (A1) Histogram of user's accuracy predicting each lithology using the ANN with well log inputs: GR and DPHI from 6 cores in the oblique-oriented (D-D') section. (A2) Confusion matrix of the ANN showing misclassifications and accuracies. (B1) Histogram of user's accuracy of a each lithology using k-means with the same well log inputs in the D-D' section. (B2) Confusion matrix from k-means.

Appendix D-26: Electrofacies Classification Limitations

Like with any modeling approaches, there are some limitations and drawbacks with electrofacies classification techniques. Since each technique did not reach 100% prediction accuracy, the main issue for each technique is misclassification. However, the principle motivation is to reduce the misclassifications in each techniques to achieve satisfactory accuracies. Core coverage is a drawback to classification techniques and can impact the predictability of each lithology. If the cores do not cover the entire interval of section and represent the full spectrum of lithologies present, then the electrofacies classification model will also not be able to predict those lithologies. In this study, cores from past studies were incorporated to capture the lithologies present across the study area (Haynes, 2013; Birch, 2015; Lindzey 2015; Flinton, 2016; Suriamin and Pranter, 2018). Another limitation is the resolution of the well logs used as inputs in the models. Generally, well logs resolution is not detailed enough to identify the fine scale lithofacies. Accordingly, lithofacies were grouped into their parent lithologies to increase the prediction accuracy. Older logging tools with limited technology lead to miscalibrations and lower resolutions also affected the results of electrofacies classifications. Therefore, modern, more advanced logs could lead to higher overall accuracies of each lithology because of their ability to differentiate pore sizes and finer detailed characteristics of each lithology.

Dip-oriented Lithology Model					
Formation/Zone	Lithology	Major Hozizontal Range (ft)	Minor Hozizontal Range (ft)	Vertical Range (ft)	Lithology (%)
Meramec 7	Calcareous Mudstone	20000	20000	3.5	61.36
	Limestone	20000	20000	3.5	0
	Cherty Limestone	20000	20000	3.5	0
	Chert	20000	20000	3.5	0
	Calcareous Siltstone	20000	20000	3.5	36.51
	Calcareous Sandstone	20000	20000	3.5	2.13
	Shale	20000	20000	3.5	0
Meramec 6	Calcareous Mudstone	20000	20000	2.2	60.13
	Limestone	20000	20000	2.2	0.48
	Cherty Limestone	20000	20000	2.2	0.58
	Chert	20000	20000	2.2	0
	Calcareous Siltstone	20000	20000	2.2	36.95
	Calcareous Sandstone	20000	20000	2.2	2.86
	Shale	20000	20000	2.2	0
Meramec 5	Calcareous Mudstone	20000	20000	3.6	19.93
	Limestone	20000	20000	3.6	0
	Cherty Limestone	20000	20000	3.6	0
	Chert	20000	20000	3.6	0
	Calcareous Siltstone	20000	20000	3.6	64.43
	Calcareous Sandstone	20000	20000	3.6	15.65
	Shale	20000	20000	3.6	0
Meramec 4	Calcareous Mudstone	20000	20000	3.4	39.63
	Limestone	20000	20000	3.4	0.25
	Cherty Limestone	20000	20000	3.4	0
	Chert	20000	20000	3.4	0.2
	Calcareous Siltstone	20000	20000	3.4	52.84
	Calcareous Sandstone	20000	20000	3.4	7.27
	Shale	20000	20000	3.4	0
Meramec 3	Calcareous Mudstone	20000	20000	3.6	29.37
	Limestone	20000	20000	3.6	1.22
	Cherty Limestone	20000	20000	3.6	0.29
	Chert	20000	20000	3.6	0
	Calcareous Siltstone	20000	20000	3.6	63.42
	Calcareous Sandstone	20000	20000	3.6	9.7
	Shale	20000	20000	3.6	0
Meramec 2	Calcareous Mudstone	20000	20000	3.1	14.09
	Limestone	20000	20000	3.1	11.55
	Cherty Limestone	20000	20000	3.1	5.30
	Chert	20000	20000	3.1	0
	Calcareous Siltstone	20000	20000	3.1	45.65
	Calcareous Sandstone	20000	20000	3.1	25.39
	Shale	20000	20000	3.1	0

Appendix D-27: Horizontal and vertical variogram ranges by zone for the dip-oriented (C-C') lithology model. The horizontal ranges were adjusted from Lindzey (2015), which were seismically constrained. Vertical ranges were estimated for each zone through vertical variography.

Meramec 1	Calcareous Mudstone	20000	20000	3.2	14.81
	Limestone	20000	20000	3.2	18.11
	Cherty Limestone	20000	20000	3.2	1.99
	Chert	20000	20000	3.2	0
	Calcareous Siltstone	20000	20000	3.2	45.75
	Calcareous Sandstone	20000	20000	3.2	19.35
	Shale	20000	20000	3.2	0
Osage 8	Calcareous Mudstone	20000	20000	2	2.38
	Limestone	20000	20000	2	20.3
	Cherty Limestone	20000	20000	2	0.38
	Chert	20000	20000	2	0
	Calcareous Siltstone	20000	20000	2	24.72
	Calcareous Sandstone	20000	20000	2	52.2
	Shale	20000	20000	2	0
Osage 7	Calcareous Mudstone	20000	20000	2	4.75
	Limestone	20000	20000	2	21.48
	Cherty Limestone	20000	20000	2	0.59
	Chert	20000	20000	2	0
	Calcareous Siltstone	20000	20000	2	27.61
	Calcareous Sandstone	20000	20000	2	45.57
	Shale	20000	20000	2	0
Osage 6	Calcareous Mudstone	20000	20000	3.3	3.64
	Limestone	20000	20000	3.3	54.22
	Cherty Limestone	20000	20000	3.3	4.11
	Chert	20000	20000	3.3	0.14
	Calcareous Siltstone	20000	20000	3.3	19.94
	Calcareous Sandstone	20000	20000	3.3	18.05
	Shale	20000	20000	3.3	0
Osage 5	Calcareous Mudstone	20000	20000	5.9	1.04
	Limestone	20000	20000	5.9	77.59
	Cherty Limestone	20000	20000	5.9	16.57
	Chert	20000	20000	5.9	0.29
	Calcareous Siltstone	20000	20000	5.9	2.25
	Calcareous Sandstone	20000	20000	5.9	4.48
	Shale	20000	20000	5.9	0
Osage 4	Calcareous Mudstone	20000	20000	3.9	0.59
	Limestone	20000	20000	3.9	62.08
	Cherty Limestone	20000	20000	3.9	30.5
	Chert	20000	20000	3.9	5.94
	Calcareous Siltstone	20000	20000	3.9	0.62
	Calcareous Sandstone	20000	20000	3.9	0.2
	Shale	20000	20000	3.9	0

Appendix D-27 cont'd.: Horizontal and vertical variogram ranges by zone for the dip-oriented (C-C') lithology model. The horizontal ranges were adjusted from Lindzey (2015), which were seismically constrained. Vertical ranges were estimated for each zone through vertical variography.

Osage 3	Calcareous Mudstone	20000	20000	3.9	3.44
	Limestone	20000	20000	3.9	51.87
	Cherty Limestone	20000	20000	3.9	40.6
	Chert	20000	20000	3.9	3.71
	Calcareous Siltstone	20000	20000	3.9	0.24
	Calcareous Sandstone	20000	20000	3.9	0.03
	Shale	20000	20000	3.9	0.12
Osage 2	Calcareous Mudstone	20000	20000	1.6	82.08
	Limestone	20000	20000	1.6	5.07
	Cherty Limestone	20000	20000	1.6	7.85
	Chert	20000	20000	1.6	0
	Calcareous Siltstone	20000	20000	1.6	0.6
	Calcareous Sandstone	20000	20000	1.6	0
	Shale	20000	20000	1.6	4.75
Osage 1	Calcareous Mudstone	20000	20000	1	28.25
	Limestone	20000	20000	1	47.59
	Cherty Limestone	20000	20000	1	16.12
	Chert	20000	20000	1	0
	Calcareous Siltstone	20000	20000	1	0.80
	Calcareous Sandstone	20000	20000	1	0
	Shale	20000	20000	1	7.23
Kinderhook	Calcareous Mudstone	20000	20000	1.4	2.72
	Limestone	20000	20000	1.4	1.07
	Cherty Limestone	20000	20000	1.4	3.14
	Chert	20000	20000	1.4	0
	Calcareous Siltstone	20000	20000	1.4	5.87
	Calcareous Sandstone	20000	20000	1.4	0
	Shale	20000	20000	1.4	86.17

Appendix D-27 cont'd.: Horizontal and vertical variogram ranges by zone for the dip-oriented (C-C') lithology model. The horizontal ranges were adjusted from Lindzey (2015), which were seismically constrained. Vertical ranges were estimated for each zone through vertical variography.

Oblique-oriented Lithology Model					
Formation/Zone	Lithology	Major Hozizontal Range (ft)	Minor Hozizontal Range (ft)	Vertical Range (ft)	Lithology (%)
Meramec 7	Calcareous Mudstone	15000	15000	1	17.71
	Limestone	15000	15000	1	0
	Cherty Limestone	15000	15000	1	0
	Chert	15000	15000	1	0
	Calcareous Siltstone	15000	15000	1	74.04
	Calcareous Sandstone	15000	15000	1	8.25
	Shale	15000	15000	1	0
Meramec 6	Calcareous Mudstone	15000	15000	0.9	22.88
	Limestone	15000	15000	0.9	0
	Cherty Limestone	15000	15000	0.9	0
	Chert	15000	15000	0.9	0
	Calcareous Siltstone	15000	15000	0.9	73.55
	Calcareous Sandstone	15000	15000	0.9	3.57
	Shale	15000	15000	0.9	0
Meramec 5	Calcareous Mudstone	15000	15000	2.7	16.86
	Limestone	15000	15000	2.7	0
	Cherty Limestone	15000	15000	2.7	0
	Chert	15000	15000	2.7	0
	Calcareous Siltstone	15000	15000	2.7	58.21
	Calcareous Sandstone	15000	15000	2.7	24.93
	Shale	15000	15000	2.7	0
Meramec 4	Calcareous Mudstone	15000	15000	2.3	21.35
	Limestone	15000	15000	2.3	0
	Cherty Limestone	15000	15000	2.3	0.05
	Chert	15000	15000	2.3	0.18
	Calcareous Siltstone	15000	15000	2.3	72.13
	Calcareous Sandstone	15000	15000	2.3	6.29
	Shale	15000	15000	2.3	0
Meramec 3	Calcareous Mudstone	15000	15000	3.3	21.27
	Limestone	15000	15000	3.3	0.37
	Cherty Limestone	15000	15000	3.3	0.41
	Chert	15000	15000	3.3	0.2
	Calcareous Siltstone	15000	15000	3.3	64.57
	Calcareous Sandstone	15000	15000	3.3	13.18
	Shale	15000	15000	3.3	0
Meramec 2	Calcareous Mudstone	15000	15000	2.5	13.56
	Limestone	15000	15000	2.5	4.89
	Cherty Limestone	15000	15000	2.5	0.79
	Chert	15000	15000	2.5	0
	Calcareous Siltstone	15000	15000	2.5	48.07
	Calcareous Sandstone	15000	15000	2.5	32.69
	Shale	15000	15000	2.5	0

Appendix D-28: Horizontal and vertical variogram ranges by zone for the oblique-oriented (D-D') lithology model. The horizontal ranges were adjusted from Lindzey (2015), which were seismically constrained. Vertical ranges were estimated for each zone through vertical variography.

Meramec 1	Calcareous Mudstone	15000	15000	2.5	11.71
	Limestone	15000	15000	2.5	12.24
	Cherty Limestone	15000	15000	2.5	1.38
	Chert	15000	15000	2.5	0
	Calcareous Siltstone	15000	15000	2.5	49.37
	Calcareous Sandstone	15000	15000	2.5	25.29
	Shale	15000	15000	2.5	0
Osage 2	Calcareous Mudstone	15000	15000	3	4.54
	Limestone	15000	15000	3	17.83
	Cherty Limestone	15000	15000	3	3.00
	Chert	15000	15000	3	0
	Calcareous Siltstone	15000	15000	3	23.35
	Calcareous Sandstone	15000	15000	3	51.29
	Shale	15000	15000	3	0
Osage 1	Calcareous Mudstone	15000	15000	4.3	5.04
	Limestone	15000	15000	4.3	33.35
	Cherty Limestone	15000	15000	4.3	30.56
	Chert	15000	15000	4.3	0
	Calcareous Siltstone	15000	15000	4.3	11.07
	Calcareous Sandstone	15000	15000	4.3	19.98
	Shale	15000	15000	4.3	0
Miss Lime 6	Calcareous Mudstone	15000	15000	6.2	2.92
	Limestone	15000	15000	6.2	34.14
	Cherty Limestone	15000	15000	6.2	43.64
	Chert	15000	15000	6.2	1.89
	Calcareous Siltstone	15000	15000	6.2	7.8
	Calcareous Sandstone	15000	15000	6.2	9.61
	Shale	15000	15000	6.2	0
Miss Lime 5	Calcareous Mudstone	15000	15000	6.2	5.16
	Limestone	15000	15000	6.2	40.51
	Cherty Limestone	15000	15000	6.2	46.06
	Chert	15000	15000	6.2	1.04
	Calcareous Siltstone	15000	15000	6.2	3.21
	Calcareous Sandstone	15000	15000	6.2	4.02
	Shale	15000	15000	6.2	0
Miss Lime 4	Calcareous Mudstone	15000	15000	4.3	1.39
	Limestone	15000	15000	4.3	67.65
	Cherty Limestone	15000	15000	4.3	25.00
	Chert	15000	15000	4.3	5.76
	Calcareous Siltstone	15000	15000	4.3	0.16
	Calcareous Sandstone	15000	15000	4.3	0.03
	Shale	15000	15000	4.3	0

Appendix D-28 cont'd.: Horizontal and vertical variogram ranges by zone for the oblique-oriented (D-D') lithology model. The horizontal ranges were adjusted from Lindzey (2015), which were seismically constrained. Vertical ranges were estimated for each zone through vertical variography.

Miss Lime 3	Calcareous Mudstone	15000	15000	2.4	3.77
	Limestone	15000	15000	2.4	30.29
	Cherty Limestone	15000	15000	2.4	54.45
	Chert	15000	15000	2.4	11.22
	Calcareous Siltstone	15000	15000	2.4	0.12
	Calcareous Sandstone	15000	15000	2.4	0.12
	Shale	15000	15000	2.4	0.04
Miss Lime 2	Calcareous Mudstone	15000	15000	0.6	51.33
	Limestone	15000	15000	0.6	14.13
	Cherty Limestone	15000	15000	0.6	32.47
	Chert	15000	15000	0.6	0.91
	Calcareous Siltstone	15000	15000	0.6	0.42
	Calcareous Sandstone	15000	15000	0.6	0.47
	Shale	15000	15000	0.6	0.27
Miss Lime 1	Calcareous Mudstone	15000	15000	0.6	10.32
	Limestone	15000	15000	0.6	49.51
	Cherty Limestone	15000	15000	0.6	37.19
	Chert	15000	15000	0.6	1.70
	Calcareous Siltstone	15000	15000	0.6	0.25
	Calcareous Sandstone	15000	15000	0.6	0.04
	Shale	15000	15000	0.6	0.98
Kinderhook	Calcareous Mudstone	15000	15000	1.1	10.07
	Limestone	15000	15000	1.1	0.88
	Cherty Limestone	15000	15000	1.1	1.87
	Chert	15000	15000	1.1	0.53
	Calcareous Siltstone	15000	15000	1.1	1.03
	Calcareous Sandstone	15000	15000	1.1	0
	Shale	15000	15000	1.1	85.42

Appendix D-28 cont'd.: Horizontal and vertical variogram ranges by zone for the oblique-oriented (D-D') lithology model. The horizontal ranges were adjusted from Lindzey (2015), which were seismically constrained. Vertical ranges were estimated for each zone through vertical variography.

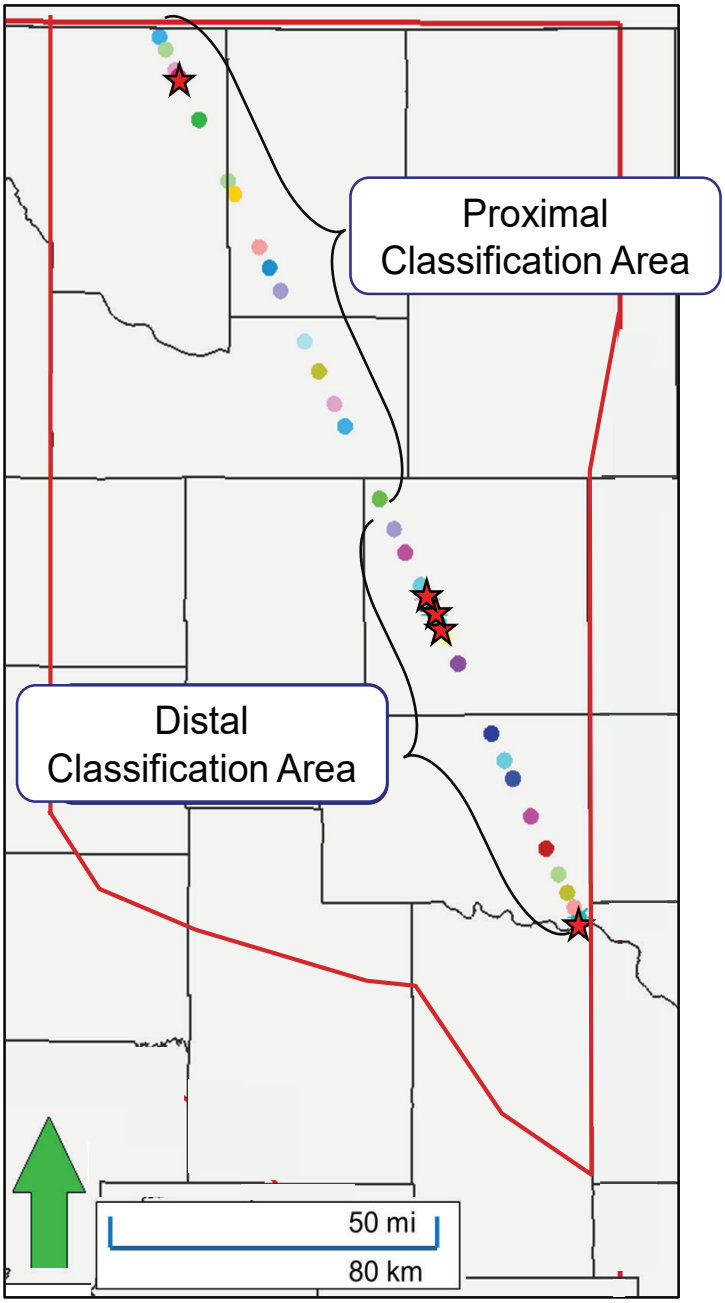

Appendix D-29: Dip-oriented transect with two classification areas. Electrofacies classifications was run in the proximal northern area using data from Chesapeake 1-4 Bann cored well (red star) in a training set to predict the lithologies in the rest of the non-cored wells. In the distal region, data from the Gulf Oil 1-23 Shaffer, Gulf Oil 1-25 Rohling, Gulf Oil 1-14 Musselman, and Petrolia 1 Payne cored wells (red stars) were used in the training set to predict the distal lithologies in the non-cored wells. This resulted in two separate predictive lithology curves which were merged between both areas in order to model the entire transect.

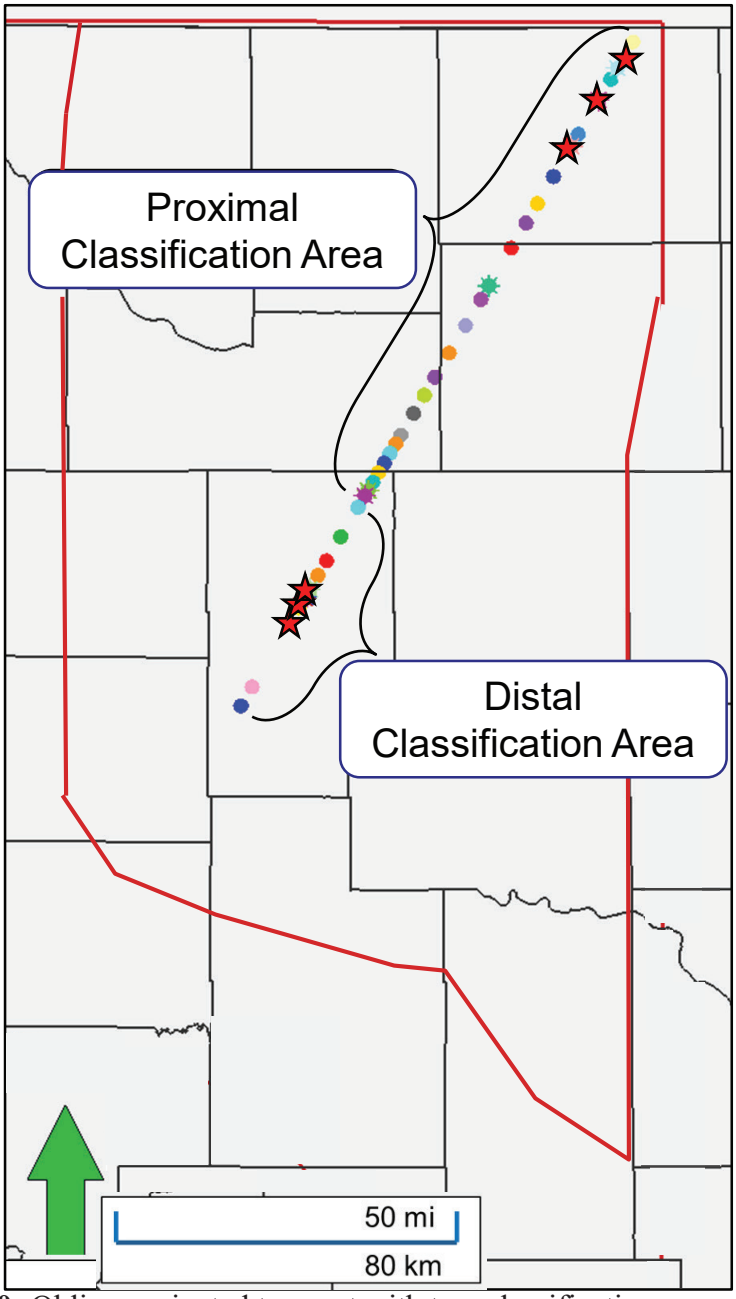

Appendix D-30: Oblique-oriented transect with two classification areas. Electrofacies classifications was run in the proximal northern area using data from Devon 1-8 Kirby, Devon 1-7 Frieouf, and Devon 1-7 Downing cored wells (red stars) in a training set to predict the lithologies in the rest of the non-cored wells. In the distal region, data from the Gulf Oil 1-23 Shaffer, Gulf Oil 1-25 Rohling, and Gulf Oil 1-14 Musselman cored wells (red stars) were used in the training set to predict the distal lithologies in the non-cored wells. This resulted in two separate predictive lithology curves which were merged between both areas in order to model the entire transect.

Appendix E: Stratigraphic Framework and Petrophysical Properties Distributions

Appendix E-1: Derivative Trend Analysis

Derivative trend analysis (DTA) is a type of log attribute analysis used to aid in the interpretation of geological data. The first step in the DTA process is to determine the appropriate smoothing filter/frequency window for the data to reduce the random noise and detail (Guo, 2011). This was achieved using the Gaussian smoothing function in *Techlog*, in which the data points from the GR logs within the smoothing windows are assigned weights based on the distance from the original point of interest (Shapiro and Stockman, 2000). The data points are then recalculated to the weighted average of the neighboring data points. The smoothing function filters out the high frequency noise while keeping the geologically significant trends. The second step is to differentiate the smoothed curves suing the central-difference method:

$$Derivative(i) = \frac{(Value\ (i+l) - Value\ (i-l))}{(Depth\ (i+l) - Depth\ (1-l))}$$

Central difference method determines how the smoothed curve changes by calculating the slope between the nearby points on a curve to measure the derivative of the point of interest. The differentiated curve then displays positive values when the curve original input curve is decreasing upward and negative when it is increasing upward (Wethington and Pranter, 2018).

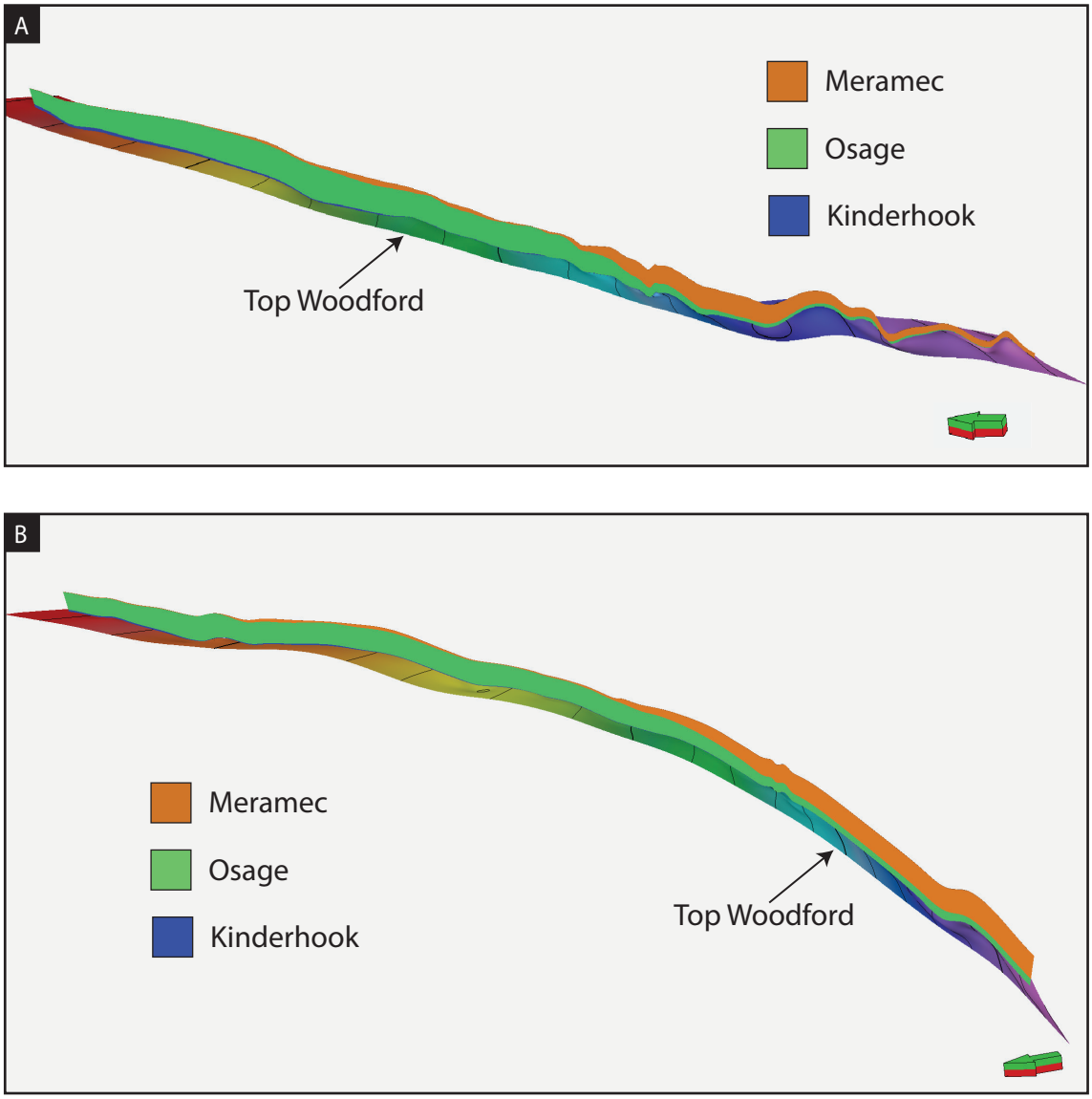

Appendix E-2: Interpreted stratigraphic framework showing relative distributions of the Kinderhookian, Osagean, and Meramecian aged strata. The Kinderhook and Osage thin southward, whereas the Meramec thickens to the south. (A) Dip-oriented (A-A') transect distributions. (B) oblique-oriented (B-B') transect distributions.

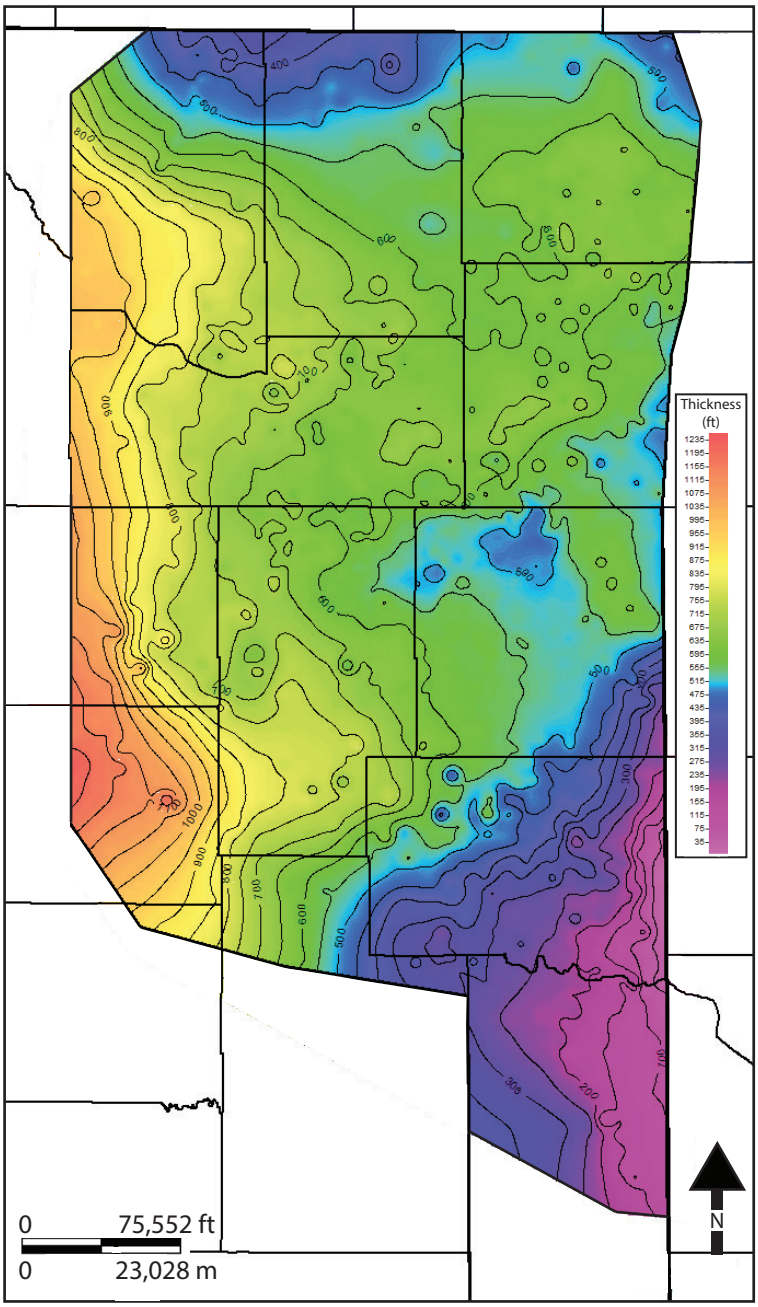

Appendix E-3: Isopach map of the Mississippian interval (Kinderhook, Osage and Meramec) showing general thickening towards the southwest and west and thinning again to the southeast due to proximity to the Nemaha Uplift and the Ardmore Basin.

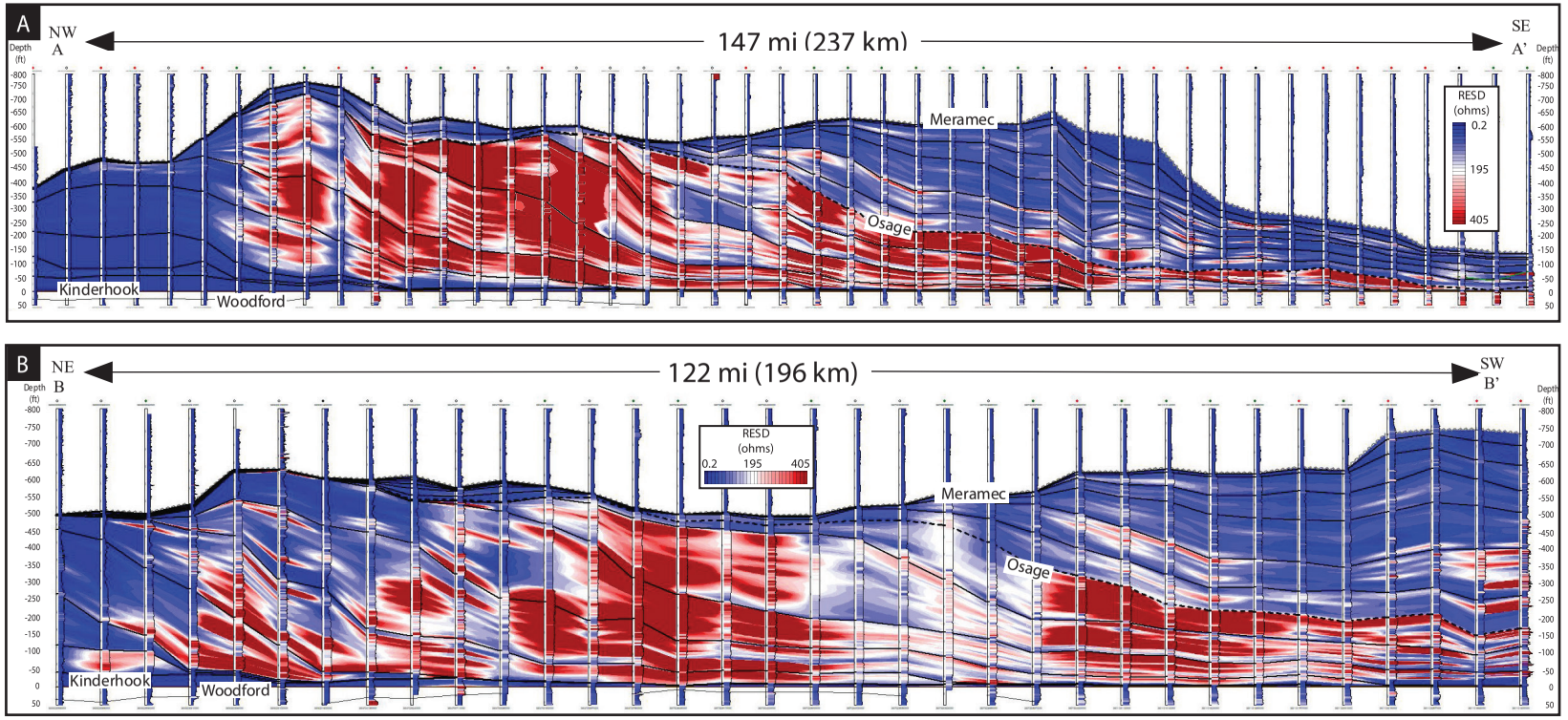

Appendix E-4: Deep Resistivity interpolated models from the RESD using *Petra's* interpretative cross-section function. Resistivity was used to aid the correlation of the top Osage and the internal Osage zones. (A) RESD model of the dip-oriented (A-A') transect . (B) RESD model of the strike-oriented (B-B') transect. Note that the color bar is not logarithmic therefore the RESD values are not accurately portrayed but still convey the higher RESD zones.

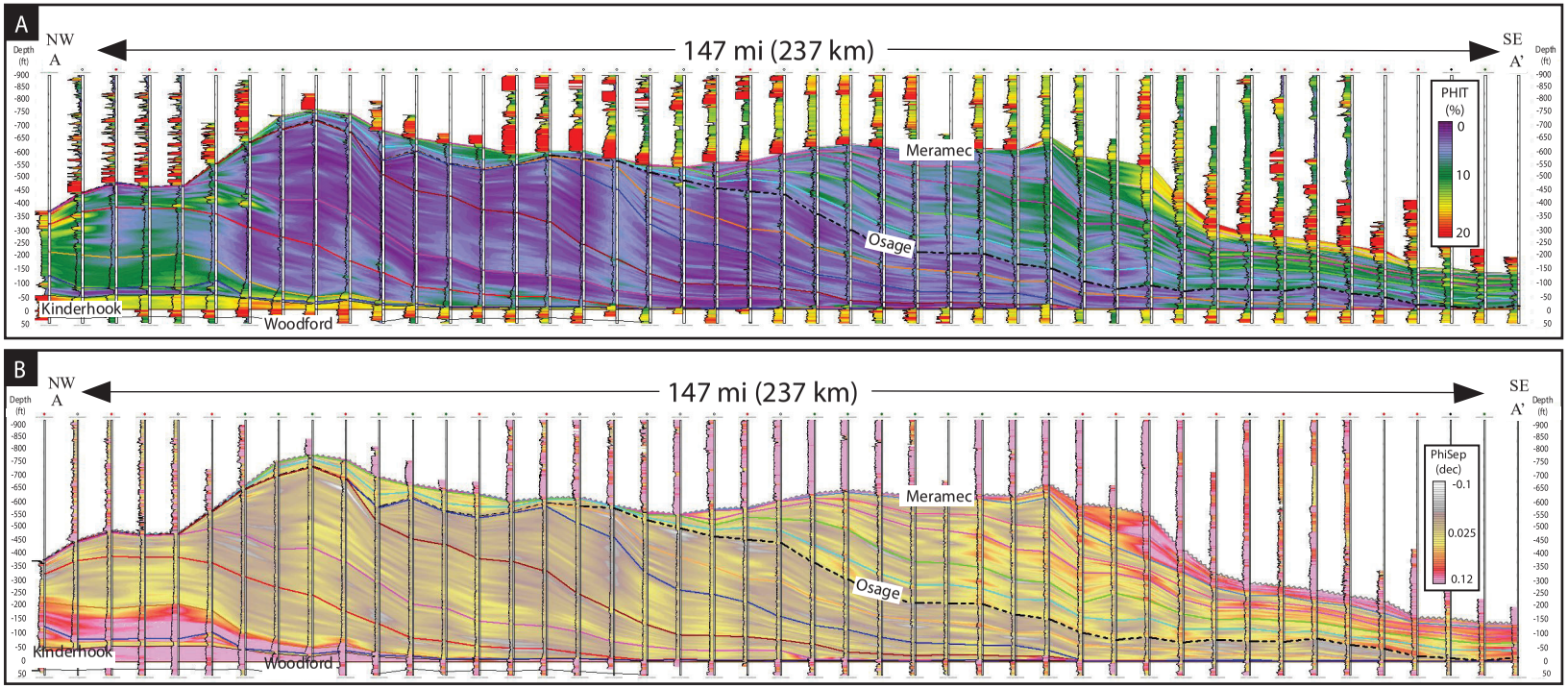

Appendix D-5: (A) Dip-oriented total porosity (PHIT) interpretive stratigraphic cross-section for A-A' not contsrained to lithology. Datum on top Woodford. PHIT model shows lower PHIT values are associated with the interpreted limestones. Higher PHIT values up-dip are associated with altered cherts and cherty limestone due to porosity creation by diagenetic processes and sea level fluctuations resulting in subaerial exposure. Down-dip the higher PHIT values are related to the amount of clay in the system. The clay fills the pore space making calcite-cementation difficult. Intervals with large amounts of calcite-cement have the lowest porosities because the calcite occludes the pore space. (B) Dip-oriented porosity separation (PHISEP) interpretive stratigraphic cross-section for A-A'. Datum on top Woodford. Porosity separation model is a tool used to emphasize dolomitized and clay-rich intervals. High PHISEP values are associated with the higher PHIT intervals, seen above. High PHISEP values are concentrated in the basal Kinderhookian zone and down-dip they associated with the increased clay content within the system. The brighter yellows could indicate dolomitized sections.

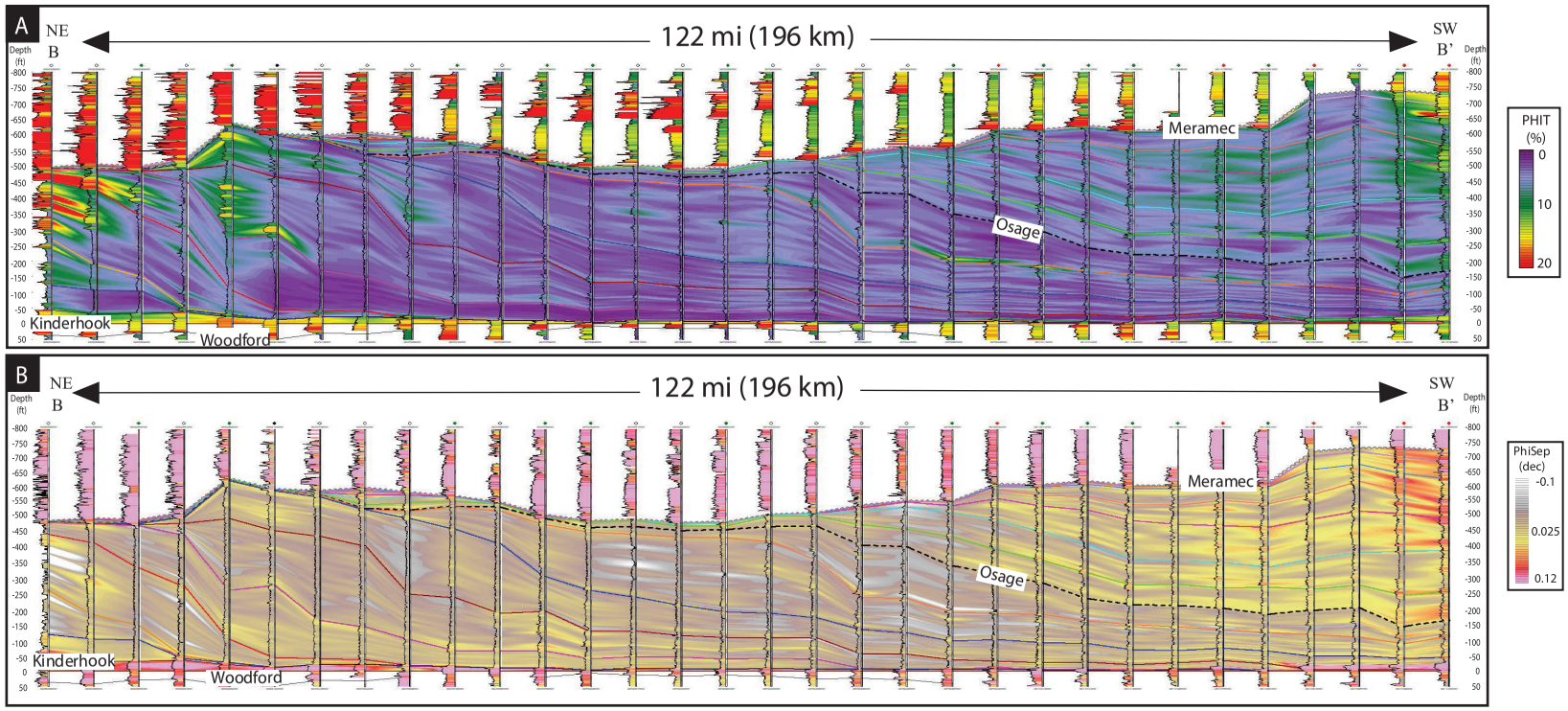

Appendix D-6: (A) Oblique-oriented total porosity (PHIT) interpretive stratigraphic cross-section for A-A' not contsrained to lithology. Datum on top Woodford. PHIT model shows lower PHIT values are associated with the interpreted limestones. Higher PHIT values up-dip are associated with altered cherts and cherty limestone due to porosity creation by diagenetic processes and sea level fluctuations resulting in subaerial exposure. Down-dip the higher PHIT values are related to the amount of clay in the system. The clay fills the pore space making calcite-cementation difficult. Intervals with large amounts of calcite-cement have the lowest porosities because the calcite occludes the pore space. (B) Oblique-oriented porosity separation (PHISEP) interpretive stratigraphic cross-section for A-A'. Datum on top Woodford. Porosity separation model is a tool used to emphasize dolomitized and clay-rich intervals. High PHISEP values are associated with the higher PHIT intervals, seen above. High PHISEP values are concentrated in the basal Kinderhookian zone and down-dip they associated with the increased clay content within the system. The brighter yellows could indicate dolomitized sections.

Dip-oriented Porosity Model				
Formation/Zone	Lithology	Major Hozizontal Range (ft)	Minor Hozizontal Range (ft)	Vertical Range (ft)
Meramec 7	Calcareous Mudstone	10000	10000	1.3
	Limestone	10000	10000	1.3
	Cherty Limestone	10000	10000	1.3
	Chert	10000	10000	1.3
	Calcareous Siltstone	10000	10000	1.3
	Calcareous Sandstone	10000	10000	1.3
	Shale	10000	10000	1.3
Meramec 6	Calcareous Mudstone	10000	10000	1.2
	Limestone	10000	10000	1.2
	Cherty Limestone	10000	10000	1.2
	Chert	10000	10000	1.2
	Calcareous Siltstone	10000	10000	1.2
	Calcareous Sandstone	10000	10000	1.2
	Shale	10000	10000	1.2
Meramec 5	Calcareous Mudstone	10000	10000	1.5
	Limestone	10000	10000	1.5
	Cherty Limestone	10000	10000	1.5
	Chert	10000	10000	1.5
	Calcareous Siltstone	10000	10000	1.5
	Calcareous Sandstone	10000	10000	1.5
	Shale	10000	10000	1.5
Meramec 4	Calcareous Mudstone	10000	10000	1.2
	Limestone	10000	10000	1.2
	Cherty Limestone	10000	10000	1.2
	Chert	10000	10000	1.2
	Calcareous Siltstone	10000	10000	1.2
	Calcareous Sandstone	10000	10000	1.2
	Shale	10000	10000	1.2
Meramec 3	Calcareous Mudstone	10000	10000	1.3
	Limestone	10000	10000	1.3
	Cherty Limestone	10000	10000	1.3
	Chert	10000	10000	1.3
	Calcareous Siltstone	10000	10000	1.3
	Calcareous Sandstone	10000	10000	1.3
	Shale	10000	10000	1.3
Meramec 2	Calcareous Mudstone	10000	10000	1
	Limestone	10000	10000	1
	Cherty Limestone	10000	10000	1
	Chert	10000	10000	1
	Calcareous Siltstone	10000	10000	1
	Calcareous Sandstone	10000	10000	1
	Shale	10000	10000	1

Appendix E-7: Horizontal and vertical variogram ranges by zone for the dip-oriented (C-C') total porosity and porosity separation model. The ranges were decreased from the lithology modeling variograms to account for internal variability within lithologies.

Meramec 1	Calcareous Mudstone	10000	10000	1
	Limestone	10000	10000	1
	Cherty Limestone	10000	10000	1
	Chert	10000	10000	1
	Calcareous Siltstone	10000	10000	1
	Calcareous Sandstone	10000	10000	1
	Shale	10000	10000	1
Osage 1	Calcareous Mudstone	10000	10000	1.1
	Limestone	10000	10000	1.1
	Cherty Limestone	10000	10000	1.1
	Chert	10000	10000	1.1
	Calcareous Siltstone	10000	10000	1.1
	Calcareous Sandstone	10000	10000	1.1
	Shale	10000	10000	1.1
Osage 2	Calcareous Mudstone	10000	10000	1.1
	Limestone	10000	10000	1.1
	Cherty Limestone	10000	10000	1.1
	Chert	10000	10000	1.1
	Calcareous Siltstone	10000	10000	1.1
	Calcareous Sandstone	10000	10000	1.1
	Shale	10000	10000	1.1
Miss Lime 6	Calcareous Mudstone	10000	10000	1.2
	Limestone	10000	10000	1.2
	Cherty Limestone	10000	10000	1.2
	Chert	10000	10000	1.2
	Calcareous Siltstone	10000	10000	1.2
	Calcareous Sandstone	10000	10000	1.2
	Shale	10000	10000	1.2
Miss Lime 5	Calcareous Mudstone	10000	10000	2.8
	Limestone	10000	10000	2.8
	Cherty Limestone	10000	10000	2.8
	Chert	10000	10000	2.8
	Calcareous Siltstone	10000	10000	2.8
	Calcareous Sandstone	10000	10000	2.8
	Shale	10000	10000	2.8
Miss Lime 4	Calcareous Mudstone	10000	10000	2.2
	Limestone	10000	10000	2.2
	Cherty Limestone	10000	10000	2.2
	Chert	10000	10000	2.2
	Calcareous Siltstone	10000	10000	2.2
	Calcareous Sandstone	10000	10000	2.2
	Shale	10000	10000	2.2

Appendix E-7 cont'd: Horizontal and vertical variogram ranges by zone for the dip-oriented (C-C') total porosity and porosity separation model. The ranges were decreased from the lithology modeling variograms to account for internal variability within lithologies.

Miss Lime 3	Calcareous Mudstone	10000	10000	2.2
	Limestone	10000	10000	2.2
	Cherty Limestone	10000	10000	2.2
	Chert	10000	10000	2.2
	Calcareous Siltstone	10000	10000	2.2
	Calcareous Sandstone	10000	10000	2.2
	Shale	10000	10000	2.2
Miss Lime 2	Calcareous Mudstone	10000	10000	1.1
	Limestone	10000	10000	1.1
	Cherty Limestone	10000	10000	1.1
	Chert	10000	10000	1.1
	Calcareous Siltstone	10000	10000	1.1
	Calcareous Sandstone	10000	10000	1.1
	Shale	10000	10000	1.1
Miss Lime 1	Calcareous Mudstone	10000	10000	0.7
	Limestone	10000	10000	0.7
	Cherty Limestone	10000	10000	0.7
	Chert	10000	10000	0.7
	Calcareous Siltstone	10000	10000	0.7
	Calcareous Sandstone	10000	10000	0.7
	Shale	10000	10000	0.7
Kinderhook	Calcareous Mudstone	10000	10000	0.75
	Limestone	10000	10000	0.75
	Cherty Limestone	10000	10000	0.75
	Chert	10000	10000	0.75
	Calcareous Siltstone	10000	10000	0.75
	Calcareous Sandstone	10000	10000	0.75
	Shale	10000	10000	0.75

Appendix E-7 cont'd: Horizontal and vertical variogram ranges by zone for the dip-oriented (C-C') total porosity and porosity separation model. The ranges were decreased from the lithology modeling variograms to account for internal variability within lithologies.

Oblique-oriented Porosity Model				
Formation/Zone	Lithology	Major Hozizontal Range (ft)	Minor Hozizontal Range (ft)	Vertical Range (ft)
Meramec 7	Calcareous Mudstone	8000	8000	1
	Limestone	8000	8000	1
	Cherty Limestone	8000	8000	1
	Chert	8000	8000	1
	Calcareous Siltstone	8000	8000	1
	Calcareous Sandstone	8000	8000	1
	Shale	8000	8000	1
Meramec 6	Calcareous Mudstone	8000	8000	0.9
	Limestone	8000	8000	0.9
	Cherty Limestone	8000	8000	0.9
	Chert	8000	8000	0.9
	Calcareous Siltstone	8000	8000	0.9
	Calcareous Sandstone	8000	8000	0.9
	Shale	8000	8000	0.9
Meramec 5	Calcareous Mudstone	8000	8000	2.7
	Limestone	8000	8000	2.7
	Cherty Limestone	8000	8000	2.7
	Chert	8000	8000	2.7
	Calcareous Siltstone	8000	8000	2.7
	Calcareous Sandstone	8000	8000	2.7
	Shale	8000	8000	2.7
Meramec 4	Calcareous Mudstone	8000	8000	2.3
	Limestone	8000	8000	2.3
	Cherty Limestone	8000	8000	2.3
	Chert	8000	8000	2.3
	Calcareous Siltstone	8000	8000	2.3
	Calcareous Sandstone	8000	8000	2.3
	Shale	8000	8000	2.3
Meramec 3	Calcareous Mudstone	8000	8000	3.3
	Limestone	8000	8000	3.3
	Cherty Limestone	8000	8000	3.3
	Chert	8000	8000	3.3
	Calcareous Siltstone	8000	8000	3.3
	Calcareous Sandstone	8000	8000	3.3
	Shale	8000	8000	3.3
Meramec 2	Calcareous Mudstone	8000	8000	2.5
	Limestone	8000	8000	2.5
	Cherty Limestone	8000	8000	2.5
	Chert	8000	8000	2.5
	Calcareous Siltstone	8000	8000	2.5
	Calcareous Sandstone	8000	8000	2.5
	Shale	8000	8000	2.5

Appendix E-8: Horizontal and vertical variogram ranges by zone for the oblique-oriented (D-D') total porosity and porosity separation model. The ranges were decreased from the lithology modeling variograms to account for internal variability within lithologies.

Meramec 1	Calcareous Mudstone	8000	8000	2.5
	Limestone	8000	8000	2.5
	Cherty Limestone	8000	8000	2.5
	Chert	8000	8000	2.5
	Calcareous Siltstone	8000	8000	2.5
	Calcareous Sandstone	8000	8000	2.5
	Shale	8000	8000	2.5
Osage 1	Calcareous Mudstone	8000	8000	3
	Limestone	8000	8000	3
	Cherty Limestone	8000	8000	3
	Chert	8000	8000	3
	Calcareous Siltstone	8000	8000	3
	Calcareous Sandstone	8000	8000	3
	Shale	8000	8000	3
Osage 2	Calcareous Mudstone	8000	8000	4.3
	Limestone	8000	8000	4.3
	Cherty Limestone	8000	8000	4.3
	Chert	8000	8000	4.3
	Calcareous Siltstone	8000	8000	4.3
	Calcareous Sandstone	8000	8000	4.3
	Shale	8000	8000	4.3
Miss Lime 6	Calcareous Mudstone	8000	8000	6.2
	Limestone	8000	8000	6.2
	Cherty Limestone	8000	8000	6.2
	Chert	8000	8000	6.2
	Calcareous Siltstone	8000	8000	6.2
	Calcareous Sandstone	8000	8000	6.2
	Shale	8000	8000	6.2
Miss Lime 5	Calcareous Mudstone	8000	8000	6.2
	Limestone	8000	8000	6.2
	Cherty Limestone	8000	8000	6.2
	Chert	8000	8000	6.2
	Calcareous Siltstone	8000	8000	6.2
	Calcareous Sandstone	8000	8000	6.2
	Shale	8000	8000	6.2
Miss Lime 4	Calcareous Mudstone	8000	8000	4.3
	Limestone	8000	8000	4.3
	Cherty Limestone	8000	8000	4.3
	Chert	8000	8000	4.3
	Calcareous Siltstone	8000	8000	4.3
	Calcareous Sandstone	8000	8000	4.3
	Shale	8000	8000	4.3

Appendix E-8 cont'd: Horizontal and vertical variogram ranges by zone for the oblique-oriented (D-D') total porosity and porosity separation model. The ranges were decreased from the lithology modeling variograms to account for internal variability within lithologies.

Miss Lime 3	Calcareous Mudstone	8000	8000	2.4
	Limestone	8000	8000	2.4
	Cherty Limestone	8000	8000	2.4
	Chert	8000	8000	2.4
	Calcareous Siltstone	8000	8000	2.4
	Calcareous Sandstone	8000	8000	2.4
	Shale	8000	8000	2.4
Miss Lime 2	Calcareous Mudstone	8000	8000	0.6
	Limestone	8000	8000	0.6
	Cherty Limestone	8000	8000	0.6
	Chert	8000	8000	0.6
	Calcareous Siltstone	8000	8000	0.6
	Calcareous Sandstone	8000	8000	0.6
	Shale	8000	8000	0.6
Miss Lime 1	Calcareous Mudstone	8000	8000	0.6
	Limestone	8000	8000	0.6
	Cherty Limestone	8000	8000	0.6
	Chert	8000	8000	0.6
	Calcareous Siltstone	8000	8000	0.6
	Calcareous Sandstone	8000	8000	0.6
	Shale	8000	8000	0.6
Kinderhook	Calcareous Mudstone	8000	8000	1.1
	Limestone	8000	8000	1.1
	Cherty Limestone	8000	8000	1.1
	Chert	8000	8000	1.1
	Calcareous Siltstone	8000	8000	1.1
	Calcareous Sandstone	8000	8000	1.1
	Shale	8000	8000	1.1

Appendix E-8 cont'd: Horizontal and vertical variogram ranges by zone for the oblique-oriented (D-D') total porosity and porosity separation model. The ranges were decreased from the lithology modeling variograms to account for internal variability within lithologies.